Ivan Estupiña Martos

Assessment of Ground-Borne Vibrations from Urban Rail Transit

Master Thesis

July 2022

Assessment of Ground-Borne Vibrations from Urban Rail Transit

Master Thesis

July 2022

Student: **Ivan Estupina Martos**

Supervisor: **Eyal Levenberg**

Cover photo: Ivan Estupina Martos, 2022

Published by: DTU, Department of Civil Engineering, Brovej, Building 118, 2800 Kgs. Lyngby, Denmark

www.byg.dtu.dk

Preface

This study represents the work of a master's thesis conducted at the Technical University of Denmark (DTU) in collaboration with IDOM Consulting, Engineering, Architecture. The study counts for 30 ECTS and has been running for 6 months from February 1st to July 30th. It concludes the author's study in the Master's degree in Civil Engineering at the Department of Civil Engineering at DTU.

It is assumed that the reader has basic knowledge in the areas of mathematics, physics, and railway engineering.

Ivan Estupina Martos - s202268

SIGNED: .....

DATE: 30/07/2022 .....

Abstract

The focus of this Master Project is on ground-borne vibrations caused by rail transit that operates in urban environments, i.e., a class of relatively lightweight and slow-moving trains that frequently run close to buildings and facilities. Specifically, the work commences with a review of existing knowledge about rail-induced ground vibrations: (i) generation and propagation, (ii) possible sources, (iii) mitigation measures, and (iv) common vibration characterization models.

Next, a primarily analytical methodology is developed to characterize and analyze the vibrations from the wheel-rail contact (source) and their propagation to a nearby structure (receiver). The theoretical development considers both quasi-static effects due to the moving vehicle's self-weight and dynamic effects due to impacts caused by defects at the wheel-rail interface.

Finally, the developed methodology is applied to the case study of the not-yet-built section of the Ring 3 light rail line that will run through the DTU campus in Lyngby. One of the objectives during the realization of the case study is to quantify and characterize the vibrations based on the project's specific characteristics. It is also intended to study how different elements in the track-ground-structure system affect vibration transmission, especially the damping mats installed as vibration mitigation elements.

With the intention that the ideas and methods of this project will continue to be expanded and improved, a field instrumentation plan is proposed for future work. The implementation of this plan allows validating with actual results both the methodology used and the projected vibration features.

Dedication and acknowledgements

This work has been accomplished under the supervision of Associate Professor Eyal Levenberg from the Department of Civil Engineering at DTU. Thank you, Eyal, for your guidance, support and interest in the project.

Other people who have participated and collaborated in the development of the work are Asmus Skar, assistant professor at DTU; Sebastian Andersen, postdoc at DTU; María del Mar Mayo, Civil Engineer at IDOM and Pablo Salvador, professor in the Department of Transport Infrastructure and Engineering at the Polytechnic University of Valencia. They have provided their knowledge and experience to contribute to the smooth development of the work. My sincere gratitude to all of you for that.

Juliana, David, Julien, and Pia, my office mates, have given me their company, support, and friendship for almost half a year, making this experience much more special. Thank you for all the good times in the office, and best of luck to all of you in the future.

Last but not least, a special thanks to my parents. To my father, for his way of being, comprehension, and support, and to my mother, for helping, encouraging, and understanding me like no one else. Be sure that all this would not have been possible without being able to count on you.

Table of Contents

Page

List of Tables **xi**

List of Figures **xiii**

1 Introduction **1**
1.1 Background and motivation 1
1.2 Thesis structure 3

2 Literature review **5**
2.1 Urban rail-induced vibration generation and propagation 5
2.1.1 Ground vibration propagation and attenuation 6
2.1.2 Vibration propagation in structures 8
2.2 Possible sources of rail-induced ground-borne vibrations 10
2.2.1 Moving load effect 10
2.2.2 Distributed track unevenness 11
2.2.3 Localized defects at the wheel-rail interface 11
2.3 Common vibration mitigation measures 12
2.3.1 Mitigation at source 13
2.3.2 Mitigation in the transmission path 16
2.4 Common modeling approaches for forecasting vibration features 17
2.4.1 Numerical models 17
2.4.2 Analytical models 18
2.4.3 Empirical models 19
2.4.4 Hybrid models 20

3 Objectives and methodology **21**
3.1 Objectives 21
3.2 Methodology 21
3.2.1 Quasi-static analysis due to the moving load effect 22

3.2.2 Dynamic analysis due to irregularities in the wheel-rail interface 29
3.3 Assumptions and limits 41

4 Vibration analysis case study: Ring 3 Letbanen at DTU 43
4.1 Quasi-static analysis 43
4.1.1 Inputs 43
4.1.2 Calculations 45
4.1.3 Conclusions 51
4.2 Dynamic analysis 53
4.2.1 Inputs 53
4.2.2 Calculations 54
4.2.3 Conclusions 62
4.3 Validation of results 65

5 Conclusion 69
5.1 Summary 69
5.2 Findings and discussion 69
5.3 Recommendations for future work 70

Bibliography 75

List of Tables

Table **Page**

4.1 Vehicle technical data for the quasi-static analysis. 44
4.2 Soil elastic properties for the dynamic analysis. 44
4.3 Track inputs for the quasi-static analysis. 45
4.4 Characteristics of a standard building 51
4.5 Vehicle technical data for the dynamic analysis. 53
4.6 Track inputs for the dynamic analysis. 54
4.7 Soil elastic properties for the dynamic analysis. 54
4.8 Sensitivity analysis of Equation 3.17 65

List of Figures

Figure **Page**

1.1 Two tramways at a stop just few meters away from buildings in Sydney (Australia). 2
1.2 Recreation of the Siemens Avenio light rail unit running at Anker Engelunds Vej. . 2
1.3 Laying of precast concrete slabs that are part of the track of the Ring 3 light rail line on the section next to the Lyngby shopping center. 3

2.1 P-wave, S-wave and Rayleigh wave propagation. 6
2.2 Geometric damping for body and surface waves when a point load is applied on the surface. 7
2.3 Resonance transmissibility as a function of the ratio of natural to input frequencies in a mechanical oscillatory system. 9
2.4 A complex vibration pattern separated into a set of vibration modes. 10
2.5 Flexible modes of the slabs in an embedded rail track model. 10
2.6 Rail corrugation. 11
2.7 Rail squat. 12
2.8 Wheel flat. 13
2.9 The mass breakdown and sprung environments of a rail vehicle bogie with outboard bearing wheelsets. 14
2.10 Continuously supported and fastened embedded ballastless track system developed by *Pandrol* 14
2.11 Continuous under slab mat MATRACK developed by *Isolgomma* 15
2.12 Vibration mitigation measures on the transmission path 16
2.13 Continuously supported two-layer model for an ERS track. 19

3.1 General scheme of the vibration transmission path. 22
3.2 An infinite Euler beam continuously supported on a Winkler elastic foundation subjected to a point force P moving at a velocity V. 22
3.3 An infinite Euler beam continuously supported on a Winkler elastic foundation subjected to several point forces P representing all the axes of the MU and moving at a speed V. 23

3.4 Loading and unloading over time for the whole of a concrete slab due to the passage of the train over it. . . . 24
3.5 Infinitely large half-space where a force P is applied on the surface and the displacements at any point of the terrain N are to be known. . . . 25
3.6 3-storey building modelled with springs and masses subjected to an external force due to vertical displacements on the ground. . . . 26
3.7 Time and frequency domains of an impulse load. . . . 30
3.8 Infinitely long Euler-Bernoulli beam on a Winkler foundation subjected to an impulsive dynamic load, Imp, at $x = 0$. . . . 31
3.9 Geometric models of rail and wheel defects. . . . 33
3.10 A wheel passing through a level defect. . . . 33
3.11 Generation of displacements under the rail due to impulsive loading, and load transmission to the concrete slab. . . . 34
3.12 Representation of the impact due to a rail defect of two contiguous wheels that are offset by Δt. . . . 35
3.13 Representation of the impacts due to a wheel flat in one of the wheels. . . . 35
3.14 Transmission of loads in different track layers due to multiple impulsive loads generated by defects at the wheel-rail interface. . . . 36
3.15 Two equivalent loads transmitted from the bottom face of the concrete slab. . . . 36
3.16 Slab-damping mat-soil load transmission by the mass-spring-damper model. . . . 37
3.17 Model of a track on the surface of a half-space and harmonic surface displacements u and w in response to the force $F(t)$. . . . 40

4.1 Siemens Avenio side view. . . . 44
4.2 edilon)(sedra Embedded Rail System on the groove of the slab track. . . . 45
4.3 Displacement under one rail for the maximum wheel load applied in $x = 0$. . . . 46
4.4 Distributed load under one rail for the maximum wheel load applied in $x = 0$. . . . 46
4.5 Displacement under one rail due to the total train weight when the front axle is in $x = 0$. . . . 46
4.6 Distributed load under one rail due to the total train weight when the front axle is in $x = 0$. . . . 47
4.7 Total load on one slab as a function of time. . . . 47
4.8 Horizontal surface displacement in the x-direction at a point 6 metres away from the track as the train moves away from it. . . . 48
4.9 Horizontal surface displacement in the y-direction at a point 6 metres away from the track as the train moves away from it. . . . 48
4.10 Vertical surface displacement in the z-direction at a point 6 metres away from the track as the train moves away from it. . . . 49

4.11 Total horizontal surface displacement in the x-direction at a point 6 metres away from the track over time. . . . 49
4.12 Total horizontal surface displacement in the y-direction at a point 6 metres away from the track over time. . . . 50
4.13 Total vertical surface displacement in the z-direction at a point 6 metres away from the track over time. . . . 50
4.14 Vertical displacement for each one of the three storeys of the building. . . . 51
4.15 Vertical soil surface displacements at a point 6 metres away from the track over time for 3-meter long slabs. . . . 52
4.16 Vertical displacement for each one of the three storeys of the building for 3-meter slabs track. . . . 52
4.17 Displacement at $x = 0$ for a unit impulsive load. . . . 55
4.18 Displacement at $x = 0$ for an impulsive load caused by the wheel when going through a 60 mm long squat. . . . 55
4.19 Displacements along the rail for a given time due to a unit load. . . . 56
4.20 Displacements at the defect position ($x = 0$) over time for eight impulsive loads due to the considered squat defect. . . . 56
4.21 Displacements over time at $x = 0$ for nine impulsive loads due to a wheel flat. . . . 57
4.22 Load $F_{o,1}(t)$ on a concrete slab over time for one impulsive load due to a squat rail defect located in the slab mid-point. . . . 57
4.23 Load $F_{o,8}(t)$ on a concrete slab over time for eight impulsive loads due to a squat rail defect located in the slab mid-point. . . . 58
4.24 Vertical displacements over time, $x_{m1}(t)$, on a concrete slab subjected to $F_{o,8}(t)$ and supported on an anti-vibration mat. . . . 59
4.25 Load transmitted to the soil, $F(t)$. . . . 59
4.26 Load transmitted to the soil, $F(t)$, for the case without damping mat. . . . 60
4.27 DFT of $F(t)$ with and without damping mat. . . . 60
4.28 Transfer functions H_u and H_w for a radius $r = 6$ m. . . . 61
4.29 DFT of $u(t)$ with and without damping mat. . . . 61
4.30 DFT of $w(t)$ with and without damping mat. . . . 61
4.31 Transfer functions H_u and H_w over radius, r, for the frequency $f = 1.3$ Hz. . . . 62
4.32 Force $F(t)$ transmitted to the ground for different values of the viscous damping coefficient, c, of the damping mat. . . . 63
4.33 DFT of $F(t)$ for different values of the viscous damping coefficient, c, of the damping mat. . . . 63
4.34 Force $F(t)$ transmitted to the ground for different values of the spring stiffness, k, of the damping mat. . . . 64
4.35 DFT of $F(t)$ for different values of the spring stiffness, k, of the damping mat. . . . 64

4.36 Examples of impulse excitation responses. 66
4.37 Relations between vehicle speed and maximum wheel-rail dynamic impact forces induced by wheel flats of different sizes. 67
4.38 Spectrogram of different wheel-rail excitations. 68

5.1 Signal acquisition process. 71
5.2 Sensor set-up for ground measurements. 72
5.3 Field instrumentation plan. 74

Chapter 1

Introduction

1.1 Background and motivation

Over the past few decades, several factors have led to a tremendous growth in the popularity of urban rail transport. These include rising fuel prices, as well as the need to reduce CO_2 emissions from private vehicles to combat climate change and meet the Sustainable Development Goals recently introduced by the United Nations [1]. Moreover, there is a clear trend in major European cities to reduce the area dedicated to large interurban roads and return it to pedestrians in the form of, e.g., green zones. Urban rail transport, and specifically metro and light-rail, are considered an effective mobility solution in big cities to roads; this is due to their high capacity, elevated safety, and lower energy requirements [2]. However, given that metro and light-rail operate within densely populated areas close to residential, commercial, and educational buildings, they cause ground-borne vibrations. Such vibrations interact with the environment and negatively affect the quality of life of residents; they can cause malfunction of sensitive equipment, and may also induce damage to structures [3].

There are a large number of real cases that expose the aforementioned issues with vibrations. In Murcia, Spain, an association created because of the nuisance to neighbors related to the running of the city's tramway, asked for vibration protection measures to be included in the project to extend one of the tramway lines. The main cause of this demand was the discomfort of residents living near the sections of the tramway already built, who had previously complained about vibrations [5]. In Zaragoza, also in Spain, a similar case occurred: several neighborhood associations complained about the decrease in their quality of life due to the vibrations and noise generated by the light rail. In this case, in addition, some neighbors reported the appearance of cracks in their homes as well as other damages [6].

There have been cases where even urban rail lines were not developed because of possible vibration effects. A good example is Duke University in Durham, USA. Officials at this uni-

Figure 1.1: Two tramways at a stop just few meters away from buildings in Sydney (Australia) [4].

versity in the state of North Carolina blocked a planned light-rail line that would cross their property. They raised concerns that the construction and operation of the line could interfere with sensitive equipment at the school's sprawling medical campus, that the train line would border. Officials also worried about the project's impact on the underground utilities that serve the medical center, and the possibility of new lawsuits [7].

The work developed in this Master's Thesis is motivated by the need to quantify and characterize the vibration problem caused by urban rail, and assess the effectiveness of the mitigation technologies. The specific trigger for this work was the upcoming light rail construction project that runs through DTU campus.

Figure 1.2: Recreation of the Siemens Avenio light rail unit running at Anker Engelunds Vej [8].

Figure 1.3: Laying of precast concrete slabs that are part of the track of the Ring 3 light rail line on the section next to the Lyngby shopping center.

1.2 Thesis structure

This work begins with a review of literature (Chapter 2) that covers four main topics: (i) overview of vibration generation and wave propagation; (ii) possible sources of urban rail-induced ground-borne vibrations; (iii) common vibration mitigation measures; and (iv) common modeling approaches for forecasting vibration features. Afterwards the specific study objectives and the general methodology for both quasi-static and dynamic effects are presented (Chapter 3). In Chapter 4, a vibration analysis case study is carried out applying the already developed methodology in Chapter 3. Findings are validated on the basis of other results from similar projects. Lastly, Chapter 5 offers an outline of the developed work and the main findings. The recommendations for future work include a proposed field instrumentation plan to enable validation, with measured data, of the modelling approach choices and the projected vibration features.

Chapter 2

Literature review

This chapter covers the most relevant points within the field of study of rail-induced ground-borne vibrations. For this purpose, a previous work of search, selection and summary of several publications, such as scientific articles and related books, has been carried out. The selection part is especially important, since most of the existing literature is focused on vibrations generated by high-speed trains, while the problem of urban rail-induced vibrations is less studied, although it has been developed to a great extent during the last years.

The literature study is fully focused on urban rail transit and begins by explaining the processes by which vibrations propagate through the ground and in nearby structures, as well as some basics on vibration generation. Once the physical background of the problem is generally understood, the different sources of rail-induced ground-borne vibrations are described and the most common vibration mitigation measures in existing projects and their characteristics are introduced. The last section of this chapter refers to the most common approaches to model the different system interfaces with the objective of forecasting vibration features.

2.1 Urban rail-induced vibration generation and propagation

In the scope of this project, vibration is a mechanical phenomenon that consists of repetitive or periodic movements in time about a point of equilibrium. The term *mechanical oscillation* can be used equivalently, although *vibration* is usually used when the oscillation takes place in a solid [9]. The generation of ground-borne vibrations is a consequence of the release of any kind of energy in the ground; being this release caused by the vehicle dynamic forces passing from the wheel into the track in the case of rail-induced vibrations. These vibrations propagate in the form of superficial and body waves through the various track elements and the ground beneath the track, until they reach the foundations of nearby structures.

2.1.1 Ground vibration propagation and attenuation

Lamb [10] published the first paper studying wave propagation in an elastic half-space, what is either of the two parts into which a plane divides the three-dimensional space. In this work it was concluded that when a dynamic load is applied to the surface of a half-space there are mainly three types of waves propagating in it: two body waves, P-waves and S-waves, and surface waves, called Rayleigh waves. In P-waves, also referred to as compression waves, the particles move in the direction of propagation, while in S-waves, or shear waves, they move in the direction perpendicular to the direction of propagation. R-waves (Rayleigh waves) appear on the free surface and have an associated elliptical motion of the particles on the ground [11].

In Figure 2.1 the R-waves elliptical motion has been decomposed into a horizontal and a vertical component. The propagation velocity of P-waves, C_p, is greater than that of S-waves, C_s, while C_s is greater than the propagation velocity of R-waves, C_r. The speed of P-waves and S-waves can be computed analytically as a function of the density, the bulk modulus and the shear modulus of the medium through which they are propagated. In the case of Rayleigh waves numerous formulas exist in the literature to approximate the wave speed [12].

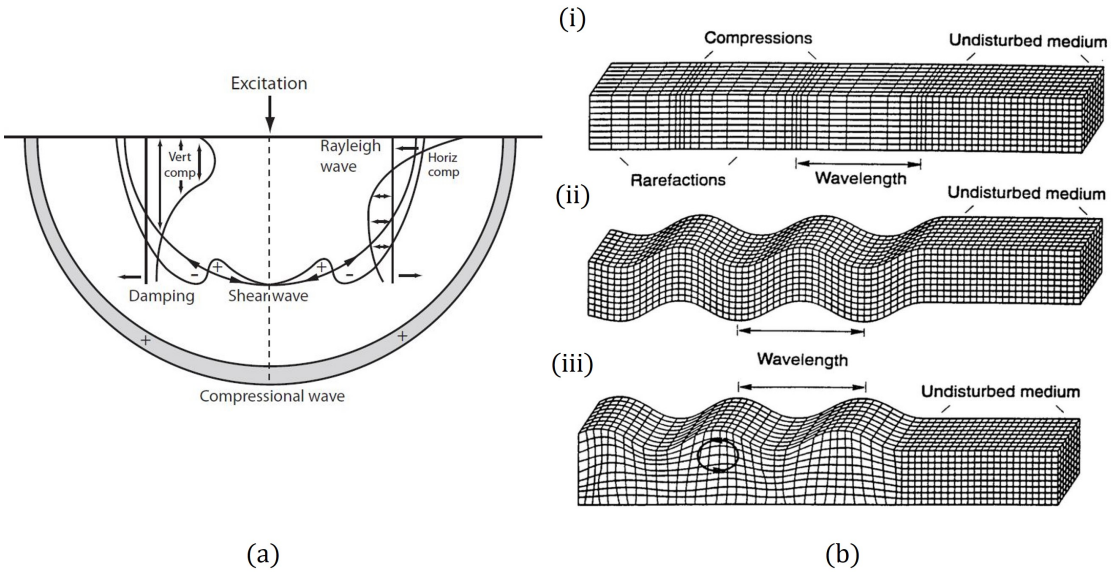

Figure 2.1: (a) Wave propagation, slice view [13]. (b) Displacement characteristics of body waves: (i) P-wave, (ii) S-wave, and (iii) Rayleigh (surface) wave [14].

Commonly, an emphasis is placed on the propagation of Rayleigh waves as they transmit around two thirds of the total excitation energy while S-waves and P-waves transmit approximately 26% and 7%, respectively [13]. Thus, R-waves contribute to a greater extent to causing negative effects both in the railway track and the surrounding structures.

The energy of a vibration system is proportional to the square of the vibration amplitude, that represents the distance from the stationary position to the extreme position on either side of the wave. The amplitude of vibrations reaching nearby structures depends on several factors such as the level of energy released at the source or the building dynamic strength. Another relevant factor, that occurs during the propagation process, is the phenomenon of vibration attenuation, in which the vibration energy is dissipated. Generally, the attenuation of vibrations with distance is composed of two factors: geometric damping and material damping.

The geometric damping occurs due to the decrease of the local energy density caused by the increase in wave front surface area during propagation away from the source, and it depends on the location and type of vibration source. Figure 2.2 shows, as an example, the propagation and geometric damping for body waves and surface waves when applying a point load on the surface.

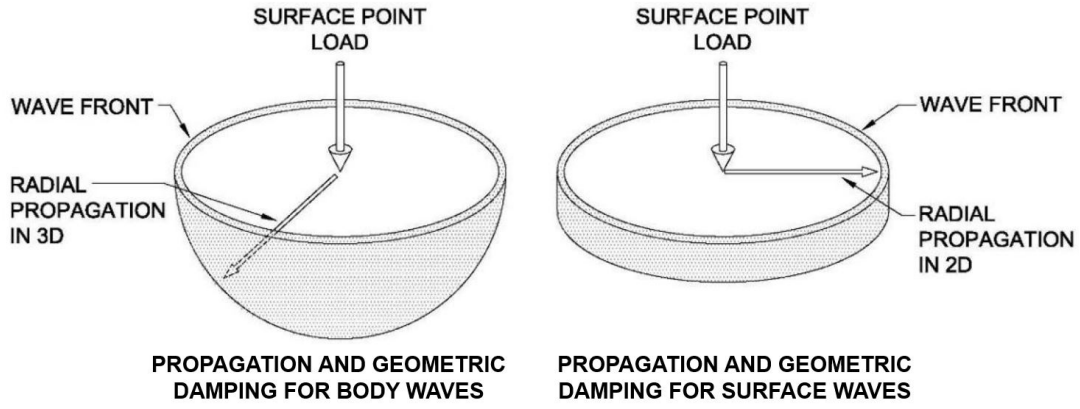

Figure 2.2: Geometric damping for body and surface waves when a point load is applied on the surface [15].

In ground-borne vibration propagation, material damping is an inherently non-linear property of the soil and refers to the conversion of of mechanical energy of a vibrating system, soil in this case, into thermal energy. In this process, the vibration energy is reduced due to the friction and cohesion between soil particles as soil is not perfectly elastic. A relevant basic concept is the loss factor η, which is proportional to the ratio of the energy dissipation per wave cycle divided by the maximum potential energy in the same cycle.

The decay of amplitude of vibration with distance can be described by [16]:

$$w_2 = w_1 \left(\frac{r_1}{r_2}\right)^n e^{-\alpha(r_2 - r_1)} \tag{2.1}$$

Where w_1 and w_2 are vibration amplitudes at distance r_1 and r_2 from a source of vibration, n is a geometric damping coefficient and α is a material damping coefficient. n is analytically determined as a function of the type of source, the type of wave and the source location. The material damping coefficient, α, is expressed as:

$$\alpha = \frac{\pi \eta f}{c} \tag{2.2}$$

Where η is the loss factor, f is the wave frequency and c is the wave velocity.

2.1.2 Vibration propagation in structures

Ground-borne vibrations that reach nearby buildings are propagated from the ground to the building foundation and then from the foundation to the floor system through building members such as beams and columns. The ground-building vibration interaction process is known as immission and varies depending on the building typology. Therefore, different types of buildings tend to have different behaviors to rail-induced vibrations. Some types can even amplify vibrations significantly while centenary-old buildings offer greater attenuation compared to modern buildings [17].

The amplitude of a vibration is commonly characterized by either the displacement, the velocity or the acceleration of the oscillatory movement of an object [18]. When significant vibration intensities (amplitude-dependent) propagate in a building, structural damage can be produced e.g., cracking of foundation walls or excessive sloping of floors.

Furthermore, the soil particularly dampens vibrations at high frequencies, so most of the vibration spectrum that reaches the structures is below 100 Hz. As the natural frequencies of many buildings are below 10 Hz, the ground shifts the vibration of the track to a range more likely to resonate with structures [13].

Resonance magnifies the structural vibration intensity due to the significant increase of the amplitude of the waves at a certain frequency. This phenomenon occurs when the frequency of vibrations reaching a building are equal or close to its natural frequency, which is the frequency at which a system tends to oscillate after being excited by an external force. All systems have a natural frequency at which they vibrate and most of them have many natural frequencies. Resonance must be specially studied as it can affect the building itself, as well as sensitive equipment.

Figure 2.3 represents the increase of transmissibility as the frequency approaches the natural frequency in a mechanical oscillatory system. When studying vibrations, *transmissibility* is defined as the ratio of the force transmitted into some building member to the force firstly

generated by an external agent and that will be transmitted. A transmissibility higher than the unit means amplification, i.e. increase of amplitude, and decrease of damping.

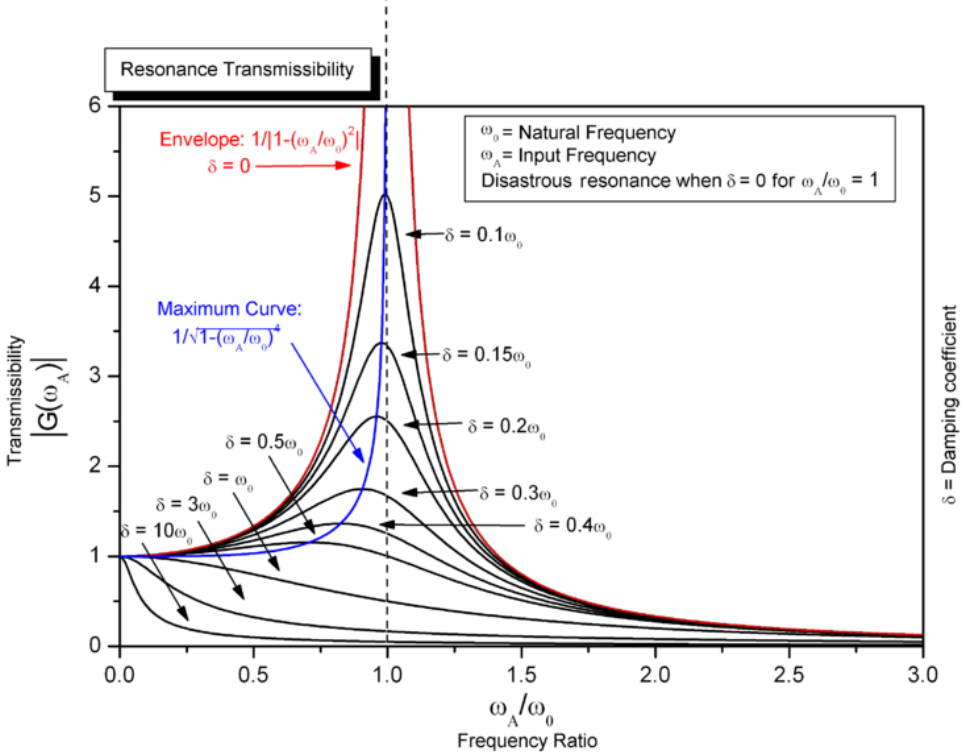

Figure 2.3: Resonance transmissibility as a function of the ratio of natural to input frequencies in a mechanical oscillatory system [19].

Each of the natural frequencies at which a given system oscillates has a vibration mode associated with it. In the case of structures, these different vibration modes define the shapes in which a structure will deform when excited, the first mode being the one associated with the lowest frequency at which vibration occurs. The sum of the different excited modes results in the complex pattern that can be measured in a physical domain.

As the modes of vibration are associated to higher frequencies they usually also become more complex shapes which require more energy to be excited in comparison to the more simple low frequency modes.

The study of vibration modes is not only relevant in the buildings under study, but also in the railway infrastructure. Vibrations that propagate through the track before reaching the ground can be amplified if some of the natural frequencies of the track system are excited.

Figure 2.5 shows the four first flexible mode shapes of the slabs used in an embedded rail

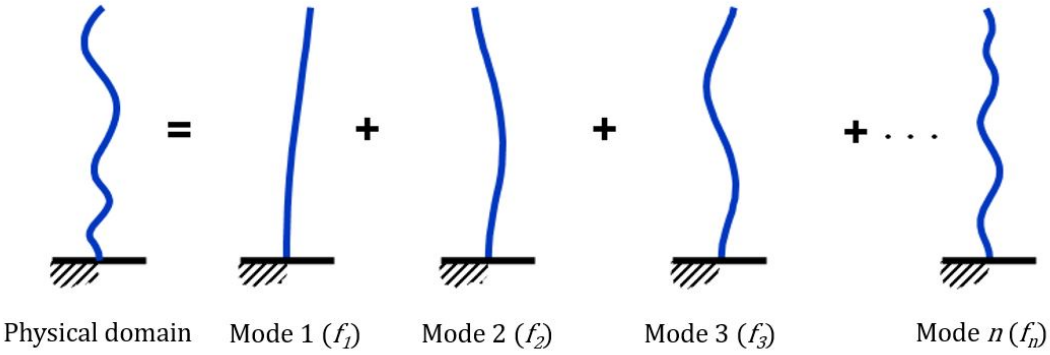

Figure 2.4: A complex vibration pattern separated into a set of vibration modes.

track model [20]. The frequency of the highest mode is 109 Hz, which is enough to simulate the dynamic behaviour of the track slabs as the structural resonant frequency of embedded rail structures is usually below 80 Hz.

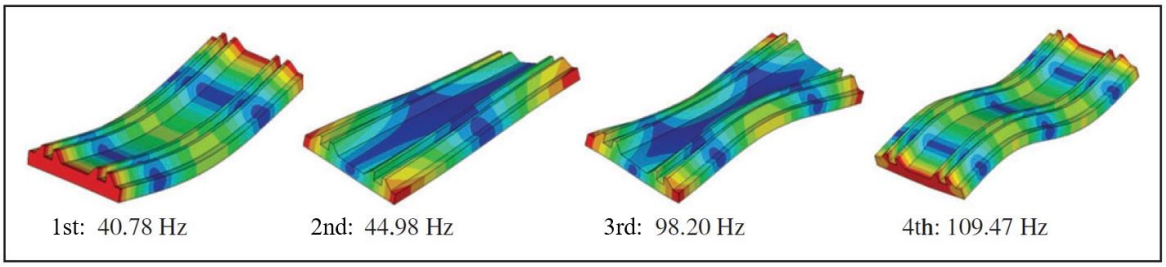

Figure 2.5: Flexible modes of the slabs in an embedded rail track model [20].

2.2 Possible sources of rail-induced ground-borne vibrations

Knowing and understanding the characteristics of the main sources of ground-borne vibrations caused by the passing of urban trains is essential for the simulation of excitation, which in turn determines the choice of a suitable predictive model. The literature generally agrees on the identification of the main sources of vibrations due to urban rail traffic, presented below.

2.2.1 Moving load effect

The moving load effect is due to the self-weight of the railway vehicle that causes a quasi-static track deflection. Quasi-static forces arise from this effect and dominate the track response and near field. Furthermore, these forces are time dependent but are "slow" enough such that inertial effects can be ignored [21]. The moving railway is mostly represented as a constant load moving along a straight line on the surface of a half-space at constant speed. Many analytical

and numerical prediction models have been developed due to the extensive study of this problem for several years.

2.2.2 Distributed track unevenness

The lack of smoothness in the rail and wheel surface geometries makes the wheel-rail contact imperfect. This unevenness causes the wheel and rail to move vertically relative to one another and, thus, dynamic excitation is generated. These dynamic forces will lead to wave propagation in the ground.

There are several sources of distributed track unevenness. In the case of slab tracks, the geometric sources can be the unevenness at the surface of the rail, slab, or track bed and bent rail or slab during the initial deflection of the neutral line of rail or slab. In addition, the variation in stiffness of elements, such as the slab or the rail supports, also represents other possible sources of track unevenness [22].

When considering the rail surface, unevenness is most commonly caused by irregular wear or corrugation of the rail contact surface at wavelengths less than about 1 m (Figure 2.6). At much longer wavelengths, i.e., lower frequencies, it is due to undulations in the track bed [23].

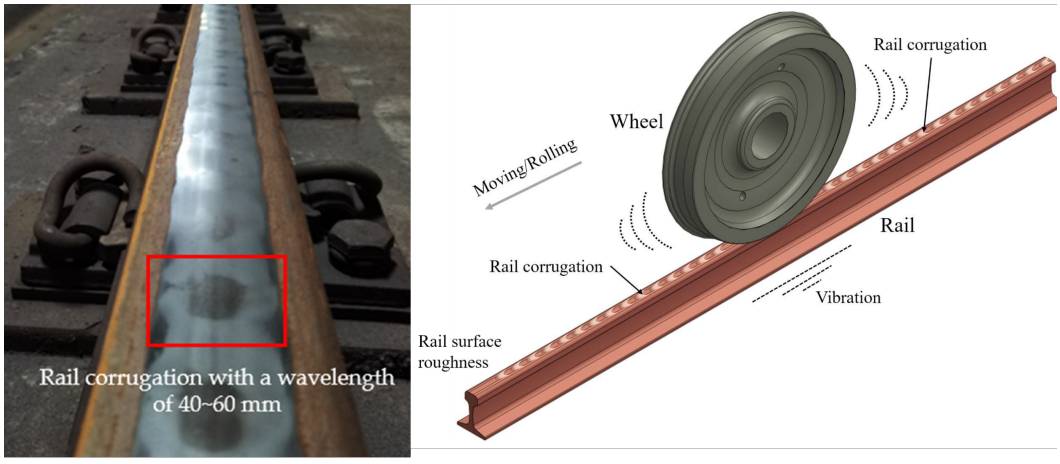

(a) (b)

Figure 2.6: (a) Example of a corrugated rail [24]. (b) Rail corrugation and vibration generated through the wheel-rail contact mechanism [25].

2.2.3 Localized defects at the wheel-rail interface

The impact forces occurring at each wheel rotation due to irregularities at the wheel-rail interface generate meaningful dynamic excitation and are the main contributor of rail-induced

ground-borne vibrations in urban rail transit even at low speeds [26]. These irregularities are caused by both defects in the rail and wheel-flats.

Singular defects on the rail such as flat spots (also known as squats) or crossings constitute changes in vertical geometry or stiffness which are the cause of the aforementioned impacts. An example of rail squat can be seen in Figure 2.7.

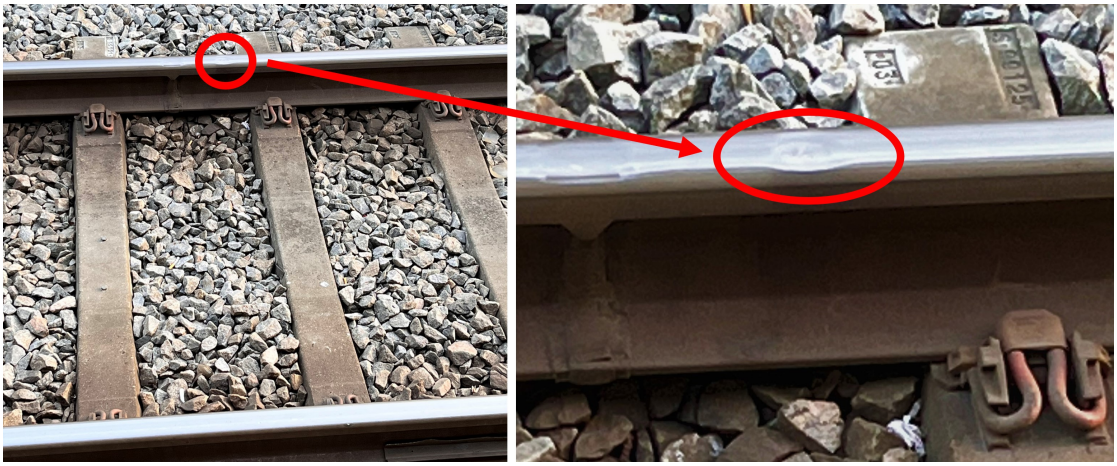

Figure 2.7: Squat defect on S-Train tracks at Svanemøllen station, Copenhagen. Image by Eyal Levenberg.

Wheel flats is the name given to defects on the wheel surface and occur when a wheel-set is dragged along the rail. These situations occur especially in emergency braking or slip and slide conditions that lead to the wheels locking while the train is still in motion. An example of a real wheel flat and how it is usually represented schematically is shown in Figure 2.8.

In some cases, the study of the dynamic effect of the wheel flat can be related in orders of magnitude to the problem of localized defects in the rail. The level of vibrations generated is also similar, as well as the repetitiveness occurring at one or more positions on the wheel circumference [27].

2.3 Common vibration mitigation measures

Given the major problem of ground borne vibrations generated by urban railway lines, various measures have been developed to mitigate them, either by reducing vibrations at source or by minimizing their propagation on the transmission path. The focus is not placed on measures at the receiver, such as base isolation of the building, as they are not as effective and economical as the previous types of measures [28].

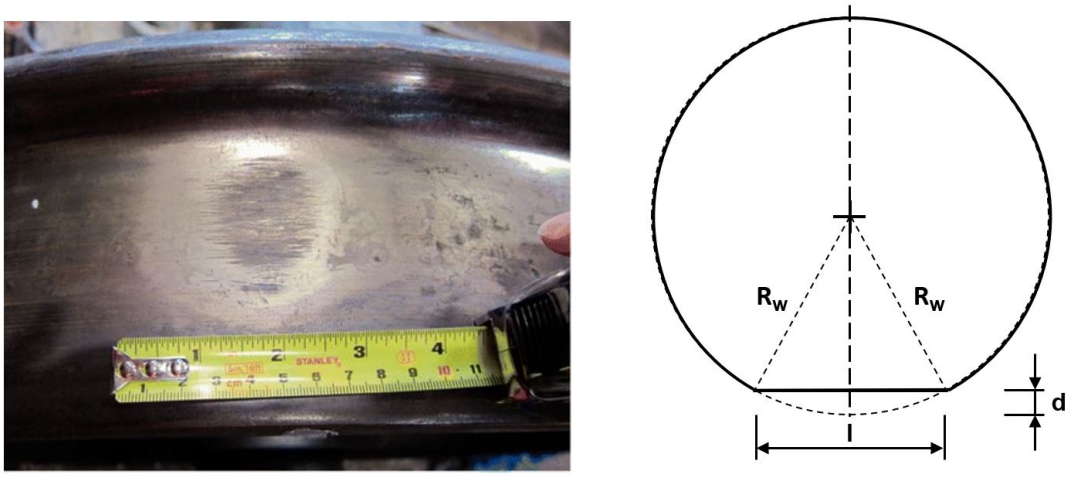

(a) (b)

Figure 2.8: (a) Example of a newly created wheel flat of approximately 3 centimeters length [27]. (b) Schematic diagram of an ideal wheel flat defined by the wheel radius R_w, and the defect dimensions, d and l [27].

2.3.1 Mitigation at source

Mitigating vibrations at the source can be achieved by reducing both wheel and track unevenness and defects that increase dynamic vehicle loads. For wheels, removing wheel flats by wheel reprofiling or truing avoids large impact forces. For minimizing track unevenness, methods such as reprofiling and rail grinding are used.

Vehicle dynamic impact forces can be also cut down through the modification of the rolling stock characteristics. The parameters of greatest influence are the stiffness of the primary suspension, which links the axlebox to the bogie frame, and the unsprung mass basically consisting of the wheelsets and other components directly connected to them (Figure 2.9) [29]. With a stiffer primary suspension and a heavier unsprung mass, one can expect higher vibration levels. Furthermore, in some cases, resilient wheels were found to reduce ground-borne vibrations generated by rail defects [30].

A third way of reducing ground-borne vibration is by including resilient elements at different levels in the track structure with the aim of isolating it dynamically. In the case of Embedded Rail System (ERS) tracks, very common in urban rail transport systems, some typical elements are resilient ERS strips placed under the rail, prefabricated rubber parts around the rail web (Figure 2.10), or damping mats beneath the concrete slab (Figure 2.11).

The rubber parts that function as rail bedding material not only elastically support and

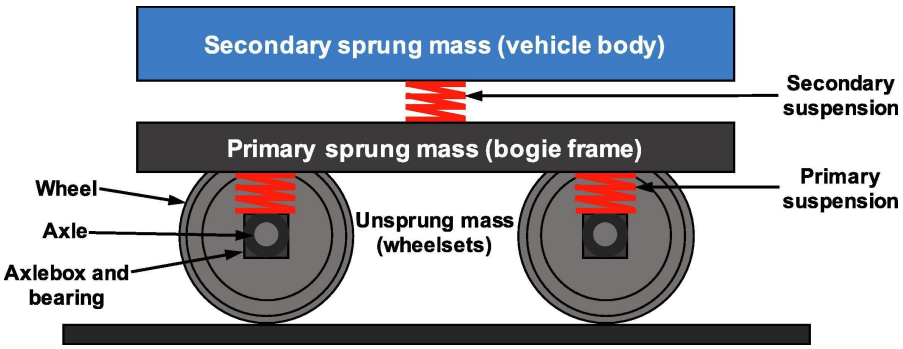

Figure 2.9: The mass breakdown and sprung environments of a rail vehicle bogie with outboard bearing wheelsets [31].

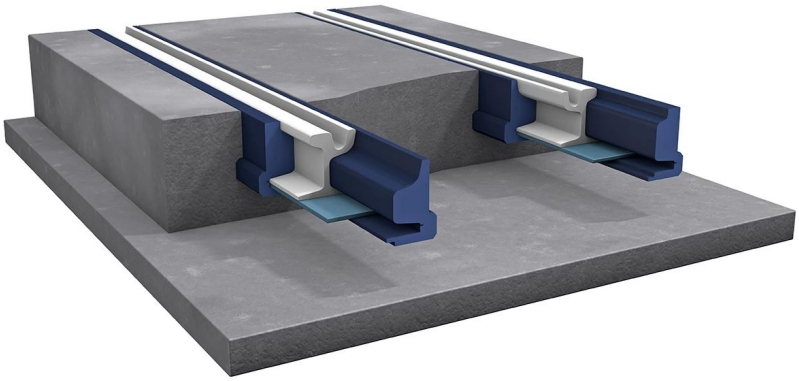

Figure 2.10: Continuously supported and fastened embedded ballastless track system developed by *Pandrol*. Rubber rail profiles in dark blue and ERS strip in light blue [32].

fasten the rail but also insulate its web. It has been proven that implementing continuously embedded rails reduces vibrations up to 8 dB in the frequency range between 5 and 400 Hz in comparison to standard discrete rail fixations to concrete slab [33]. This is caused by the elimination of metal-metal contacts present in the last system.

Elastomeric mats under concrete slabs are usually composed of two different layers. The upper layer is made of viscoelastic materials with high vibration damping ability such as resin-bonded rubbers with a thickness around 15-30 mm. The lower one is a non-woven protection layer of much lesser thickness.

Generally, a larger part of the track mass will be isolated and will work in a lower frequency range if the resilient elements are placed at a lower levels in the track [35]. That is the reason why slab damping mats in ERS and floating slab tracks are the best suited for treating ground-borne vibration, whereas other measures may be more efficient for the treatment of noise generation.

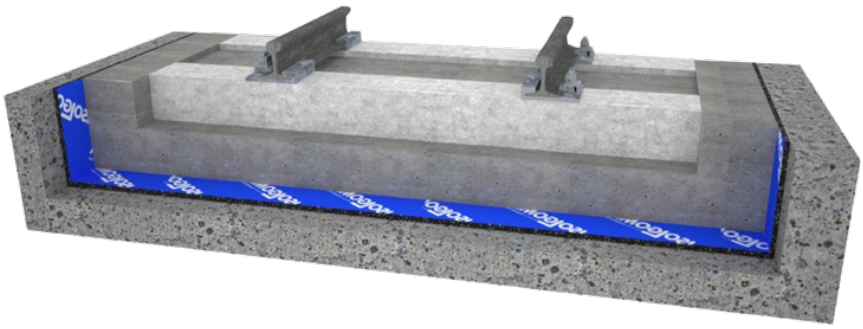

Figure 2.11: Continuous under slab mat MATRACK developed by *Isolgomma* [34].

The track stiffness should be as low as possible for an efficient vibration mitigation. Firstly, a stiffness decrease will affect the dynamic vehicle loads by lowering the natural frequency of the unsprung vehicle mass on the track stiffness. This can be easily checked in Equation 2.3, that gives the first and only natural frequency for a simple spring-mass system with one mass.

$$\omega = \sqrt{\frac{k_t}{M_u}} \tag{2.3}$$

Where k_t is the track stiffness and m_u is the unsprung vehicle mass.

Consequently, the frequency spectrum of the dynamic vehicle loads will be shifted to lower frequencies. This leads to an amplification of the dynamic vehicle load around the new (lower) resonance frequency and a reduction at higher frequencies, around the original natural frequency [35].

Second, resilient elements modify the track-soil transfer of vibrations by cutting-on frequencies of surface waves that mainly travel on top of the resilient layer. Again, vibrations amplify around the modified cut-on frequency while positive insertion loss values are found at higher frequencies.

In conclusion, the increased elasticity of the track superstructure through the insertion of resilient elements favors the damping of vibrations generated by dynamic effects at the wheel-rail interface. However, the track must be minimally stiff so as not to exceed the maximum allowable static deflection of the track. An excessively elastic track will have excessive deflections that will lead to track structural problems as well as increase the amplitude of vibrations due to the vehicle self-weight.

Finally, still in the field of mitigation at source, the subgrade stiffening technique under the

track is used to improve the bearing capacity in soft soils, avoiding excessive settlements in that area. But, in addition, in cases where quasi-static excitation is important, this process has also been shown effectively reduce ground-borne vibration levels [36].

2.3.2 Mitigation in the transmission path

Maximizing the distance between the track and the buildings is the most effective measure when it comes to reduce the propagation of ground-borne vibrations. However, this is rarely feasible in large cities with little land available. Other measures include the use of open trenches, that effectively cut off the propagation of Rayleigh waves if the depth of the trench is at least half the Rayleigh wavelength [37]. Trenches are especially employed to control at-grade track vibrations, although to be effective at very low frequencies the depth required becomes impractical for stability reasons [38]. Moreover, the presence of ground water jeopardizes the efficiency of this measure.

Concrete slabs, rows of concrete or steel piles, or jet grouting walls are used as stiff wave barriers embedded in the ground. They impede the transmission of waves that propagate through the soil when the wavelength of the incident waves is smaller than the bending wavelength in the stiff section [39]. In addition, they have the advantage of not presenting problems of stability or in conditions of high water table, as is the case with trenches.

Lastly, new mitigation measures based on placing heavy masses on the ground surface next to the track such as gabion walls or concrete blocks have been proposed. Some recent research shows that the use of masses for mitigation purposes offers the possibility of reducing vibration at low frequencies [40].

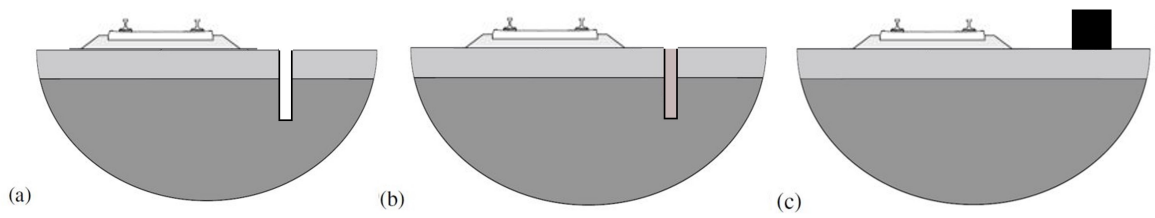

Figure 2.12: Vibration mitigation measures on the transmission path: (a) open trench, (b) stiff wave barrier, and (c) heavy masses next to the track [35].

2.4 Common modeling approaches for forecasting vibration features

A proper and accurate modeling approach is essential especially in the train-track interaction, which is the source of railway vibrations. If the vibration response is modeled inaccurately, then not only will the vibration of the track be erroneous, but this error will be carried over to vibration calculations on other elements: vehicle, ground and structures. The different modeling approaches for railway vibration prediction are presented below.

2.4.1 Numerical models

The prediction of ground vibrations in buildings is developed through a two-part process. First, the response to the passage of a train in the terrain is calculated and then, from these results, the response of the building is determined.

Focusing on the transmission part from the vehicle to the ground, numerical prediction models of railway-induced ground vibrations are generally obtained by coupling submodels for the train, the track and the ground. The dynamic behavior of the vehicle is often represented by a simple multibody vehicle model, whereas capturing the dynamic behavior of the track and ground requires much more computational and modeling effort. Moreover, to obtain an accurate numerical prediction of ground-borne vibrations, detailed information on soil dynamic parameters and characteristics that can be derivable from in-situ geophysical testing is needed.

The prediction of the induced wavefield usually also consists of two steps. First, the train-track-soil interaction problem is solved with the aim of calculating the dynamic vehicle loads; for example, assuming a perfect contact between train and track or crosswise invariance of the track geometry [29]. Second, the vehicle dynamic loads are applied to the track and the free-field response is calculated. This can be done using a transfer function $H(x, x', t)$ that links the response at a point x' on the ground to the load at a point x on the track for a time instant t.

Finite element methods (FEM) offer the greatest flexibility in modeling, but at a high computational cost. One reason is that numerical models suffer from spurious reflections at truncated model edges. For non-complex geometries, such as soil masses, absorbing boundaries can be used; however, for more complex track-type models, these boundary conditions are difficult to apply [13]. Therefore, when numerical methods are used, the total length of the modeled track must be much larger than the region of interest.

In addition, there are other important limitations in the use of numerical models that can be attributed to uncertainties in the model and in the parameters employed in it. The

simplifications introduced for modeling may be too constraining for the model to be useful. The track and soil geometry may vary or be non-periodic, for example, due to the existence of transition zones in the track, sloping soil layers or heterogeneities in the ground.

2.4.2 Analytical models

Analytical models are attractive because they are more computationally efficient compared to numerical approaches, the limitations of which were discussed in Subsection 2.4.1.

As a result, analytical models have been widely analyzed, especially before the arrival of high-powered computing. Traditional approaches used to track modeling are based on the assumption that the rail can be modeled as a single beam (typically Euler-Bernoulli) resting on a continuous Winkler-type support. This support has been used to describe the track or a combination of track and soil. Thus, this approach often models the track as a homogeneous material.

Subsequently, it was found that the accuracy of the model can be improved by replacing the Euler beam formulation with that of a Timoshenko beam. Timoshenko beam theory takes into account additional degrees of freedom (shear forces) compared to Euler beams and thus allows more accurate modeling of the track dynamics.

Two-layer models are also available, which are considered an improvement over single-layer models, as they allow other track elements to be simulated. Both this and the previous models are associated with the assumption that the track response can be reduced to two dimensions, considering the invariance of the transverse dimension.

In the case of the embedded rail system (ERS) track, the track elements in a two-layer model can be the rubber profile surrounding the rail, the concrete slab in which the rail is embedded, or vibration mitigation elements such as damping mats. A continuously supported two-layer model for a ERS track is presented in Figure 2.13.

Similar to the development of analytical models, research has been done to try to include soil stiffness contributions in track response calculations [13]. The most common approach to accomplish this is to model the soil as a linear elastic half-space. In these cases, the soil model is included only to increase the accuracy of the track model, since it is the track response that is of interest, not the far-field soil vibrations.

The role of the soil in the transmission path can also be modeled analytically using analytical expressions describing wave propagation in a homogeneous half-space due to different types of loads. The groundwork for the development of these solutions was established by Horace

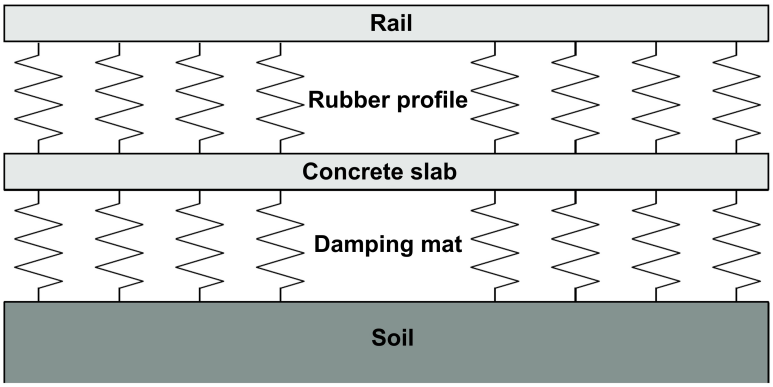

Figure 2.13: Continuously supported two-layer model for an ERS track.

Lamb. However, modeling the track-soil system involves making many assumptions to reduce the complexity of the model. For this reason, numerical methods have become more popular, as they are better suited to simulate complexities in the ground.

2.4.3 Empirical models

Despite recent significant advances in developing numerical models for railway-induced ground vibrations, these are still mainly used for research. In contrast, empirical methods are still primarily used in engineering practice [29].

The types of empirical approaches for vibration prediction change during the different stages of a project, and a distinction is made between scoping models (earliest stage), environmental assessment models (planning process), and detailed design models (construction and design part).

One well-known example of an empirical method is the Transit Noise and Vibration Impact Assessment Manual. This document is the procedure developed by the Federal Transit Administration (FTA) of the U.S. Department of Transportation specifically for rail rapid transit systems. Both this and other empirical methods are intended to predict the quasi-stationary response during the passage of a train and can be presented in the following general form:

$$A(f) = S(f)P(f)R(f) \tag{2.4}$$

Where $A(f)$ is the magnitude of ground vibration to be estimated, $S(f)$ represents the source strength, $P(f)$ characterizes the propagation path, and $R(f)$ the receiver.

In the Detailed Vibration Assessment, included in the FTA's manual, $P(f)$ is determined from field measurements by adding the contribution of point sources at different positions along the track. The final result is what is referred to as linear source transfer mobility. The

line transfer mobility accounts for the energy transmitted through the soil due to a line source, i.e., a train on a track [41]. The source strength $S(f)$, which is called the force density, is determined from field measurements and the linear source transfer mobility. The force density represents the power per unit length introduced into the soil by the source [41]. A database of source strengths obtained at different locations can be used to predict ground vibration levels at locations where the transfer mobility of the linear source has been determined.

Compared to numerical models, this type of empirical methods accounts for vibration transmission characteristics at a given site by directly using measured transfer functions. Thus, the need for simplifying assumptions, such as identifying dynamic soil characteristics, is avoided. As a result, empirical prediction methods have proven their worth in practice by providing reasonable estimates of vibration velocity levels [29].

2.4.4 Hybrid models

The use of empirical methods is limited to cases where adequate characterization of source strength and vibration transmission is available. To overcome these limitations, empirical methods can be combined with numerical methods in a hybrid or semi-empirical prediction procedure.

Hybrid prediction methods are particularly attractive in the case of new tracks or rolling stock [29]. Numerical models can be used to evaluate the influence of rolling stock characteristics and track design on ground vibrations, avoiding the need for in-situ tests that possibly require the construction of test tracks. In the case of new tracks, a numerically predicted source intensity can be combined with an experimental transfer function or attenuation law that inherently takes into account the particularities of vibration transmission. These transfer functions can be determined in the absence of the track.

Hybrid prediction methods improve the accuracy of numerical models through a suitable characterization of vibration transfer while providing the flexibility of numerical models to evaluate a wide range of rolling stock and track parameters.

Another type of hybrid methods are semi-analytical models. These models help to overcome the obstacles of analytical models due to the complexity of the mathematical problems to be solved, which may involve complicated series or integral representations. Semi-analytical methods include techniques that allow reducing the mathematical complexity of the original analytical problem by providing an approximate solution to the one obtained analytically. For example, integral transforms such as the spatial Fourier transform are widely employed in soil modeling [42].

Chapter 3

Objectives and methodology

3.1 Objectives

The main objective of the thesis is to develop a theoretical methodology to predict intensities and characteristics of vibrations generated by light rail traffic. In addition, it is intended to analyze the effects of damping mats as a vibration mitigation measure.

3.2 Methodology

This section describes the methodology developed to meet the objectives described in the previous section. The methodologies presented cover the process of vibration generation and the whole transmission path. That process starts from the vibration source through the transmission by the different elements of the slab track until reaching the soil. Once there, the waves propagate up to the vibration receiver, a building nearby the track. A schematic representation of the transmission path with all the elements described above can be observed in Figure 3.1.

First, the quasi-static vibrations analysis due to the moving load effect, presented in Subsection 2.2.1, is studied. Second, the methodology for the dynamic analysis is introduced and considers both wheel flats and rail defects, featured in Subsection 2.2.3.

The developed methodologies are applied in the next chapter to the case study of the section of the future Ring 3 line as it passes through the DTU campus in Lyngby.

Once the case study results are obtained, they are analyzed, and conclusions are drawn from the analysis. Finally, the results are validated by comparison with other results obtained in similar projects.

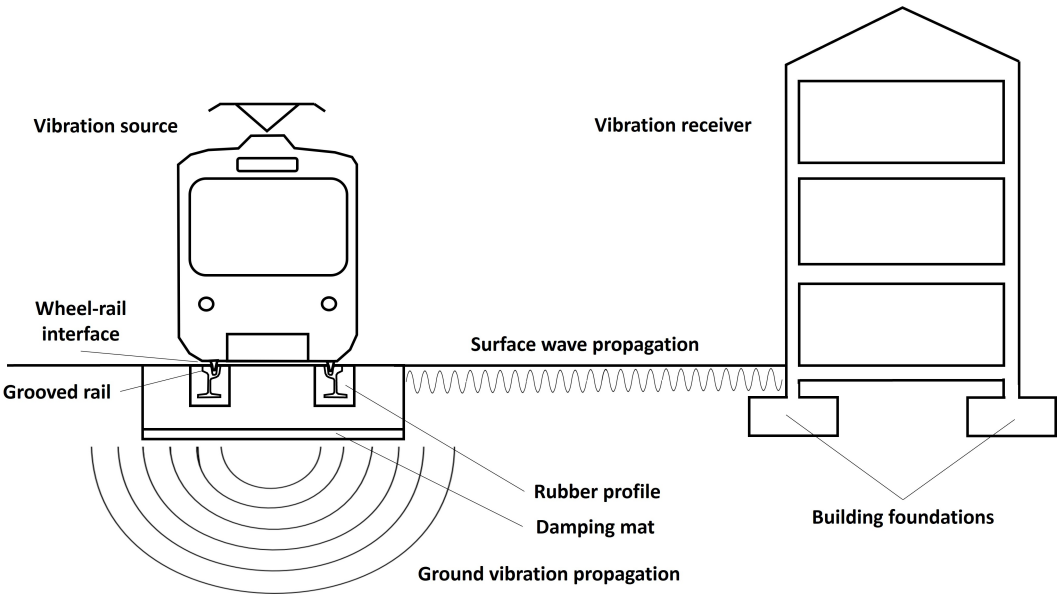

Figure 3.1: General scheme of the vibration transmission path (without scaling).

3.2.1 Quasi-static analysis due to the moving load effect

In this section a methodology is developed to study the moving load effect due to the vehicle's self-weight by means of a quasi-static analysis.

The analysis is based on the assumption that the rail behaves as an Euler beam continuously supported on an elastic foundation of Winkler type that represents the continuous rubber profile enclosing the rail, as depicted in Figure 3.2.

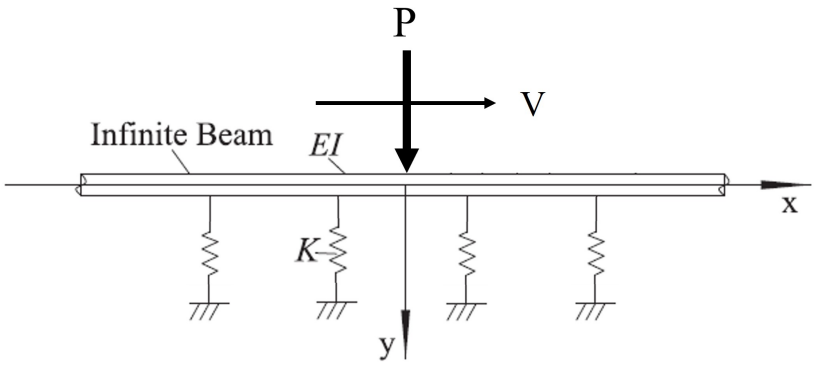

Figure 3.2: An infinite Euler beam continuously supported on a Winkler elastic foundation subjected to a point force P moving at a velocity V.

Equation 3.1 shows the expression of the deflected axis of an Euler beam subjected to a point force P [43] [44]. The elastic support of the beam is assumed to be continuum, horizontal

and uniform, i.e., constant modulus of elasticity, k.

$$y(x) = \frac{P\beta}{2k} e^{-\beta|x|} \left(\sin \beta|x| + \cos \beta|x|\right) \tag{3.1}$$

Where P is the static load applied by the wheel, k the modulus of elasticity of the elastic support and β is the support parameter, that represents a ratio of flexibility between the support and the beam. It is defined as:

$$\beta = \sqrt[4]{\frac{k}{4EI_x}} \tag{3.2}$$

Where E is the modulus of elasticity of the rail and I_x indicates the moment of inertia of the rail with respect to the x-axis.

Given the assumption of considering the support as purely elastic, the relationship between displacements and forces is given by the elastic modulus, k, of the rubber profile. Therefore, to obtain the loads transmitted under the rail per unit length along the rail direction, it is necessary to multiply the displacements obtained, $y(x)$, by k.

To analyze the displacements and loads induced by all the axes of the multiple unit (MU), several point loads separated are superimposed at distances corresponding to the vehicle's axle spacing, as shown graphically in Figure 3.3. This is made possible by the superposition principle, valid in this analysis since all materials are considered as elastic and linear.

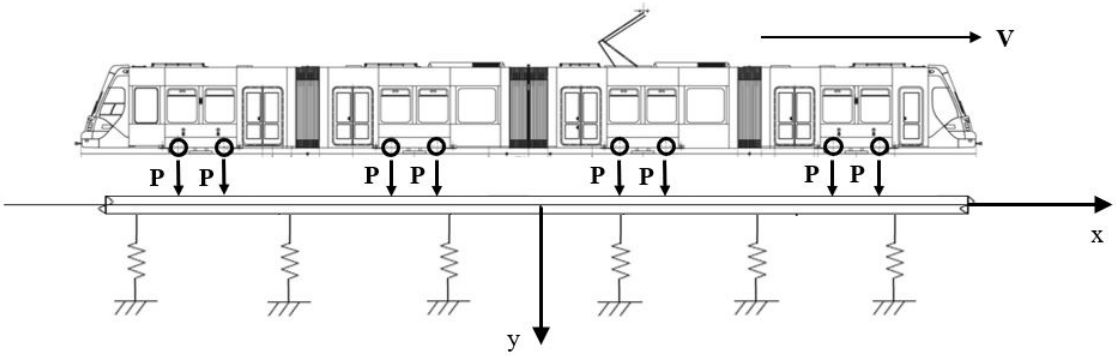

Figure 3.3: An infinite Euler beam continuously supported on a Winkler elastic foundation subjected to several point forces P representing all the axes of the MU and moving at a velocity V.

As the train advances over time, so will the displacement and loads under the rail due to the train's self-weight. That is why it is necessary to evaluate the length of the track section that

has an influence on the displacements occurring to the building of interest due to the moving load effect. For that purpose, and considering an ERS track composed of several concrete slabs separated by joints, it is first necessary to calculate the maximum load that can be transmitted to a concrete slab.

Equation 3.1 describes how the displacements are distributed along the rail due to a point load, but does not include the time variable, t. In order to study the evolution of displacement or load distributions over time, it is sufficient to add a term relating the position x to time t in Equation 3.1. This is where the speed of the convoy, v, comes into play, which multiplied by time gives the position for uniform rectilinear motion. After adding this term, Equation 3.1 becomes a function both of x and t (Equation 3.3).

$$y(x,t) = \frac{P\beta}{2k} e^{-\beta(|x|-vt)} [\sin\beta(|x|-vt) + \cos\beta(|x|-vt)] \tag{3.3}$$

By adding up all the axles and multiplying Equation 3.3 times the modulus of elasticity, k, the distributed load along the track as a function of position and time is obtained. If the resulting distributed load is integrated numerically over the length of a slab, a new expression, $Q(t)$, is obtained which is now only dependent on time. All that remains is to plot the resulting numerical expression to represent how a concrete block is loaded and unloaded with time during the passage of all axles of the MU. This concept is represented in Figure 3.4.

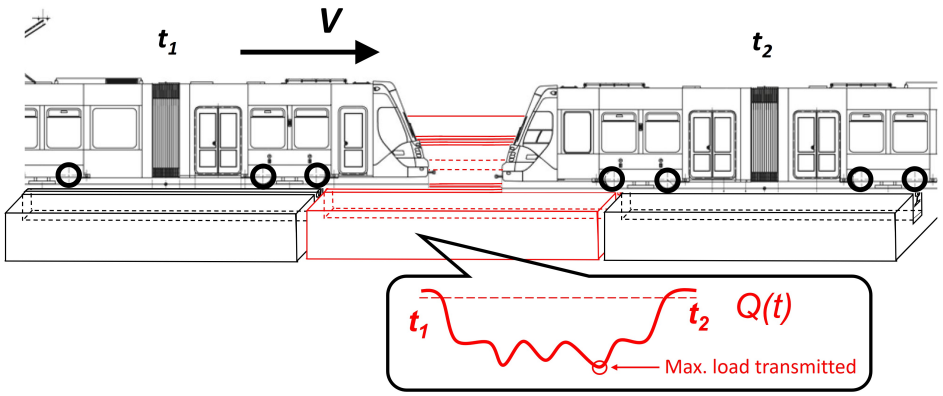

Figure 3.4: Loading and unloading over time for the whole of a concrete slab due to the passage of the train over it.

For the sake of simplifying the next calculations, it is assumed that the concrete slab is infinitely stiff and that the Saint Venant's principle is satisfied. This principle states that the difference between the effects of two different but statically equivalent loads becomes very small at sufficiently large distances from load [45]. Therefore, the uniform distributed load transmitted by the infinitely stiff slab is considered as an equivalent point load so that the

classical Boussinesq solution for a point load can be applied.

The Boussinesq theory makes it possible to determine the response at any point on the ground due to a force applied on the surface of an infinitely large half-space. This is represented in Figure 3.5 for a point load P and a random point on the ground N. The solution assumes that the point from which a response is obtained is located in a homogeneous, elastic and isotropic medium.

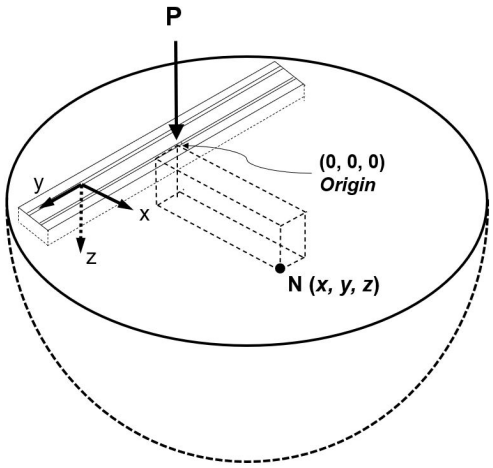

Figure 3.5: Infinitely large half-space where a force P is applied on the surface and the displacements at any point of the terrain N are to be known.

The displacements at a specific point on the ground due to a point force applied in the surface, $P(t)$, are calculated by means of the Boussinesq solution with Equations 3.4, 3.5 and 3.6 [46]. The coordinate system to be used is the one shown in Figure 3.5. The origin of coordinates is the point of application of the force $P(t)$ on the surface.

$$u_x = \frac{x\,(1+\nu)}{2\pi\,(x^2+y^2+z^2)^{0.5}}\left(\frac{z}{x^2+y^2+z^2}+\frac{2\nu-1}{z+(x^2+y^2+z^2)^{0.5}}\right)\frac{P(t)}{E} \tag{3.4}$$

$$u_y = \frac{y\,(1+\nu)}{2\pi\,(x^2+y^2+z^2)^{0.5}}\left(\frac{z}{x^2+y^2+z^2}+\frac{2\nu-1}{z+(x^2+y^2+z^2)^{0.5}}\right)\frac{P(t)}{E} \tag{3.5}$$

$$u_z = \frac{1}{2\pi}\left(\frac{2\left(1-\nu^2\right)}{(x^2+y^2+z^2)^{0.5}}+\frac{(1+\nu)\,z^2}{(x^2+y^2+z^2)^{1.5}}\right)\frac{P(t)}{E} \tag{3.6}$$

Where E and ν are elastic properties of the half-space, $P(t)$ is the point load applied at the coordinate origin, and u_x, u_y and u_z are the displacements in the x, y and z axes, respectively, of the ground point with coordinates x, y and z.

Once the load over time to which a slab is subjected, and that is directly transmitted to the ground, is known, it is possible to determine the value of the maximum load transmitted, as indicated in Figure 3.4.

Inserting this value as $P(t)$ in Equations 3.4, 3.5 and 3.6 it is possible to assess the evolution of the surface displacements in the receiver location as a function of the distance from this fixed location to the vehicle on the x, y and z axes. Based on these results, the number of slabs along the track that influence the response under the receiver can be estimated, and, therefore, be the ones to be used in the analysis.

Once the section of track to be studied has been determined, the next step is to calculate the total displacements in each direction, u_x, u_y and u_z, under the receiver building. This is achieved by inserting the time-dependent load, $P(t)$, transmitted by each slab into Equations 3.4, 3.5 and 3.6 taking into account the position of the receiver with respect to each slab.

To analyze the response of a building to the vertical displacements calculated above, a mass-spring model is used. The columns are represented by springs while the slabs are modelled as masses. The model for analyzing the vibrations in a building structure due to vertical displacements is shown in Figure 3.6 for a 3 degrees of freedom linear system.

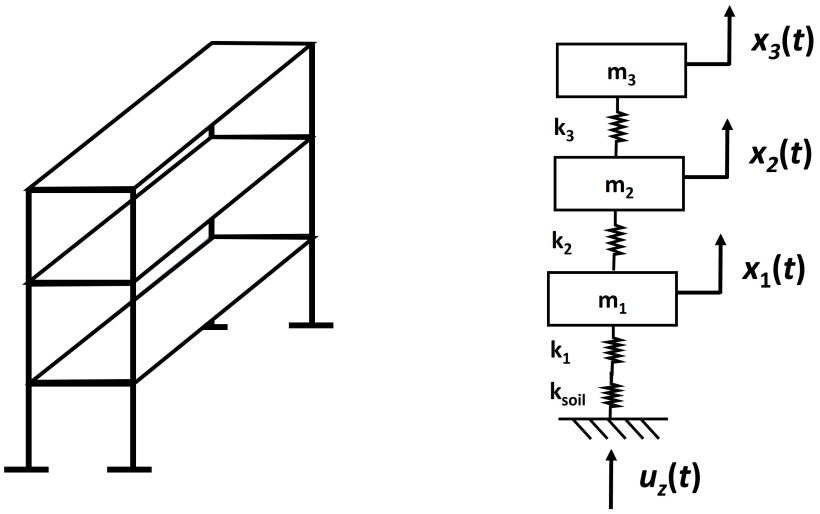

Figure 3.6: 3-storey building modelled with springs and masses subjected to an external force due to vertical displacements on the ground.

Although the building represented in Figure 3.6 has several columns, the mass-spring model is represented with only one spring per floor. For this, it is necessary to calculate a spring constant equivalent to all the columns going from one floor to another. Since these columns (modeled as springs) operate in parallel, the equivalent constant is calculated as the sum of the

coefficients of each of the parallel springs (Equation 3.7) [47].

$$k_n = \sum_{i=1}^{n} k_i \tag{3.7}$$

Where k_n denotes the equivalent spring constant and k_i is the spring constant of each of the n springs in parallel.

In turn, the equivalent spring stiffness of the column and the soil where the displacement, u_z, reaching the building propagates is obtained with Equation 3.8. This formula is based on the general expression for calculating the equivalent stiffness in a system of two springs in series.

$$\frac{1}{k_{eq}} = \frac{1}{k_1} + \frac{1}{k_{soil}} \tag{3.8}$$

Where k_{eq} is the equivalent spring stiffness, k_1 is the column spring stiffness and k_{soil} denotes the soil spring stiffness.

From Equation 3.8, it follows that if the stiffness of the soil is much greater than that of the column, the resulting equivalent stiffness will be very similar to that of the column and, therefore, the soil will have little influence on load transmission. In the opposite case, if the two stiffnesses under consideration are equal, the equivalent stiffness turns out to be half of each of the stiffnesses in series separately.

Therefore, if the stiffness of the soil is significantly higher than that of the column, it is possible to simplify the system in Figure 3.6 and only consider the stiffness of the column.

The vertical soil spring stiffness, k_{soil}, can be calculated using Equation 3.9 [48]:

$$k_{soil} = \frac{GL}{1-\nu}\left[0.73 + 1.54\left(\frac{B}{L}\right)^{0.75}\right] \tag{3.9}$$

Where L and B are the length and width of the column cross-section, respectively. G is the shear modulus of the soil, which is given by Equation 3.10.

$$G = \frac{E}{2\,(1+\nu)} \tag{3.10}$$

Where E and ν are the modulus of elasticity and Poisson's ratio of soil, respectively.

The spring stiffness of a column with rectangular cross-sectional area BL is calculated with Equation 3.11 [49].

$$k = \frac{3EI}{l^3} \tag{3.11}$$

Where E is the Young's modulus of the column's material, l denotes the column's length and I is the polar moment of inertia of the cross-sectional area, obtained by using Equation 3.12.

$$I = \frac{bh^3}{12} \tag{3.12}$$

Where b is the column's width and h its thickness.

In order to obtain the system's equation of movement (EOM), the Newton's second law is applied in each mass of the system with 3 degrees of freedom shown in Figure 3.6. The system of equations in Equation 3.13 shows the EOM for the system's masses, which are linear ordinary differential equations [50]. These equations are coupled with each other.

$$\begin{cases} m_1 x_1'' + (k_{eq} + k_2)(x_1 - u_z) - k_2 x_2 = 0 \\ m_2 x_2'' + (k_2 + k_3) x_2 - k_2 (x_1 - u_z) - k_3 x_3 = 0 \\ m_3 x_3'' + k_3 x_3 - k_3 x_2 = 0 \end{cases} \tag{3.13}$$

Where m_1, m_2 and m_3 represent the masses; k_{eq}, k_2 and k_3 are the spring stiffnesses and u_z account for the external vertical displacement transmitted from the soil and calculated with Equation 3.6.

Equation 3.13 can be rearranged in a matrix form in order to simplify the application and manipulation of analytic methods. This is shown in Equation 3.14.

$$\begin{bmatrix} m_1 & 0 & 0 \\ 0 & m_2 & 0 \\ 0 & 0 & m_3 \end{bmatrix} \begin{Bmatrix} x_1'' \\ x_2'' \\ x_3'' \end{Bmatrix} + \begin{bmatrix} k_{eq} + k_2 & -k_2 & 0 \\ -k_2 & k_2 + k_3 & -k_3 \\ 0 & -k_3 & k_3 \end{bmatrix} \begin{Bmatrix} x_1 - u_z \\ x_2 \\ x_3 \end{Bmatrix} = \begin{Bmatrix} 0 \\ 0 \\ 0 \end{Bmatrix} \tag{3.14}$$

To get the natural frequencies of each of the floors of the building, it is necessary to determine the eigenvalues that comply with the equality shown in Equation 3.15. The total number of eigenvalues or natural frequencies is equal to the total number of degrees of freedom in the model [51].

$$K\Psi = M\Psi D \tag{3.15}$$

Where K and M are the stiffness matrix and the mass matrix, respectively, shown in Equation 3.14. D is the diagonal matrix of generalized eigenvalues, and Ψ denotes the full matrix whose columns are the corresponding eigenvectors.

The natural frequency in one floor is given by 3.16, valid in a free vibration mass-spring system.

$$f = \frac{1}{2\pi}\sqrt{\lambda} \tag{3.16}$$

Where λ denotes an eigenvalue of the system, included in the diagonal matrix D.

Once the above results are obtained, it is possible to analyze if any of the building natural frequencies are excited by the vibrations in each of the floors due to the moving load effect of the train. In this way, a potential resonance phenomenon can be predicted.

The elastomeric mat under the concrete slab was not considered in the previous stages as it is intended to attenuate high-frequency vibrations due to dynamic loads. If, nonetheless, it is desired to analyze its effect on the transmission of quasi-static loads from the track to the ground under the ERS track, the already used model consisting of an Euler beam supported on a Winkler elastic foundation (Figure 3.2) must be adapted by adding a mass-spring-damper model with one degree of freedom. The mass represents one concrete slab supported in a damping mat, modelled by a spring and a dashpot.

The mass-spring-damper model is graphically represented in Figure 3.16 and its details and application are discussed in Subsection 3.2.2, since the inclusion of the anti-vibration mat in the model is of special relevance in the dynamic analysis.

3.2.2 Dynamic analysis due to irregularities in the wheel-rail interface

The dynamic excitation is mainly generated by irregularities at the wheel-rail interface caused by rail defects and wheel-flats. The dynamic analysis developed considers these phenomena and quantifies and evaluates their impact on vibration generation.

In the quasi-static analysis, developed in Subsection 3.2.1, it was assumed that the rail behaves as an Euler beam continuously supported on an elastic foundation of Winkler type. The quasi-static loads of the vehicle were modeled from the superposition of point loads, and the response of the beam could be obtained by traditional analytical solutions.

However, it is more complex to analyze the response of the beam when, instead of static loads, dynamic loads are applied. An example of this type of load, which is particularly relevant in this analysis, is the impulsive load, what consists of a charge of very short duration compared to the period of vibration of a structure [52].

Figure 3.7 shows an impulse load in both time and frequency domains. An impulse signal represented in the frequency domain by using the Fourier transform will have a constant amplitude throughout the entire domain [53]. This will only happen in the ideal case where a load is infinitely concentrated in the time domain, following the Dirac Delta function. In the example of Figure 3.7, the amplitude is no longer constant at around 1000 Hz due to the load duration of about 60 μs.

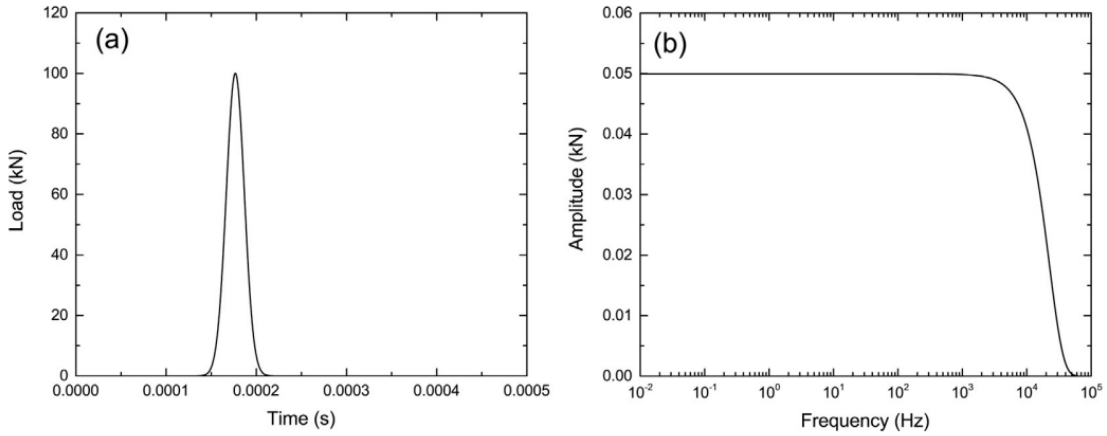

Figure 3.7: (a) Wave form of an impulsive load with time duration 60 μs and (b) its frequency characteristics [54].

If the track under study is not yet built, it is not possible to obtain data on the response to dynamic loads from measurements. One alternative option to address the problem is to take measurements in other sections of the same line where the construction process has already started. Another option is to try to perform the dynamic analysis analytically. Although the latter option is not as common as field work on practical problems in real life, it is the one chosen to start the calculations.

Yu and Yuan (2014) [55] developed an analytical solution for an infinite Euler-Bernoulli beam on a viscoelastic foundation subjected to arbitrary dynamic loads. More specifically, an analytical solution is presented for the particular case of impulsive loads, what is the most relevant for this analysis. According to the authors, an analytical solution dealing with the response of an infinite beam subjected to impulsive loads has not previously been developed in the literature.

The particularized solution for impulsive loads is particularly interesting because it makes it possible to analyze analytically the behavior of the rail encapsulated by the continuous rubber profile when it is subjected to one or more impacts due to a defect at the wheel-rail interface.

As already assumed in the quasi-static analysis, for the dynamic case it is also considered

that the rubber profile enclosing the rail is purely elastic, so the viscous damping coefficient, c, is taken as 0. Figure 3.8 depicts the described model: an infinitely long Euler-Bernoulli beam on a Winkler foundation subjected to an impulsive dynamic load.

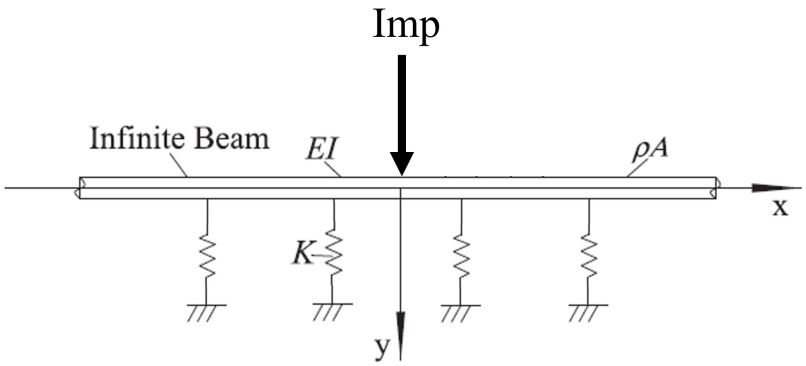

Figure 3.8: Infinitely long Euler-Bernoulli beam on a Winkler foundation subjected to an impulsive dynamic load, Imp, at $x = 0$.

Equation 3.17 shows the vertical deflection of an infinite beam subjected to a unitary impulsive load.

$$y(x,t) = \frac{1}{\pi}\frac{1}{\rho A}\int_0^{+\infty} \frac{\cos(ux)\sin[\beta(u)t]}{\beta(u)}du \tag{3.17}$$

Where ρ and A are the density and the cross section area of the beam, respectively. x represents the observation point at which the response to an impulsive load applied at the origin of the coordinate system ($x = 0$) is analyzed. t is the variable that represents the time from the instant in which the impulse under study occurred. Therefore, $t = 0$ is the time at which the load is applied. Finally, $\beta(u)$ is obtained with Equation 3.18.

$$\beta(u) = \sqrt{\frac{EI}{\rho A}u^4 + \frac{K}{\rho A}} \tag{3.18}$$

Where E and I are the beam Young's modulus and moment of inertia, and K is the modulus of elasticity of the elastic foundation that supports the beam.

After performing a dimensional analysis of Equation 3.17, it is concluded that this expression has units of displacement divided by force and time. An impulse is the integral of a force over the time interval for which it acts, so its units are force times time. Thus, the output of Equation 3.17 is a value that represents displacement divided by impulse. Consequently, a total displacement is obtained by multiplying that result by an impulse value.

The impulse, $m_{eq}\Delta V$, produced by a wheel flat on an elastically supported rail is quantified from Equation 3.19 [56]. This expression is valid as long as the speed at which the vehicle is running is less than the critical speed of the train above which the wheel separates from the rail.

$$m_{eq}\Delta V = v m_{eq}\sqrt{\frac{2h}{a}} \tag{3.19}$$

Where $m_{eq}\Delta V$ represents the rail impulse, h is the wheel flat height, a is the wheel radius, and v accounts for the train speed. m_{eq} is the the equivalent impact rail mass for resiliently supported rails, which can be estimated approximately according to Equation 3.20 [56].

$$m_{eq} = 0.4\rho_l \tag{3.20}$$

Where ρ_l is the mass of a 1-meter length of rail.

Due to the low speeds of light rail traffic it seems acceptable to assume that the critical speed is not exceeded and, therefore, that the wheel maintains contact with the rail. Furthermore, the critical speed for the case of a rail on a resilient support is higher than would be expected in the rigid case. In the latter situation the wheel must follow the shape of the irregularity, whereas in the elastic case both the wheel and the rail move up or down to follow the shape of the discontinuities [56].

Another interesting aspect of Equations 3.19 and 3.20 is that the only characteristic of the vehicle taken into account is its speed, v. Intuitively, one would think that the weight transmitted by a wheel plays an important role in quantifying an impulse. However, for frequencies below 1000 Hz, the wheel's motion is negligible compared to that of the rail. This is because the mechanical impedance, i.e., how much a structure resists motion when subjected to a harmonic force, is much greater in the wheel than in the rail in the range of frequencies below 1000 Hz [56].

To determine the impulse due to a rail defect, it is necessary to relate its geometry to the geometry of the wheel flat. Figure 3.9 shows the geometry with which a level defect on the rail and a wheel flat are modeled. At a level defect modeling a flat spot or squat on the rail (Figure 2.7), the wheel will experience a height decrease, h, equal to the sag of the circular arc with a chord, w. This can be seen in Figure 3.10.

Equation 3.21 shows the expression that approximately relates the arc sag, h, to the chord, w, and the radius, a, assuming that the sag is small compared to the radius [57].

$$h \approx \frac{w^2}{8a} \tag{3.21}$$

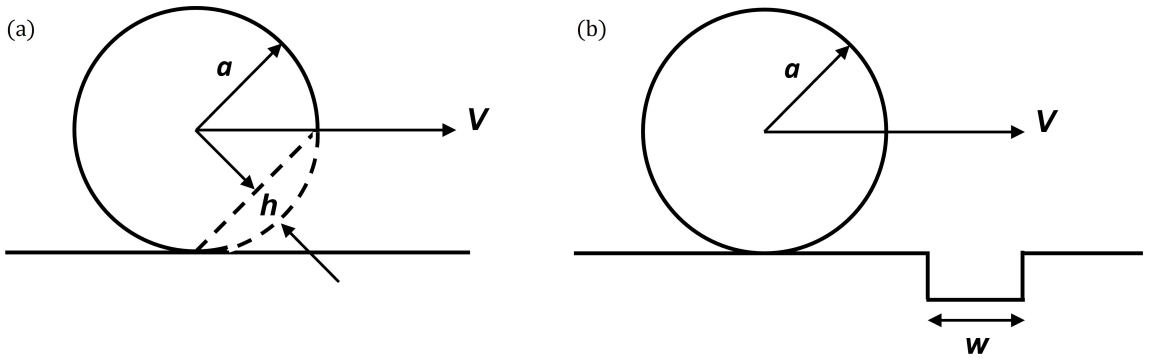

Figure 3.9: Geometric models of: (a) Wheel flat. (b) Level defect.

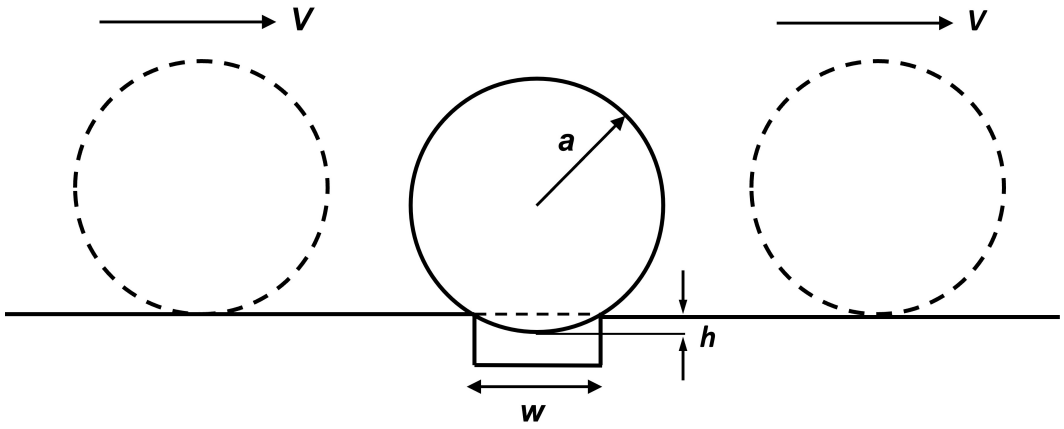

Figure 3.10: A wheel of radius a passing through a level defect with a length w.

By inserting Equation 3.21 into 3.19, the impulse for a level defect (Equation 3.22) is obtained.

$$m_{eq}\Delta V = v m_{eq}\frac{w}{2a} \tag{3.22}$$

Where $m_{eq}\Delta V$ represents the rail impulse due to a wheel impact in a level defect, w is the defect gap, a is the wheel radius and v accounts for the train speed. m_{eq} is the equivalent impact rail mass for resiliently supported rails, estimated with Equation 3.20.

As a result, with Equations 3.19 and 3.22, it is possible to obtain the impulses for the different types of defects which, multiplied with the results of Equation 3.17, provide a total displacement as a function of position, x, and time, t.

Once the total displacement, $y(x,t)$, under the rail due to an impact of the wheel with the rail is known, it is necessary to transform this displacement into a force. It will be this force the one transmitted to the top of the concrete slab, under the rubber profile that surrounds the

rail, as shown in Figure 3.11.

It suffices to multiply the displacements $y(x,t)$ as a function of position, x, and time, t, by the modulus of elasticity, k, of the elastic support to obtain the loads transmitted per linear meter of rail, q_1, due to one impulsive load. This transformation is valid as long as the assumption that the rail support is elastic is preserved.

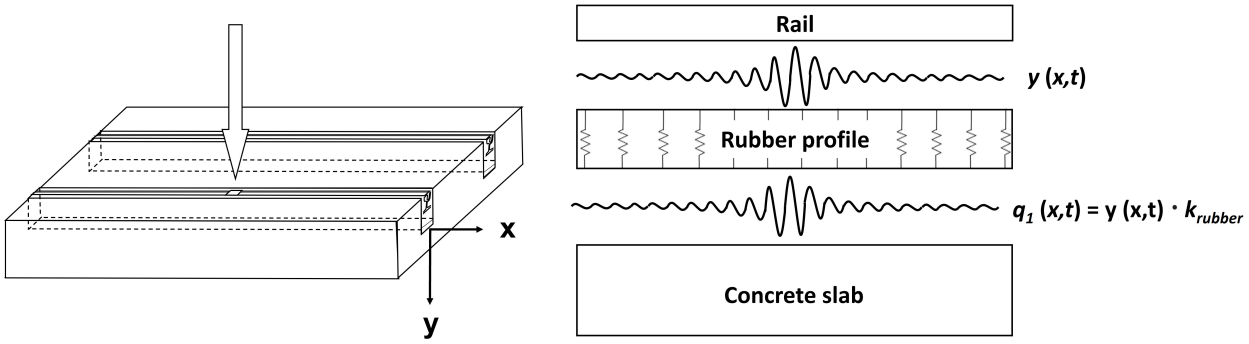

Figure 3.11: Longitudinal view of the track, generation of displacements under the rail due to impulsive loading, and transmission of distributed loads to the concrete slab.

By superimposing various impulse loads, it is possible to simulate the rail response to a wheel or rail defect. For a rail defect, the loads caused by the impacts of the different wheels with a rail defect are offset by the time elapsed since one wheel and the next wheel impact the defect, as shown in Figure 3.12. These time lags, Δt, are calculated from the relationship between the distance between axles of the vehicle and the speed at which the vehicle is moving assuming a uniform rectilinear motion.

In the case of a wheel flat, in addition to a time lag as in the case of a rail defect, there is also a change of position where the next impact occurs. The cycle starts with the damaged wheel impacting the track due to the wheel flat. The wheel will impact again once it makes a complete turn in a position at a distance of one wheel perimeter with respect to the previous impact. This is represented in Figure 3.13.

In sum, to calculate displacements in the case of a point irregularity at the wheel-rail interface, several results of Equation 3.17 corresponding to different values of x and t are added together. In the case of a rail defect the different values of t account for the time lags between the impact of the first wheel and that of each of the next wheels. For the wheel flat, in addition to different values of t, different values of x must also be considered. In contrast to the rail defect, the damaged wheel moves and will therefore impact at points separated at a distance equal to the perimeter of the wheel, disregarding the length of the wheel flat.

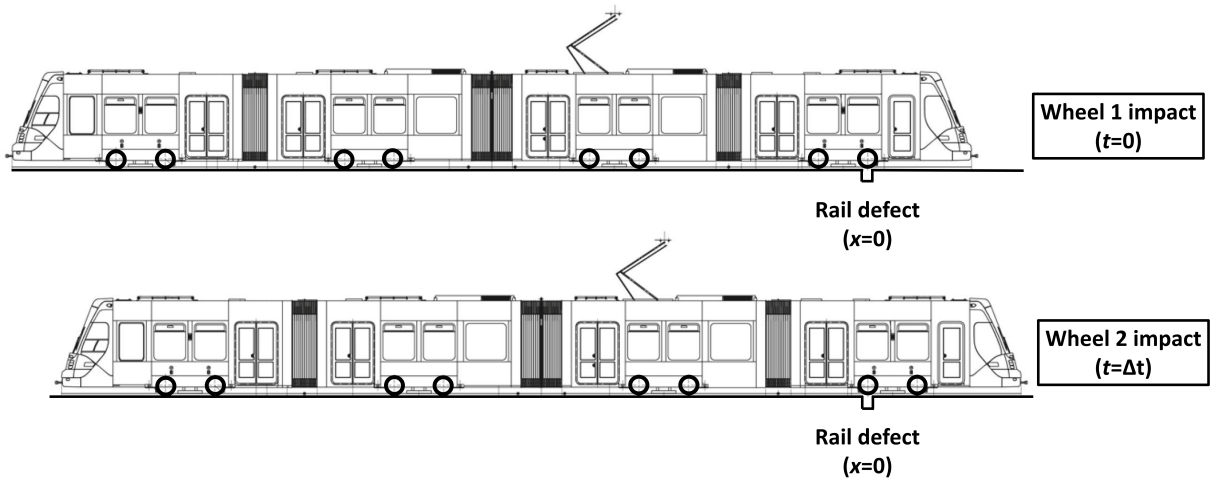

Figure 3.12: Representation of the impact due to a rail defect of two contiguous wheels that are offset by Δt.

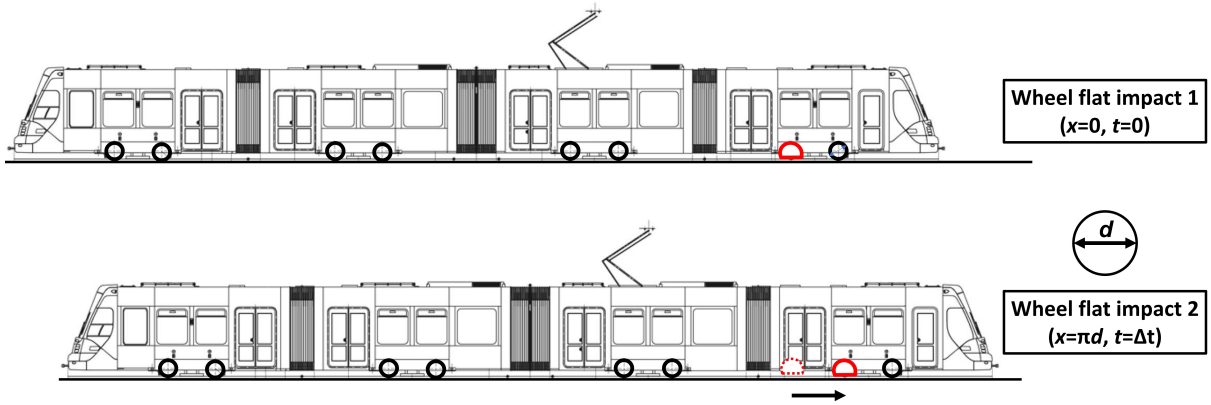

Figure 3.13: Representation of the impacts due to a wheel flat in one of the wheels.

At this point, the forces along the track transmitted to the concrete slab over time for various impulsive loads, $q_n(x,t)$, due to a point defect are known. It should be recalled that the relation between displacements under the rail and the distributed force per linear meter of rail is the modulus of elasticity of the rubber profile, k.

As in the quasi-static analysis, the track is assumed to be composed of infinitely rigid precast concrete slabs of length L connected by joints. For a slab of length L, the distributed loads are integrated along that length assuming that the defect is at the center of the rail span in the slab. With that location choice, a symmetrical force distribution $q_n(x,t)$ is achieved. The reason is that vibrations arising from the dynamic loading propagate equally on both sides of the impact. If the defect is taken at a position away from the center, the effect of the slab rotation should be considered.

The slab will transmit a load $Q(t)$ to the bottom track layers uniformly distributed over the entire area of the bottom face. This is valid for the assumption of considering the concrete as infinitely rigid, since this implies that it will not be deformed by the application of loads.

The above considerations are reflected in the graphical representations in Figure 3.14.

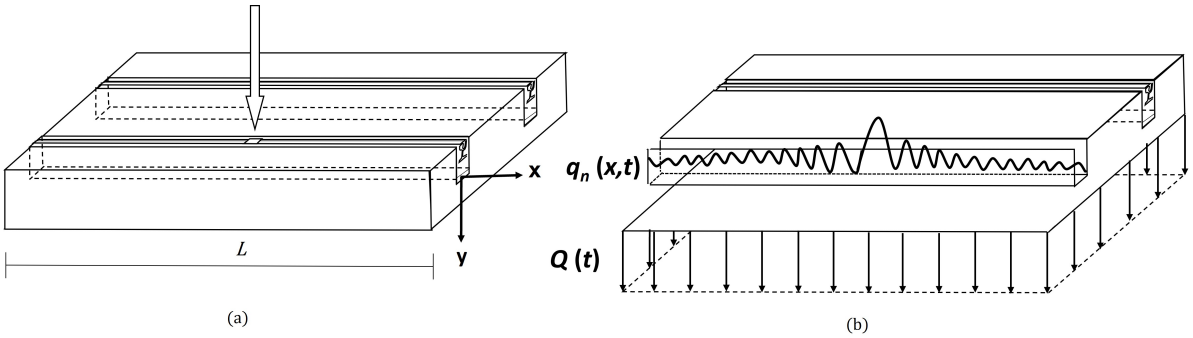

Figure 3.14: (a) Impulsive loading in a block with length L mid-point due to a punctual defect. (b) Load per linear meter of rail transmitted to the slab due to multiple impulsive loads, $q_n(x,t)$, and uniformly distributed load on the bottom face of the slab, $Q(t)$.

Applying Saint Venant's principle, it is possible to replace $Q(t)$ by an equivalent point load applied at the center of the bottom face of the precast slab, $F_o(t)$, (Figure 3.15). For this purpose, it is assumed that the distance between the vibration source and the receiver is long enough so that the effect of the two loads is similar.

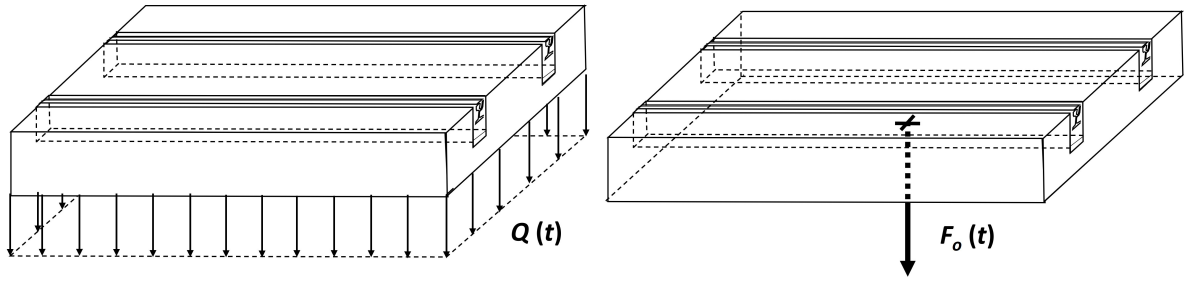

Figure 3.15: Two equivalent loads, $Q(t)$ and $F_o(t)$, transmitted from the bottom face of the concrete slab.

The next phase of the method focuses on the transmission of loads from the precast slab to the system formed by the anti-vibration mat on which the concrete slab rests and the soil. For this purpose, a mass-spring-damper model, already introduced in Subsection 3.2.1, is used and represented in Figure 3.16.

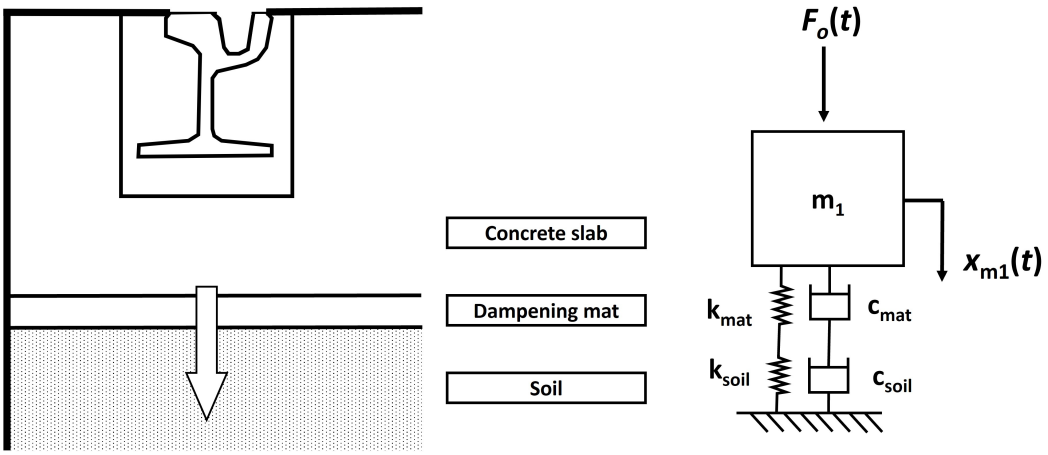

(a) (b)

Figure 3.16: (a) Load transmission from the block to the dampening mat-soil system. (b) Mass-spring-damper model for the load transmission from the block to the dampening mat-soil system.

The mass-spring-damper model is similar to the mass-spring model already employed in the quasi-static analysis (Figure 3.2). The difference between the two models is the existence of dashpots, also known as dampers, which reduce the oscillation of an oscillatory system. The damping coefficient, c, is the physical property of dashpots that quantifies how quickly the system returns to rest as the frictional force dissipates its oscillation energy [58]. In this model only linear viscous dampers are considered, in which the damping force is linearly proportional to velocity. That is, the faster the mass is moving, the more damping force is resisting that motion.

The equation of motion of the system has only one degree of freedom (Figure 3.16b) so Equation 3.23 is the one to be solved.

$$mx''(t) + c_{eq}x'(t) + k_{eq}x(t) = F_o(t) \tag{3.23}$$

Where m represents the mass of the slab, and c_{eq} and k_{eq} are the equivalent mat viscous damping coefficient and the equivalent spring stiffness of both the soil and the dampening mat, respectively. $F_o(t)$ accounts for the dynamic vertical force to which the concrete slab is subjected and which will be transmitted to the mat-soil system. x is the resulting vertical displacement over time of the mass, m.

The mass of the concrete block, m, is calculated by multiplying its volume, relative to its dimensions, by the density of the concrete.

The equivalent spring stiffness is obtained from Equation 3.24, based on the expression for calculating the equivalent stiffness in a system of two springs in series.

$$\frac{1}{k_{eq}} = \frac{1}{k_{mat}} + \frac{1}{k_{soil}} \tag{3.24}$$

Where k_{eq} is the equivalent spring stiffness, k_{mat} is the damping mat spring stiffness, and k_{soil} denotes the soil spring stiffness.

From Equation 3.24, it follows that if the stiffness of the soil is much greater than that of the mat, the soil will have little influence on load transmission. This was already discussed in Subsection 3.2.1, during the modeling of the receiver building (Figure 3.6). If the above is fulfilled, it is possible to simplify the system in Figure 3.16b and only consider the stiffness of the mat. The same applies to the dashpot and the viscous damping coefficient.

The vertical soil spring stiffness, k_{soil}, is calculated with Equation 3.9. In this case, L and B are the length and width of the slab, respectively.

Once $x(t)$ is determined in Equation 3.23, the loads transmitted to the ground under the track slab over time, $F(t)$, are calculated as expressed in Equation 3.25.

$$F(t) = c_{eq}x'(t) + k_{eq}x(t) \tag{3.25}$$

Where $c_{eq}x'(t)$ represents the resistive force against movement, i.e., damping and $k_{eq}x(t)$ is the restoration force of the spring trying to get back to the equilibrium position.

The next step is to use Fourier analysis to obtain the power distribution in frequency components that make up the time series of $F(t)$, i.e., its spectral density. For this, the Fourier transform, which is a mathematical transformation used to transform signals between the time (or spatial) domain and the frequency domain, must be used. If f is an integrable function in $\mathbb{R}$, the function $\mathcal{F}$ that defines its spectral spectrum, i.e., its Fourier transform, is given by the expression in Equation 3.26.

$$\mathcal{F}(\xi) = \int_{-\infty}^{+\infty} f(x)e^{-i2\pi\xi x}dx \tag{3.26}$$

Where the Fourier transform of f at a frequency ξ is given by the complex number $\mathcal{F}(\xi)$.

Equation 3.27 shows the Fourier transform of the function $F(t)$, whose frequency spectrum is to be known in this analysis.

$$\mathcal{F}(\xi) = \int_{-\infty}^{+\infty} F(t) e^{-i2\pi\xi t} dt \tag{3.27}$$

If Equation 3.27 is evaluated for all the values of ξ, a function in the frequency domain is produced, which is the one that allows the analysis of the main frequencies of the time series of $F(t)$.

At this point, the response at the point on the ground surface where an impulse is produced by a defect in the wheel or rail is known. To determine the response at another point on the ground due to the dynamic load $F(t)$; for example, where a building is located, it is necessary to study the wave propagation in the ground. As explained in Subsection 2.1.1, Rayleigh surface waves are the type of waves that carry the greatest amount of irradiated energy. Consequently, these are the ones chosen to study their propagation in the ground.

Maintaining the assumption of considering the soil as an isotropic and homogeneous half-space, and under the action of a harmonic force, $F(t)$, it is possible to link that force with the displacements at any point of the surface. This is achieved by means of the transfer functions, $H_u(\Omega_r r)$ and $H_w(\Omega_r r)$ shown in Equations 3.28 and 3.29 [59], which relate forces to horizontal and vertical components of the displacement, respectively. Figure 2.1a shows a graphical representation of the component decomposition of the Rayleigh wave.

$$H_u(\Omega_r r) = \frac{\Omega_r i H}{2G} \sqrt{\frac{2}{\pi \Omega_r r}} \mathrm{e}^{-i\left(\Omega_r r - \frac{3\pi}{4}\right)} \tag{3.28}$$

$$H_w(\Omega_r r) = \frac{\Omega_r i K}{2G} \sqrt{\frac{2}{\pi \Omega_r r}} \mathrm{e}^{-i\left(\Omega_r r - \frac{\pi}{4}\right)} \tag{3.29}$$

Where G is the shear modulus and H and K are material constants that depend only on the Poisson's ratio, and that can be found in [60]. Ω_r is the ratio of the angular frequency, ω, to the Rayleigh wave velocity, c_r, and r represents the distance between the point where the displacements are to be obtained and the force.

As mentioned above, the transfer function allows the force and each displacement to be related. This relationship, for the horizontal and vertical component of the displacement, is shown in Equations 3.30 and 3.31, respectively.

$$u(r,t) = H_u(\Omega_r, r) F \mathrm{e}^{i\omega t} \tag{3.30}$$

$$w(r,t) = H_w(\Omega_r, r) F \mathrm{e}^{i\omega t} \tag{3.31}$$

Where $F(t) = F\mathrm{e}^{i\omega t}$ is the complex notation for the harmonic force of amplitude F and angular frequency ω at an instant t. $u(r,t)$ and $w(r,t)$ are the horizontal and vertical components of the displacement, respectively, in a point with a distance r from the source due to the

harmonic force $F(t)$.

The elastic constants G, K and H of the soil are determined directly from the elastic modulus and Poisson's ratio. To compute the Rayleigh wave velocity, the approximate analytical expression given in Equation 3.32 can be used [61].

$$c_r = c_s \sqrt{\frac{30.876 - 14.876\nu - \sqrt{224.545376\nu^2 - 93.122752\nu + 124.577376}}{26 * (1 - \nu)}} \tag{3.32}$$

Where c_s is the shear wave speed, given by Equation 3.33:

$$c_s = \sqrt{\frac{G}{\rho}} \tag{3.33}$$

Where G is the shear modulus and ρ is the density of the soil.

Figure 3.17 shows the model of a track on the surface of a half-space and the harmonic surface displacements u and w in a point N in response to the harmonic force $F(t)$.

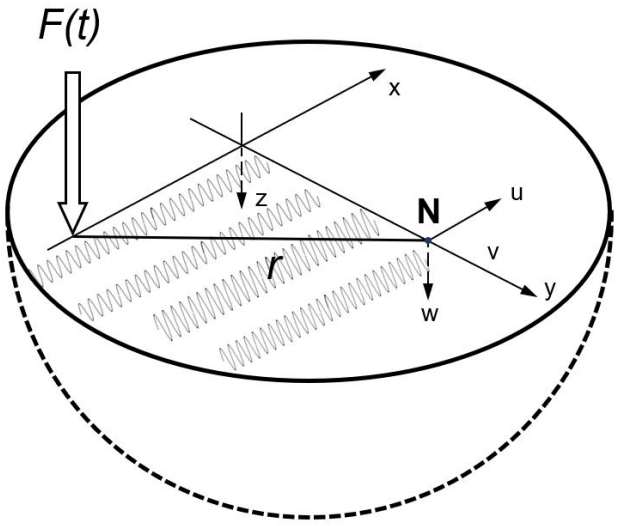

Figure 3.17: Model of a track on the surface of a half-space and harmonic surface displacements u and w in response to the force $F(t)$.

Once the main frequencies of $F(t)$ and the transfer functions applicable to Rayleigh waves are known, it is possible to estimate the response of the ground surface at any point of interest, including the location of the vibration receiver. If the receiver is a building whose vibration response is to be known, then the vibration transmission through the structure can be studied using the mass-spring model already introduced in Subsection 3.2.1 (Figure 3.6).

3.3 Assumptions and limits

The methodology developed in the previous sections is limited to urban rail transit and embedded rail tracks. For high-speed rail traffic, the approach to the problem of vibration generation changes completely. In those high-performance lines, the maintenance is much higher and, therefore, it is not usual to count punctual defects in the rail or wheel, where the standards are much more restrictive, among other differences.

Throughout the vibration characterization process, it has been necessary to make different assumptions to simplify the problem. These include considering some materials as homogeneous and elastic, assuming that the performance of different concrete slabs connected by joints is independent, or using the Saint-Venant principle regarding load distribution.

It can also be complex to characterize some elements, such as anti-vibration mats, due to the variability of their mechanical properties with temperature or the frequency and speed of the vibrations they dampen. For this reason, the analysis should consider different common values of properties such as spring stiffness and viscous damping coefficient that cover most cases in practice.

The cases covered by the analysis are also limited to those that do not compromise the rotational stability of the concrete slab. For example, regarding the position of a rail defect, only the case of one in the center of the slab has been considered. It could be the case that a defect is present at a point close to the ends of the slab, but in that case, the effect of a potential rotation would have to be taken into account.

Chapter 4

Vibration analysis case study: Ring 3 Letbanen at DTU

This chapter aims to bring the methodology presented in Section 3.2 to a real case: the section of the future Ring 3 light rail line running through the DTU campus in Lyngby. With this, it is analyzed how to apply the theoretical knowledge presented to practice, in addition to evaluating the results returned by the different solutions.

4.1 Quasi-static analysis

4.1.1 Inputs

To perform the quasi-static analysis to study the impact of the moving load effect, it is first necessary to have data on the rolling stock and the line operation, the track, and the soil where the vibrations caused by the moving train's self-weight propagate. The aim is to try to select inputs that approximate as closely as possible the characteristics of the section under study, which has not yet been built.

The rolling stock inputs are obtained from the technical data sheet of the Siemens Avenio [62], which is the tram unit that will run on the future Ring 3 line (Figure 1.3). Figure 4.1 depicts the side view of the four-car multiple unit to be acquired for the study project and table 4.1 shows the vehicle technical features employed in the quasi-static study. Furthermore, it is known that trams run at a maximum frequency of 5 minutes and that the maximum traffic speed on the study section will be 50 km/h [63].

According to the Surface Geology Map of Denmark available on the GEUS Jupiter Database [64], the predominant soil types in the DTU area are meltwater sand and clayey till. With these data, and based on typical ranges of values in similar soils [65], it has been chosen to

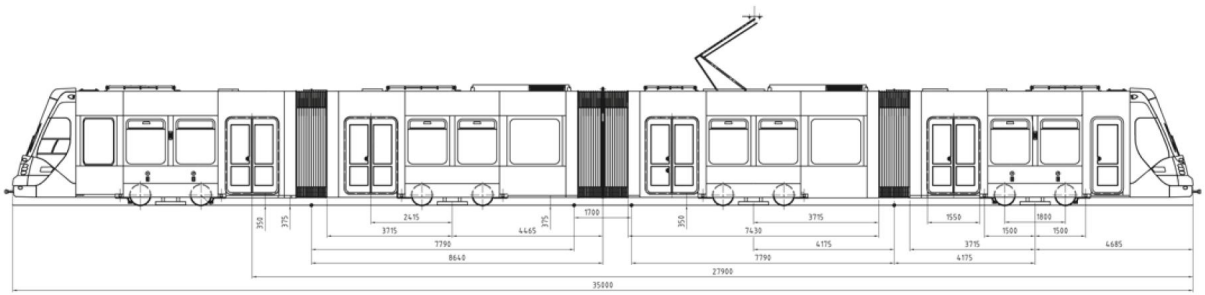

Figure 4.1: Siemens Avenio side view [62].

Rolling stock inputs	
Max. axle load	8.8 t
Vehicle length	35,000 mm
Max. operating speed	50 km/h
Time interval between trains	5 min
Axle distance in a bogie	1800 mm
Central cars bogie-bogie distance	8930 mm
Central car-end car bogie-bogie distance	8350 mm

Table 4.1: Vehicle technical data for the quasi-static analysis [62] [63].

characterize the soil with the properties listed in Table 4.2. In addition, the soil is assumed to be a homogeneous, elastic and isotropic medium in accordance with the classical Boussinesq solution to be used.

Soil inputs	
Modulus of elasticity (k_{soil})	$7 \cdot 10^7$ Pa
Poisson's coefficient (ν)	0.3
Density (ρ_{soil})	1600 kg/m

Table 4.2: Soil elastic properties for the quasi-static analysis [64] [65].

The track of study consists of 59R2 grooved rails, simply supported on the ERS LR 60R2 MS embedded rail system, on the groove of the slab track (Figure 4.2). The technical characteristics used in this analysis are obtained from the technical data sheet of the track manufacturer [66] and collected in Table 4.3.

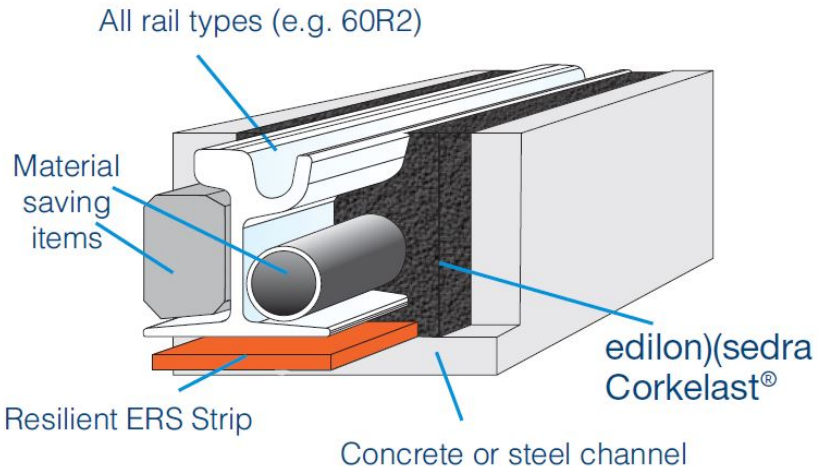

Figure 4.2: edilon)(sedra Embedded Rail System on the groove of the slab track [66].

Track inputs	
Rail Young's modulus (E_r)	$2.06 \cdot 10^{11}$ Pa
Rail moment of inertia about the neutral axis (I_x)	$3.21 \cdot 10^{5}$ m4
Rail weight per meter length (ρA)	58.2 kg/m
Modulus of Elasticity of the continuous rubber profile enclosing the rail (k)	$4.1 \cdot 10^{7}$ Pa
Concrete slab dimensions (length x width x thickness)	10x2.5x0.2 m
Density of concrete (ρ_c)	2500 kg/m^3

Table 4.3: Track inputs for the quasi-static analysis [66].

4.1.2 Calculations

Firstly, the displacement, $y(x)$, under the rail induced by one point load is studied applying Equation 3.1. Figure 4.3 shows the resulting displacement under one rail for a point load applied in $x = 0$. The point load represents the maximum load that can be transmitted by one wheel to one of the rails. For obtaining the load per unit length along the rail direction (Figure 4.4) it is sufficient to multiply the modulus of elasticity of the rubber profile, k, to the previous result.

The displacement under one rail due to the eight axle loads distributed among the four cars of the Siemens Avenio MU is represented in Figure 4.5 when the front axle is in $x = 0$. The load distribution along the track is again calculated with the previous result times the modulus of elasticity of the rubber profile, k, and shown in Figure 4.6.

The study now focuses on the behavior of the different concrete slabs, connected by joints,

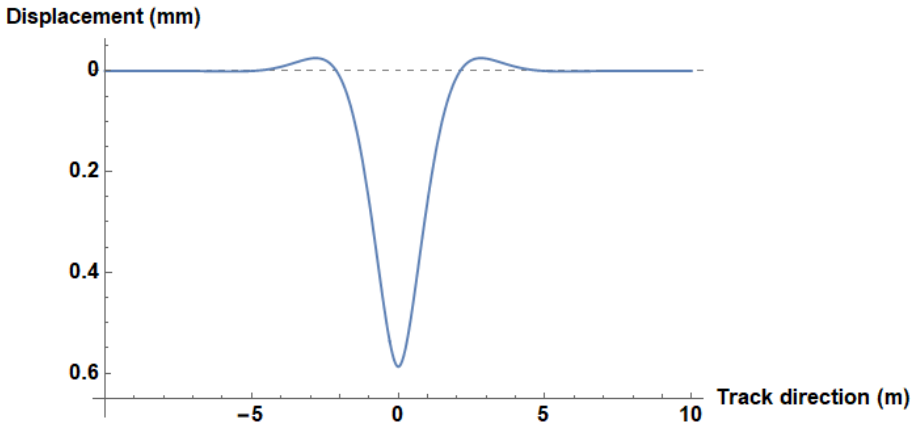

Figure 4.3: Displacement under one rail for the maximum wheel load applied in $x = 0$.

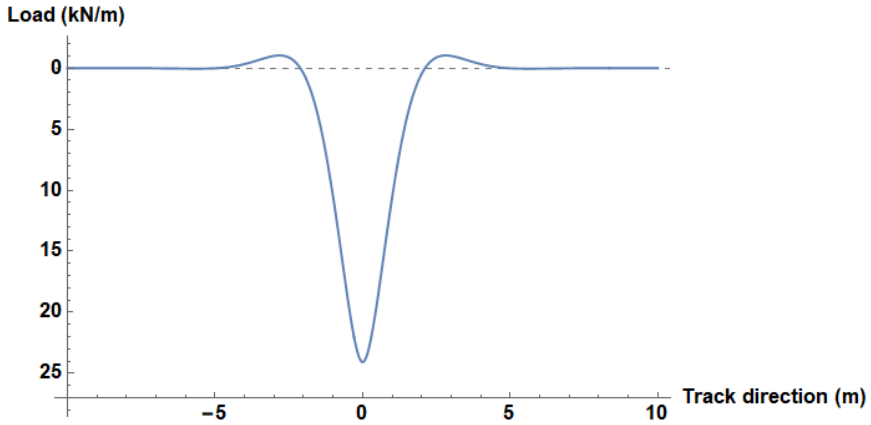

Figure 4.4: Distributed load under one rail for the maximum wheel load applied in $x = 0$.

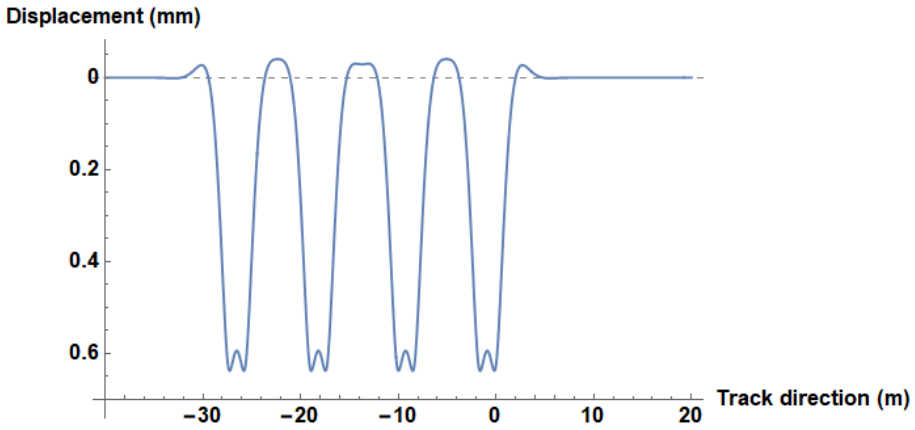

Figure 4.5: Displacement under one rail due to the total train weight when the front axle is in $x = 0$.

which form the Embedded Rail System (ERS). From Equation 3.3, which includes time, t, as an independent variable, it is possible to analyze how a slab loads and unloads as a vehicle

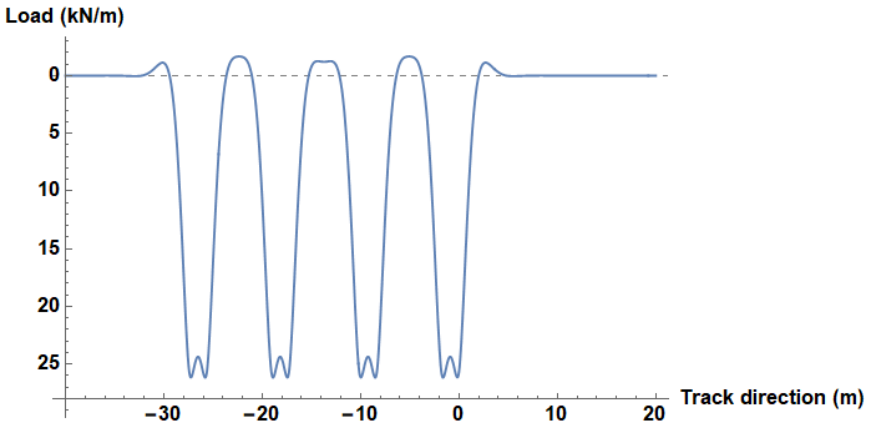

Figure 4.6: Distributed load under one rail due to the total train weight when the front axle is in $x = 0$.

passes through it. Figure 4.7 shows the total load over time on one slab with the dimensions given in Table 4.1. It should be noted that the total loads on the slab are the result of the loads transmitted by the two rails on the track. Therefore, it is necessary to multiply by two the results obtained previously, where the effect of one of the two axle wheels on a single rail was considered.

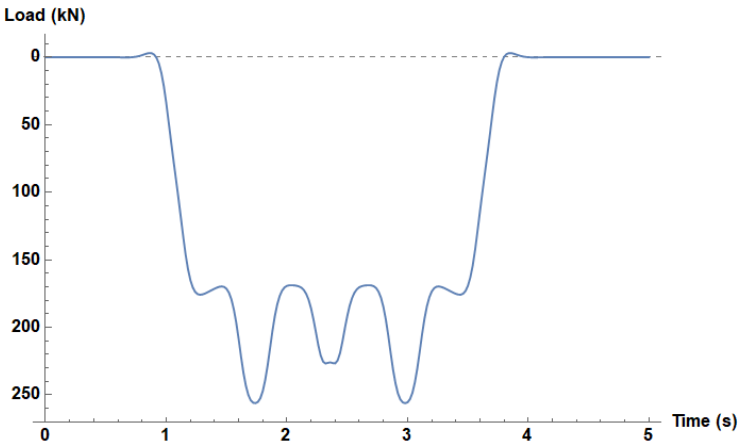

Figure 4.7: Total load on a 10-meter concrete slab as a function of time. The first axle contacts the slab at $t = 1$.

From Figure 4.7, it can be deduced that the maximum load that will be applied to a concrete slab will therefore be 253.77 kN. If this value is inserted in Equations 3.4, 3.5 and 3.6 it is possible to assess the evolution of the surface displacements in the building location as the train moves away from it.

After analysing the distances between the future tram route and the nearby buildings on the section crossing the DTU campus, a distance of 6 metres is considered. This value represents

the minimum track-to-building distance and, therefore, the most unfavourable distance in terms of vibration transmission to buildings.

Figures 4.8, 4.9 and 4.10 show both horizontal, u_x and u_y, and the vertical, u_z, surface displacements at a point 6 metres away from the track. Those displacements are caused by the maximum load transmitted by a slab as the train moves away from the receiver keeping a constant track-building distance of 6 meters in the x-axis. The coordinate system under consideration is represented in Figure 3.5.

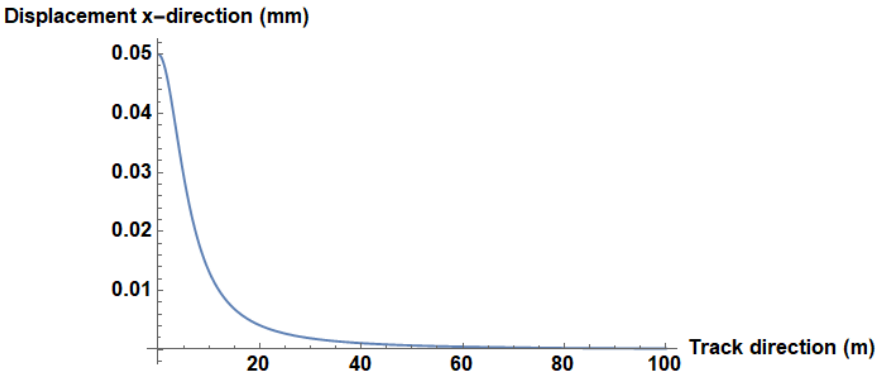

Figure 4.8: Surface displacement in the x-direction at a point 6 metres away from the track as the train moves away from it.

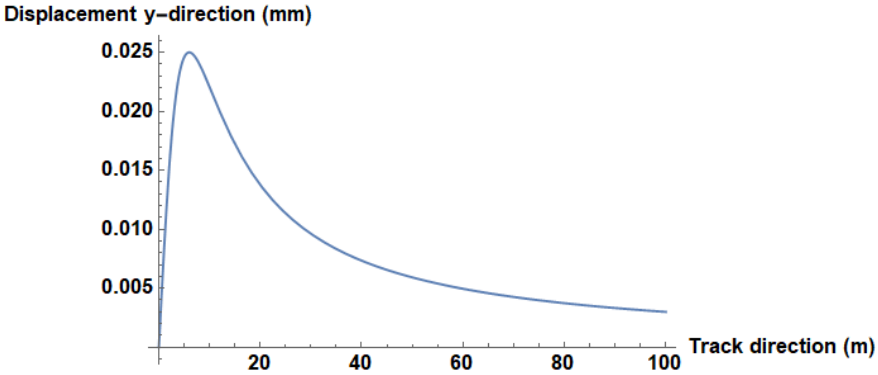

Figure 4.9: Surface displacement in the y-direction at a point 6 metres away from the track as the train moves away from it.

From the previous results it is observed that after 40 meters the displacement variation in the building location has already stabilized. Therefore, a total influence section of 80 meters is considered, 40 meters where the MU approaches and another 40 meters where it moves away. In other words, 8 concrete slabs of 10 m length will transmit loads to the ground that will influence the displacements reaching the foundation of the building. These loads are transmitted to the ground in a uniformly distributed manner under the area of each slab by assuming that the

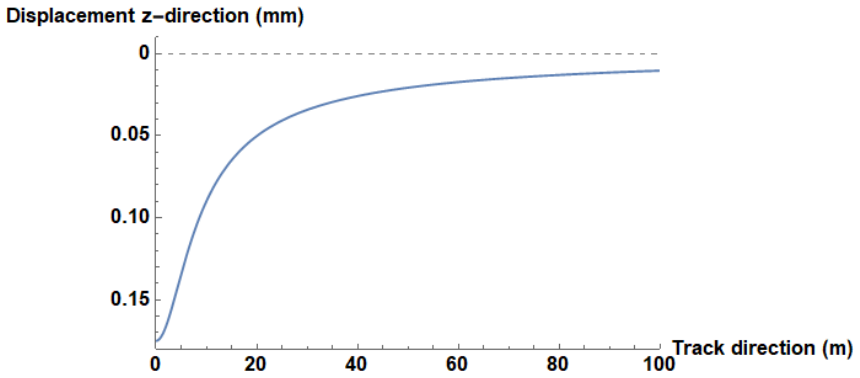

Figure 4.10: Vertical surface displacement in the z-direction at a point 6 metres away from the track as the train moves away from it.

concrete is infinitely rigid.

The total movements in each direction under the receiver building over time are shown in Figures 4.11, 4.12 and 4.13. As explained in Subsection 3.2.1, this is achieved by inserting the time-dependent loads transmitted by each slab (Figure 4.7) into Equations 3.4, 3.5 and 3.6, considering the position of each slab in the defined coordinate system.

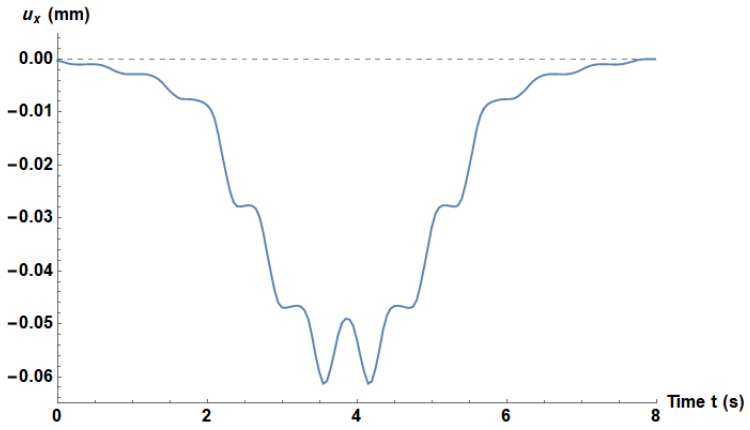

Figure 4.11: Total horizontal surface displacement in the x-direction at a point 6 metres away from the track over time.

To analyze the response of a building to the displacements calculated above, it has been chosen to implement a 3 degrees of freedom linear system since 3-story buildings are predominant in the study section. The model for analyzing the vibrations in the building structure due to vertical displacements is shown in Figure 3.6.

Table 4.4 gathers all the inputs necessary to solve the EOM associated with the system (Equation 3.14). Those data have been estimated based on typical values for buildings similar

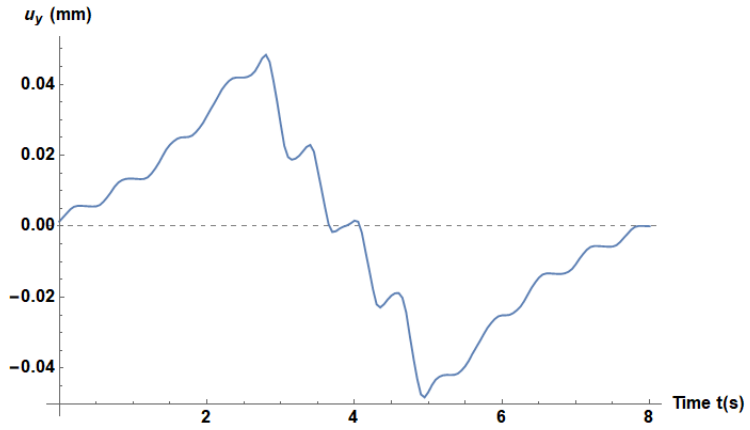

Figure 4.12: Total horizontal surface displacement in the y-direction at a point 6 metres away from the track over time.

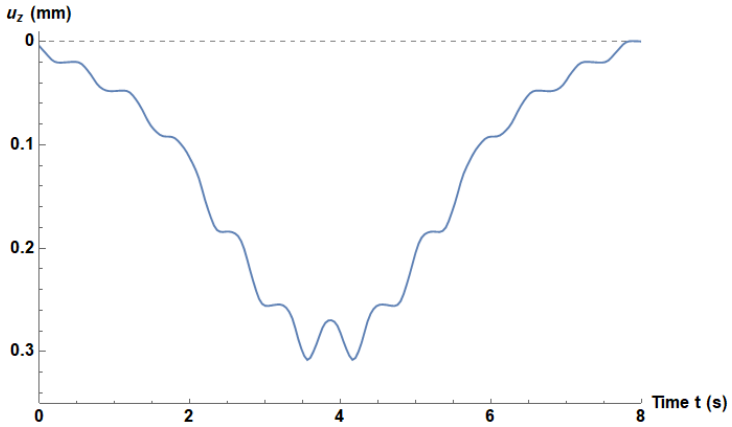

Figure 4.13: Total vertical surface displacement in the z-direction at a point 6 metres away from the track over time.

to those analyzed in the DTU section. It should be mentioned that many of the structural characteristics vary from building to building. Therefore, the geometric and structural inputs presented in Table 4.4 must be adapted for each study structure.

For the model shown in Figure 3.6 and with the characteristics listed in Table 4.4, the natural frequencies, calculated with Equation 3.16, are: 0.69 Hz (1st floor), 1.27 Hz (2nd floor), and 1.66 Hz (roof). As the vertical displacements (on the z-direction) are the most predominant of the three directions, these are the ones used to observe the building response. Figure 4.14 shows the vertical displacements for each one of the storeys after solving Equation 3.13 for x.

For the purpose of analyzing what would happen with shorter concrete slabs, 3-meter slabs are now considered. As is logical, a larger number of slabs will now transmit loads to the ground

Characteristics of a standard building	
Column's length (l)	3 m
Column's cross-sectional area (bh)	0.3x0.3 m2
Young's modulus of the column's material (E)	4e10 Pa
Resulting polar moment of inertia of the column's cross-sectional area (I)	6.75e-4 m4
Resulting spring stiffness of one column (k)	3e6 N/m
Estimated dead load per area unit of one building slab	1000 kg/m2
Estimated slab area	25x15 m2
Total dead load of one building slab (m)	375 t

Table 4.4: Characteristics of a standard building

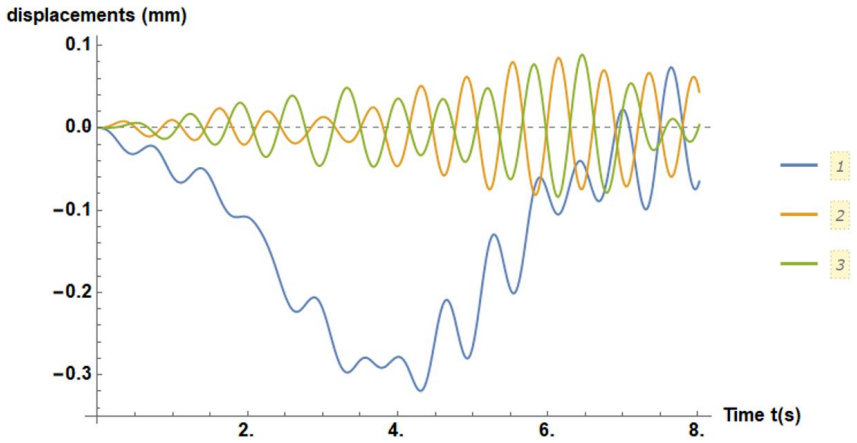

Figure 4.14: Vertical displacement for each one of the three storeys of the building.

that will influence the displacements reaching the building foundations. Figure 4.15 show the vertical displacements over time in the soil surface of the building location. In turn, the vertical displacements for each one of the building storeys considering 3-meter slabs on the track can be visualized in Figure 4.16.

4.1.3 Conclusions

After implementing the developed methodology for quasi-static analysis in the case study, some interesting points are highlighted.

Under the assumptions and simplifications under consideration, longer concrete slabs transmit more loads to the ground due to the vehicle's weight. Consequently, the displacements in the ground will be more significant. When the slabs are shorter, the weight is better distributed,

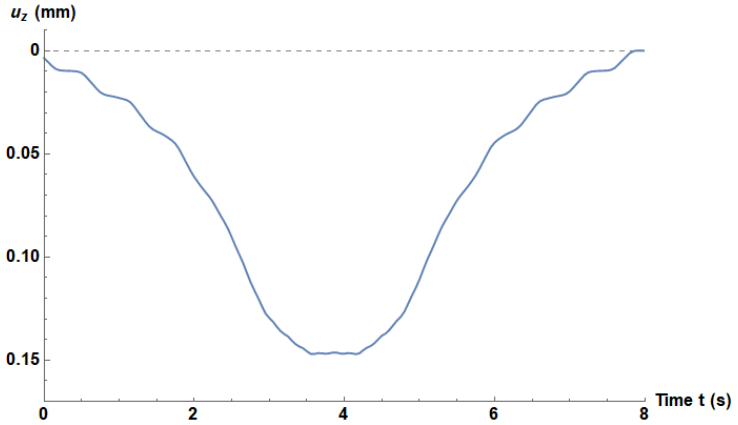

Figure 4.15: Vertical soil surface displacements at a point 6 metres away from the track over time for 3-meter long slabs.

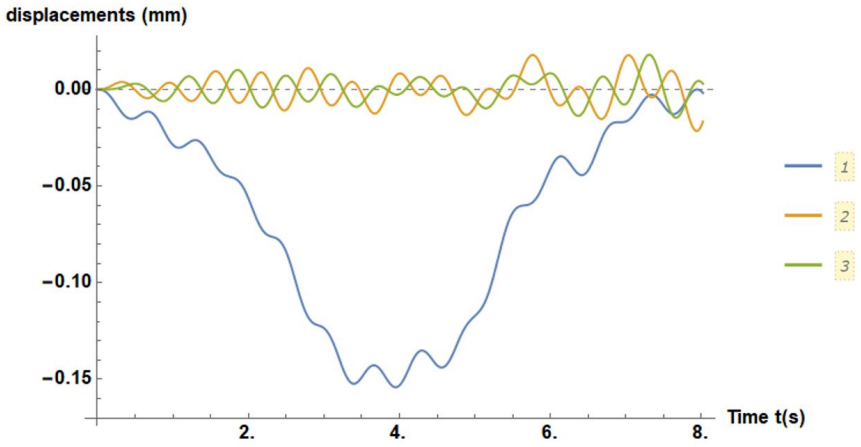

Figure 4.16: Vertical displacement for each one of the three storeys of the building for 3-meter long slabs.

and the total displacements are smaller in magnitude and evolve more uniformly.

Predictably, the predominant displacements on the ground are vertical, about five times greater than those transverse to the track. Nevertheless, the displacements at the site of the building under study are of the order of tenths of a millimeter, and the effect on the second and third floors is practically nil.

Something that was already known, and has been corroborated thanks to the model used, is that the natural frequencies in the different building floors are low. Therefore, rather than the magnitude of the displacements or accelerations, the focus should be on modal analysis to identify possible resonance cases. In any case, the study of resonances due to the moving load

effect of the track is particularly relevant for railway bridges, where the interaction between vehicle and infrastructure is very direct. In the case of buildings, the ground should dampen the amplitudes of the problematic frequencies during the propagation path.

Finally, the damping mat does not seem to have any advantage in mitigating consequences due to the moving load effect. This is not surprising either since it is not the purpose of such an element. In fact, the presence of the mat increases the track resilience, so larger displacements of the slab it supports are expected. The possible amplification of low frequencies as a result of the installation of the mat could also be analyzed.

4.2 Dynamic analysis

This section presents the results obtained after applying the dynamic analysis methodology developed in Section 3.2.2 to the case study.

4.2.1 Inputs

The rolling stock, track, and soil related inputs required to perform the dynamic excitation analysis are shown in Tables 4.5, 4.6, and 4.7. As the case study remains the same, the input data do not vary from those of the quasi-static assessment. However, it is necessary to consider additional inputs not employed in the previous analysis, which are added to those listed in Subsection 4.1.1.

Rolling stock inputs	
Max. axle load	8.8 t
Vehicle length	35 000 mm
Operation speed	50 km/h
Time interval between trains	5 min
Axle distance in a bogie	1800 mm
Central cars bogie-bogie distance	8930 mm
Central car-end car bogie-bogie distance	8350 mm
New wheel diameter	600 mm
Worn wheel diameter	520 mm

Table 4.5: Vehicle technical data for the dynamic analysis [62] [63].

The inputs for the damping mat (spring coefficient and viscous damping coefficient) have been assumed based on the characteristics of the SBR rubber, which is the main material in

Track inputs	
Rail Young's modulus (E_r)	$2.06 \cdot 10^{11}$ Pa
Rail moment of inertia about the neutral axis (I_x)	$3.21 \cdot 10^{5}$ m4
Rail weight per meter length (ρA)	58.2 kg/m
Modulus of Elasticity of the continuous rubber profile enclosing the rail (k)	$4.1 \cdot 10^{7}$ Pa
Concrete slab dimensions (length x width x thickness)	10x2.5x0.2 m
Density of concrete (ρ_c)	2500 kg/m^3
Spring stiffness of the damping mat (k_{mat})	$9 \cdot 10^{5}$ N/m
Viscous damping coefficient of the damping mat (c_{mat})	10 000 Ns/m

Table 4.6: Track inputs for the dynamic analysis [66].

anti-vibration mats of different manufacturers [67] [68] [69].

Soil inputs	
Modulus of elasticity (k_{soil})	$7 \cdot 10^{7}$ Pa
Poisson's coefficient (ν)	0.3
Density (ρ_{soil})	1600 kg/m

Table 4.7: Soil elastic properties for the dynamic analysis [64] [65].

4.2.2 Calculations

The first step is to analyze the rail response to a unit impulse (1 Ns), which is the output of Equation 3.17. Figure 4.17 represents the displacement at the rail coordinate $x = 0$ over time for a unit impulsive load. Further on, the impulse for the different defect typologies causing impacts at the wheel-rail interface will be quantified to obtain total results.

It is chosen to study the impact of a rail squat defect, modeled as shown in Figure 3.9b. For a defect length of $w = 60$ mm, the resultant rail impulse calculated with Equation 3.22 is around 37 Ns. A value of $w = 60$ mm is chosen, since it is in the range of typical values for severe squats [70]. Figure 4.18 shows the total displacements on the rail due to a squat defect after multiplying the impulse value obtained to the unit results in Figure 4.18.

In parallel to the analysis in the time domain, it is also possible to analyze the evolution of the response along the rail for a given time instant. Figure 4.19 shows how deformations

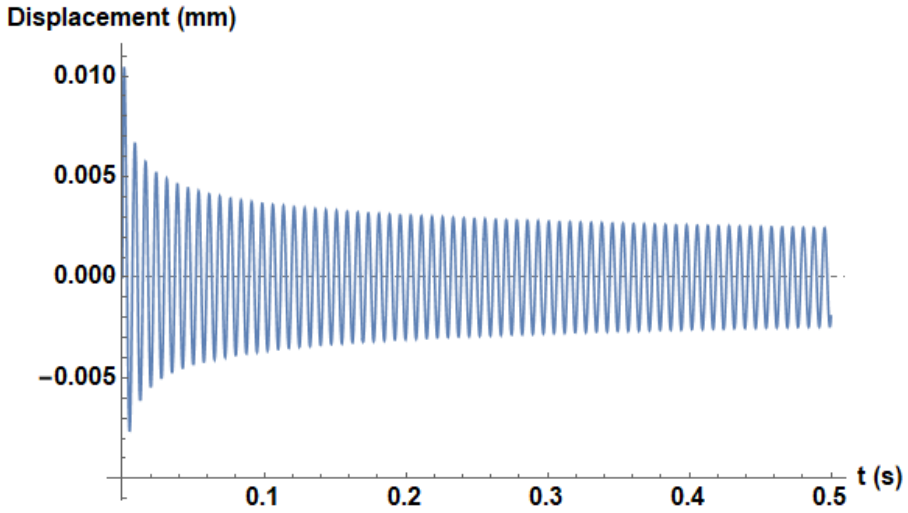

Figure 4.17: Displacement at $x = 0$ for a unit impulsive load.

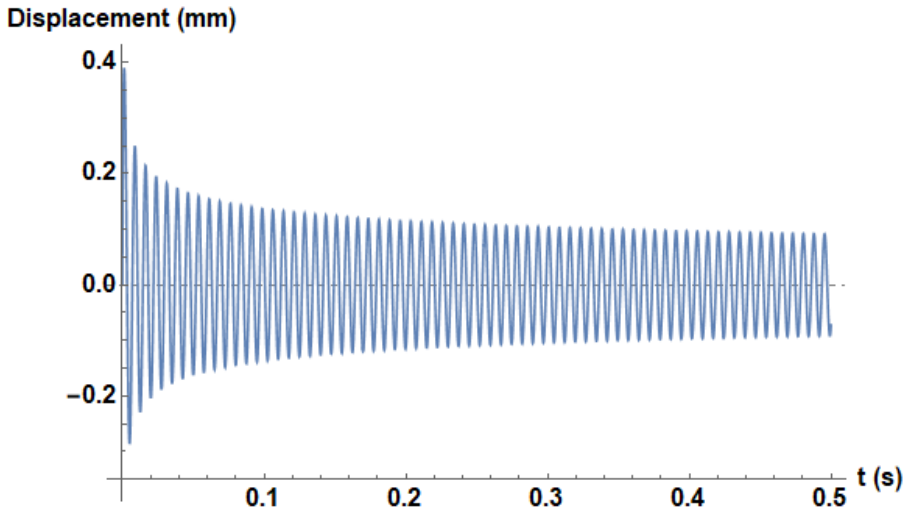

Figure 4.18: Displacement at $x = 0$ for an impulsive load caused by the wheel when going through a 60 mm long squat.

propagate along the rail for two specific time instants.

The representation of the displacements in the rail at different time instants is interesting because it clearly shows how the waves generated by an impact due to a defect in the wheel or the rail propagate. Figure 4.19 shows a change of position for the same wave peak at two time instants. By studying these peak position differences with time, it is easy to find the propagation velocity of the wave. This turns out to be constant and of value 759 m/s for the inputs being used in this case study.

Figure 4.20 shows the results for the chosen rail defect when including the 8 impacts

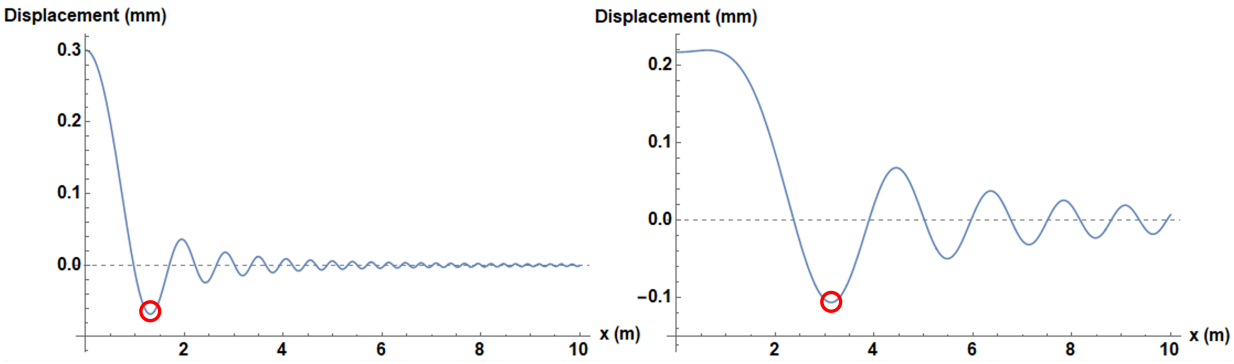

(a) (b)

Figure 4.19: Displacements along the rail for time instants (a) $t = 0.5$ ms and (b) $t = 2.5$ ms due to a unit impulsive load. The red circles indicate the same wave peak at the two instants.

corresponding to each of the vehicle wheels passing over the squat. As was done in Figure 4.18 for a single impact, the displacements at the defect position ($x = 0$) in the time domain are studied.

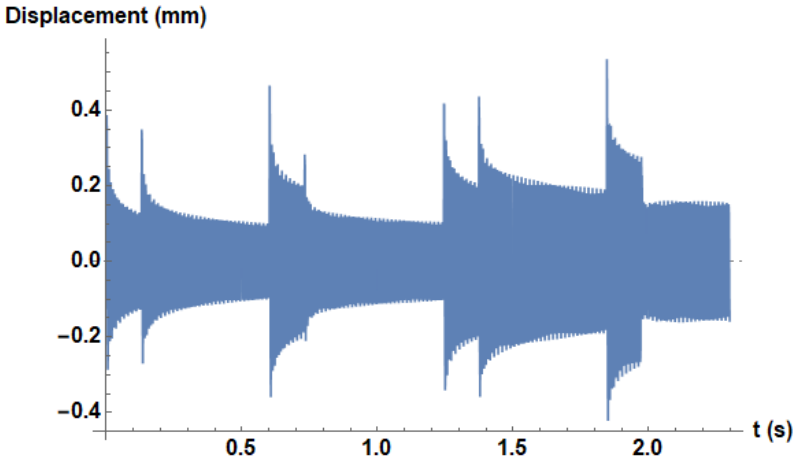

Figure 4.20: Displacements at the defect position ($x = 0$) over time for eight impulsive loads due to the considered squat defect.

For comparative purposes, it is interesting to analyze what the response of the rail would be if the type of defect were a wheel flat with an impulse equal to that calculated for the squat. The displacements as a function of time at $x = 0$ for nine impacts of the wheel flat on the rail are plotted in Figure 4.21. The position and instant at which the first impact occurs are $x = 0$ and $t = 0$.

Like in the quasi-static analysis, the analysis converges and focuses on analyzing the behavior of one 10-meter-long concrete slab connected by joints to other slabs. The evolution over time of the load transmitted to the concrete slab under a single impact of the wheel on the rail squat ($F_{o,1}(t)$) is presented in Figure 4.22. It is assumed that the rail defect is at the center of the rail

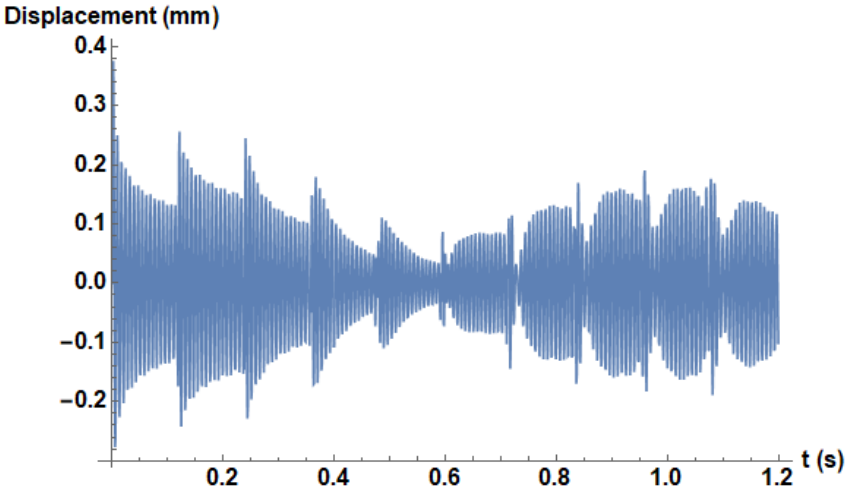

Figure 4.21: Displacements over time at $x = 0$ for nine impulsive loads due to a wheel flat.

span in the slab, as shown in Figure 3.14a.

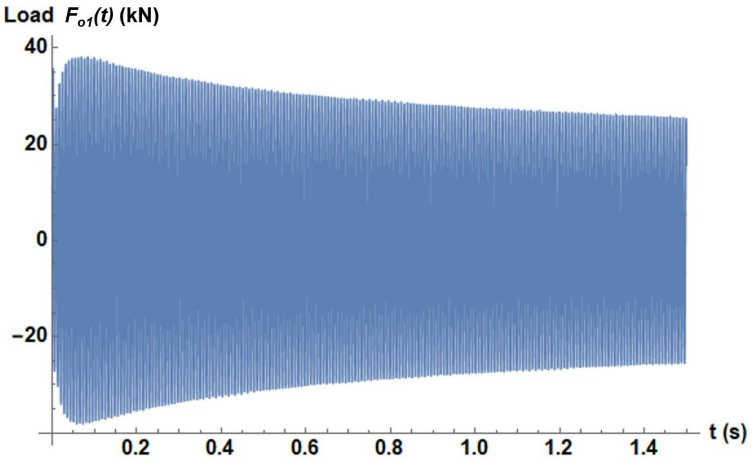

Figure 4.22: Load $F_{o1}(t)$ on a concrete slab over time for one impulsive load due to a squat rail defect located in the slab mid-point.

Because of the high computational cost when integrating Equation 3.17 with respect to x, it has been necessary to discretize the problem in sub-blocks of $\Delta x = 1$ m and in time periods of $\Delta t = 1$ ms, and to integrate numerically. In addition, only one half of the section length has been considered and the result has been multiplied by two given the symmetry of the problem.

By superimposing the results for one impulsive load (Figure 4.22), the loads transmitted to the slab over time for eight impulses, $F_{o,8}(t)$, can be derived. This is shown in Figure 4.23 and represents the slab loading due to the passage of the eight tramway wheels over the squat defect on the rail.

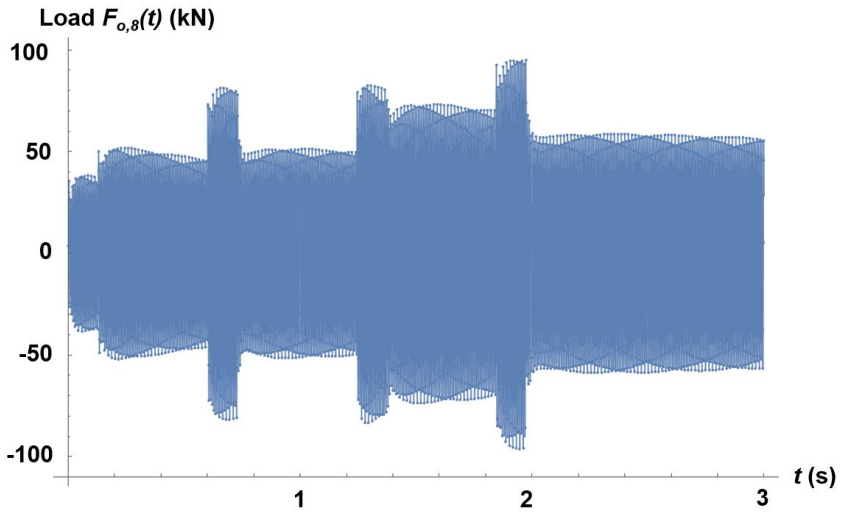

Figure 4.23: Load $F_{o,8}(t)$ on a concrete slab over time for eight impulsive loads due to a squat rail defect located in the slab mid-point.

Once the load distribution in the concrete slab is known, the mass-spring-damper model shown in Figure 3.16 is applied to determine the load transmission to the mat-ground system. The mass of one slab is 12 500 kg, according to its dimensions and the density of concrete, ρ_c.

By solving Equations 3.9 and 3.10 with the values of E, ν, and the dimensions of the concrete slab stated in Subsection 4.1.1, a soil spring stiffness equal to $k_{soil} = 4.90 \cdot 10^8$ N/m is obtained. As this spring stiffness is much larger than the one assumed of the damping mat, the latter one is the only stiffness that has an influence on the model results, while the soil behaves as a stiff element on which the mat rests.

The vertical displacements over time, $x_{m1}(t)$, undergone by the slab when subjected to a force $F_{o,8}(t)$, are obtained by solving for x in Equation 3.23. The slab is modeled as a mass supported on the anti-vibration mat, modeled as a spring. Figure 4.24 represents the displacements $x_{m1}(t)$ over time for eight impulsive loads, i.e., when the slab is subjected to $F_{o,8}(t)$. $t = 0$ is the instant at which the first impact occurs.

After calculating the displacements $x_{m1}(t)$ in the slab and together with the viscoelastic properties of the damping mat, one proceeds to calculate the loads transmitted to the soil surface, $F(t)$, by applying Equation 3.23. Figure 4.25 plots $F(t)$ and the contribution of the elastic part of the mat, i.e., the term $k_{eq}x(t)$ in Equation 3.23, and the viscous contribution, $c_{eq}x'(t)$ in Equation 3.23.

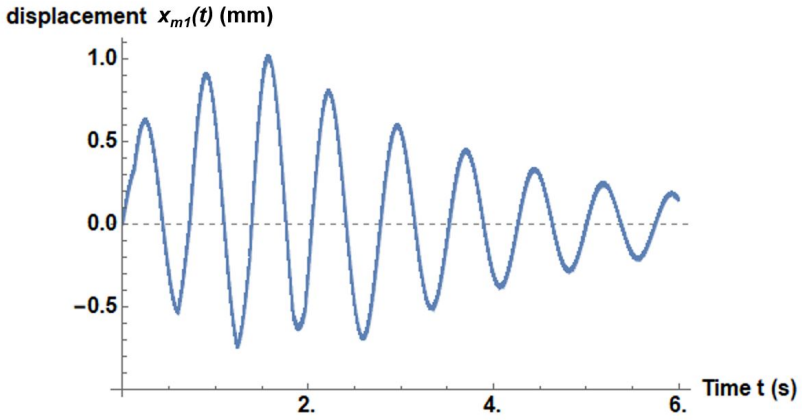

Figure 4.24: Vertical displacements over time, $x_{m1}(t)$, on a concrete slab subjected to $F_{o,8}(t)$ and supported on an anti-vibration mat.

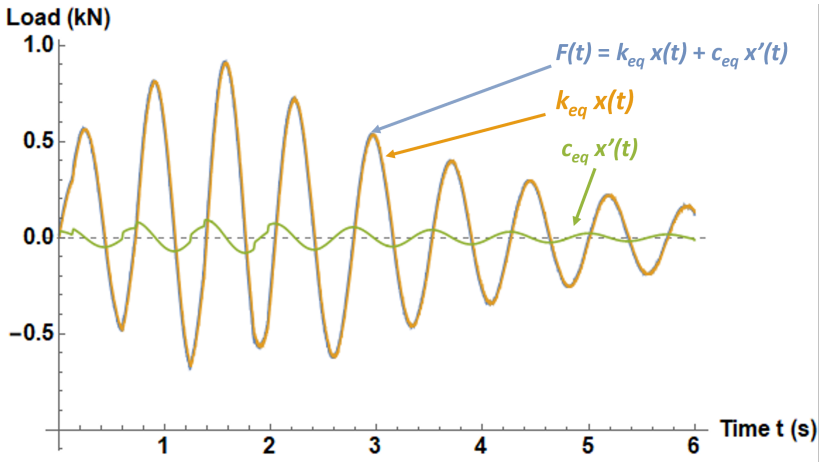

Figure 4.25: Load transmitted to the soil, $F(t)$, and both elastic and viscous contribution of the mat to the force transmission from the concrete slab displacements.

To check the impact of the damping mat on load transmission to the ground, Figure 4.26 represents the force $F(t)$ for the case where there is no mat between the slab and the ground surface.

The determination of the main frequencies of the force $F(t)$ transmitted to the ground is performed by means of the Discrete Fourier Transform (DFT). The DFT, based on the continuous Fourier transform (Equation 3.27), requires a discrete input sequence obtained from sampling a continuous function. Figure 4.27 shows the DFTs for $F(t)$ in the cases with mat and without damping mat (Figures 4.25 and 4.26) for a sampling frequency of 1000 Hz. The main frequencies of $F(t)$ are 19 Hz and 133 Hz when no damping mat is installed, and 1.3 Hz in the track with mats.

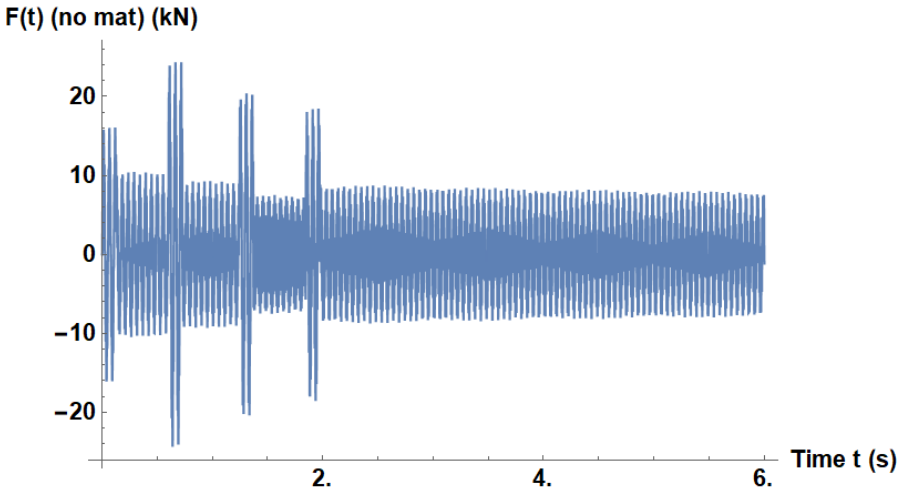

Figure 4.26: Load transmitted to the soil, $F(t)$, for the case without damping mat.

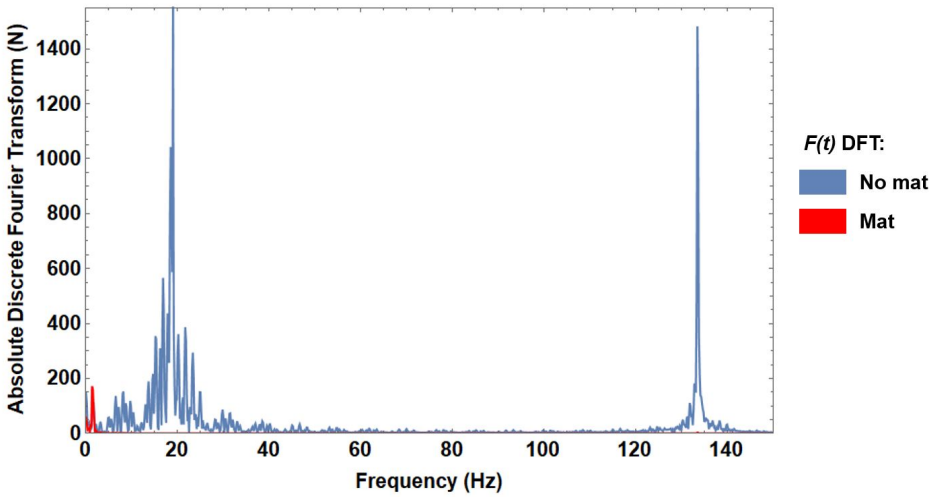

Figure 4.27: DFT of $F(t)$ with and without damping mat.

From the transfer functions presented in Equations 3.28 and 3.29, the Rayleigh wave displacements at any point on the ground surface due to the force $F(t)$ can be obtained. Figure 4.28 shows how the transfer functions, H_u and H_w, evolve as a function of frequency for the soil data of the case study (Table 4.7). The distance between the track and the study building is assumed to be 6 meters, as applied during the quasi-static analysis. Therefore, the results in Figure 4.28 are particularized for $r = 6$ m.

The Fourier analysis for the horizontal, $u(t)$, and vertical, $w(t)$, displacements on the ground surface where the study building is located are shown in Figures 4.29 and 4.30. These are obtained by multiplying the transfer functions in Figure 4.28 to the frequency domain results of $F(t)$ (Figure 4.27).

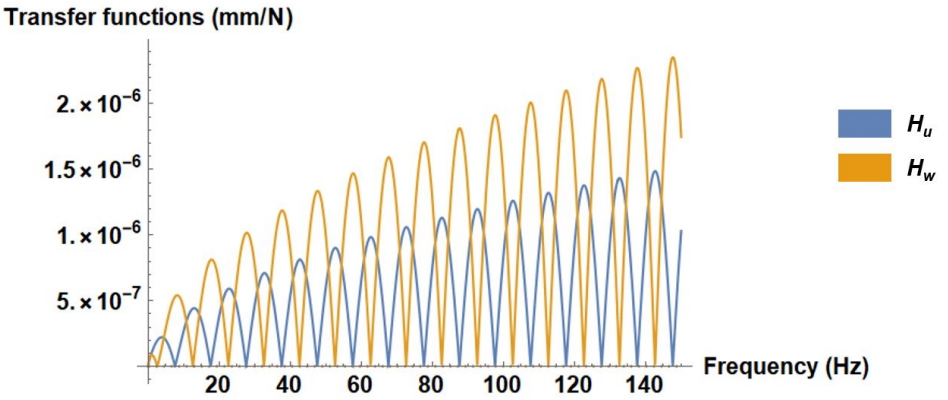

Figure 4.28: Transfer functions H_u and H_w for a radius $r = 6$ m.

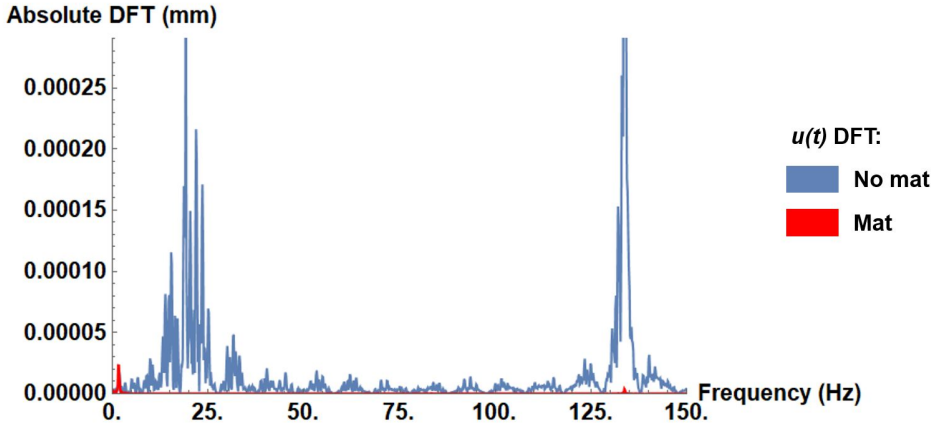

Figure 4.29: DFT of $u(t)$ with and without damping mat.

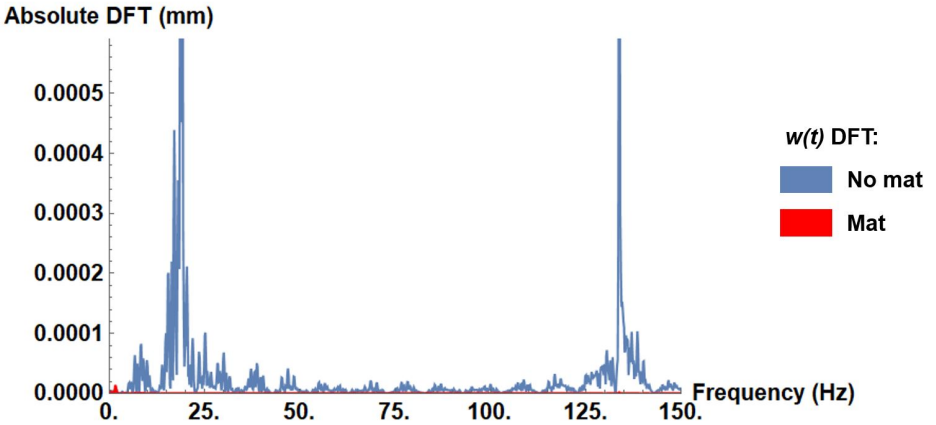

Figure 4.30: DFT of $w(t)$ with and without damping mat.

The main frequencies in both the cases with and without damping mat remain practically the same as in the results for $F(t)$ (Figure 4.27). For the case with mat the main frequency goes from 1.3 Hz to 1.5 Hz.

Finally, Figure 4.31 analyzes the exponential decay of amplitudes corresponding to the displacements u and w, given by the transfer functions H_u and H_w, with distance r. The results shown correspond to the frequency $f = 1.3$ Hz, which is the predominant frequency for the signal $F(t)$ when anti-vibration mats are installed (Figure 4.27).

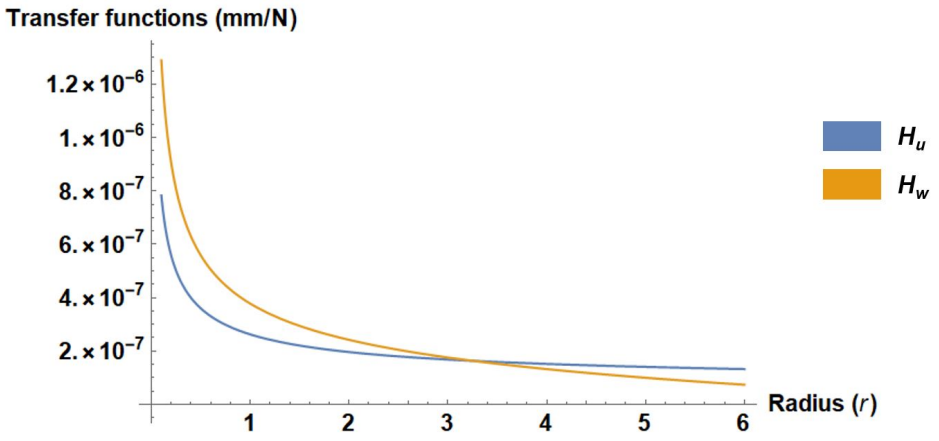

Figure 4.31: Transfer functions H_u and H_w over radius, r, for the frequency $f = 1.3$ Hz.

Once the results for the case study have been presented, the behavior of the mats and their effect on vibration transmission are analyzed by means of a parametric analysis. First, three anti-vibration mats with different values of viscous damping coefficient are compared: $c = 0$ Ns/m, $c = 10\,000$ Ns/m (already studied in the case study), and $c = 30\,000$ Ns/m. Figure 4.32 represents the transmission of force $F(t)$ to the ground for each mat. Figure 4.33 plots these results in the frequency domain using the discrete Fourier transform.

To see the effect of anti-vibration mats with different spring stiffnesses, two damping mats are now compared: one with $k = 9 \cdot 10^5$ N/m (already analyzed in the case study) and a more resilient one with $k = 3 \cdot 10^5$ N/m. Figures 4.34 and 4.35 show the results obtained for $F(t)$ in the time domain and frequency domain, respectively.

4.2.3 Conclusions

The study and analysis of the dynamic interactions between wheel and rail have made it possible to address one of the main objectives of this work: to assess the effectiveness of damping mats as a vibration mitigation measure.

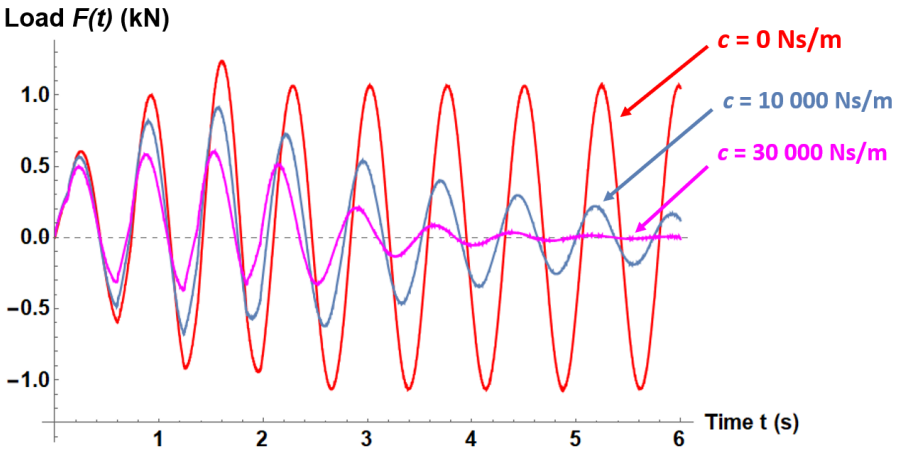

Figure 4.32: Force $F(t)$ transmitted to the ground for different values of the viscous damping coefficient, c, of the damping mat.

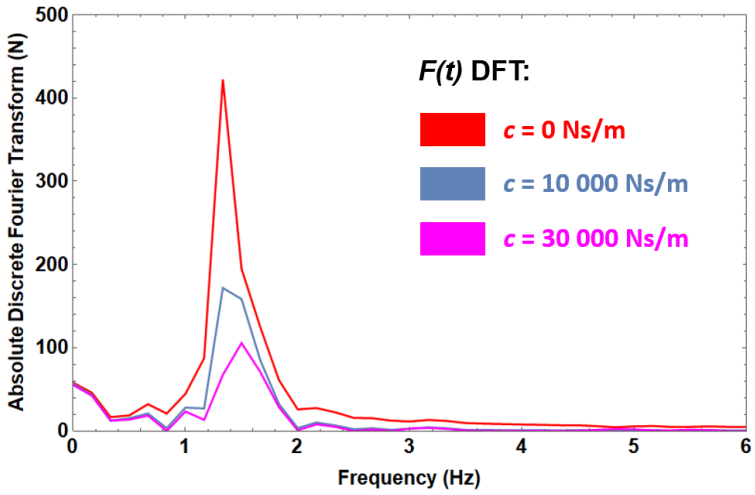

Figure 4.33: DFT of $F(t)$ for different values of the viscous damping coefficient, c, of the damping mat.

Comparing results in the frequency domain for cases with and without the mat reflects several aspects of its performance. First, the high efficiency of the damping mat, modeled as an elastic and viscous element, in damping the amplitudes of the 19 and 133 Hz frequency peaks. Second is the amplification of lower frequencies, such as 1.3 Hz in the case study.

According to the ground transfer functions considered, the soil does not significantly impact the frequency domain response. However, it slightly modifies the frequency peaks by damping different frequencies unevenly. Therefore, although the vibration problem is largely

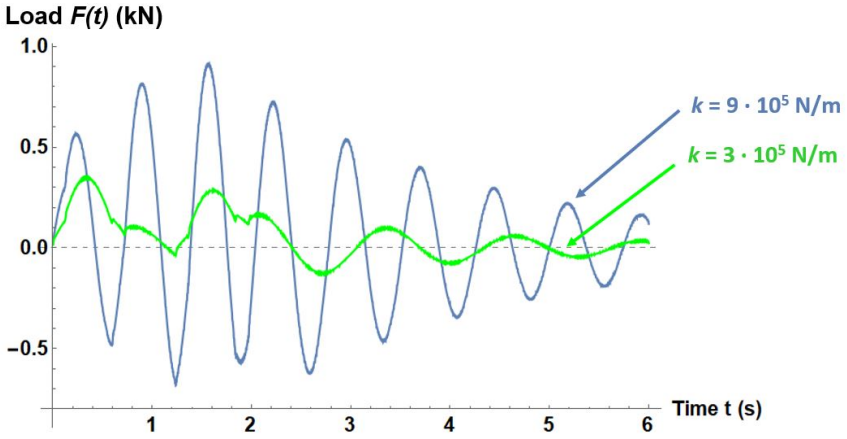

Figure 4.34: Force $F(t)$ transmitted to the ground for different values of the spring stiffness, k, of the damping mat.

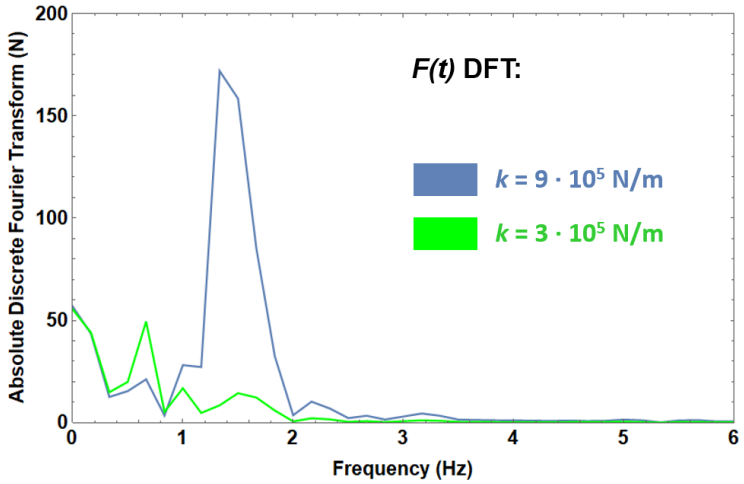

Figure 4.35: DFT of $F(t)$ for different values of the spring stiffness, k, of the damping mat.

solved, it is necessary to study the amplification of frequencies in the 0 to 5 Hz range. These low-frequency values could coincide with the natural frequencies of the building structure, generating a resonance phenomenon. In addition, the ground characterization is also essential, since the soil can change the frequency peaks during the wave propagation on the ground surface.

Taking into account the above aspects, the elastic and viscous characteristics of the mats to be installed must be adapted in such a way as to avoid the propagation of problematic low frequencies. Precisely the parametric analysis carried out at the end of the analysis has studied how the behavior of the damping mats changes when their properties are modified. The spring stiffness controls the frequency of the waves transmitted to the ground—the more flexibility,

the lower the frequencies of the outgoing waves. On the other hand, the damping coefficient controls the wave amplitude—the greater the damping, the greater the attenuation of the wave in a given period. In conclusion, an anti-vibration mat can be considered a filter that works by two mechanisms that must be regulated according to the needs and characteristics of each case.

4.3 Validation of results

This section focuses on studying the consistency of the results obtained during the application of the dynamic analysis methodology for the case study (Section 4.2). A full validation would require, in addition, to verify that the developed methodology presents comparable results to those that can be obtained by measurements at the study site. Therefore, in Section 5.3, a field instrumentation plan is proposed with which, as part of future work, measurements can be obtained to validate the analytical results.

Most of the results in Section 4.2 are based on the analytical solution for an infinite Euler-Bernoulli beam subjected to impulsive loading [55]. To verify that such a solution provides physically meaningful results, a sensitivity analysis of Equation 3.17 is performed. Table 4.8 indicates how the frequency of the waves generated by the impulsive load is affected by the different parameters in Equation 3.17.

For an increase in...	**Frequency**
Rail weight per meter length (ρA)	Decreases
Rail Young's modulus (E_r)	No effect
Rail moment of inertia about the neutral axis (I_x)	No effect
Modulus of Elasticity of the continuous support (k)	Increases
Viscous damping coefficient of the continuous support (c)	Decreases

Table 4.8: Sensitivity analysis of Equation 3.17

Let us compare the results of Table 4.8 with Equation 4.1, the analytical expression that gives the natural frequency in a damped system with 1 DOF.

$$\omega_d = \omega_n \sqrt{1 - \zeta} \tag{4.1}$$

Where ω_n is the natural frequency, obtained with Equation 2.3; ω_d is the damped natural frequency, and ζ represents the damping ratio, directly related with the viscous damping coefficient, c.

In view of Equations 4.1 and 2.3, it is verified that the relationships indicated in Table 4.8 have physical meaning. Therefore, Equation 3.17 provides consistent results, at least in terms of relationships between the frequency of the computed response and the equation parameters.

To check if the results obtained in the case study are in orders of magnitude, they are compared with outputs in projects of similar characteristics based on field measurements or numerical models. Figure 4.36 shows examples of impulse responses in a cantilever beam [71], and in a discretely supported rail [72], with which to compare the estimated response in the case study (Figure 4.17).

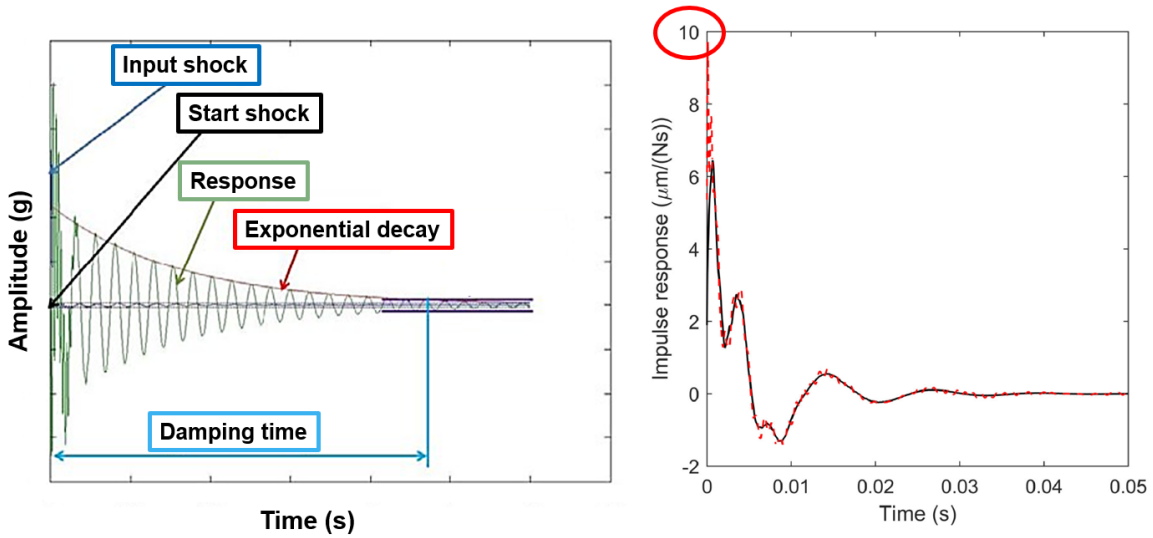

(a) (b)

Figure 4.36: Examples of impulse excitation responses: (a) Free vibration response of a cantilever beam due to impulse excitation [71]. (b) Moving Green's functions for a rail subjected to an excitation above a sleeper (black) and at the middle of the sleeper bay (red) [72]. Train speed 100 km/h.

Figure 4.36a shows the typical shape of the response of a medium to an impulse, similar to the one presented in Figure 4.17. An initial peak that decays exponentially with time until it stabilizes after the damping time. Figure 4.36b shows the response for a rail on a sleeper track, which is a different track typology than the one addressed in this work. However, it is interesting to see that the impulse response peak is about 0.01 mm, a value similar to the peak in Figure 4.17. This seems to indicate that, at least, the first results in the dynamic analysis of the case study are in orders of magnitude.

Figure 4.37 presents relations between the vehicle speed and the maximum wheel-rail dynamic impact force induced by wheel flats of different sizes. These results are based on a

full-scale high-speed wheel-rail interface test rig conducted in China [73].

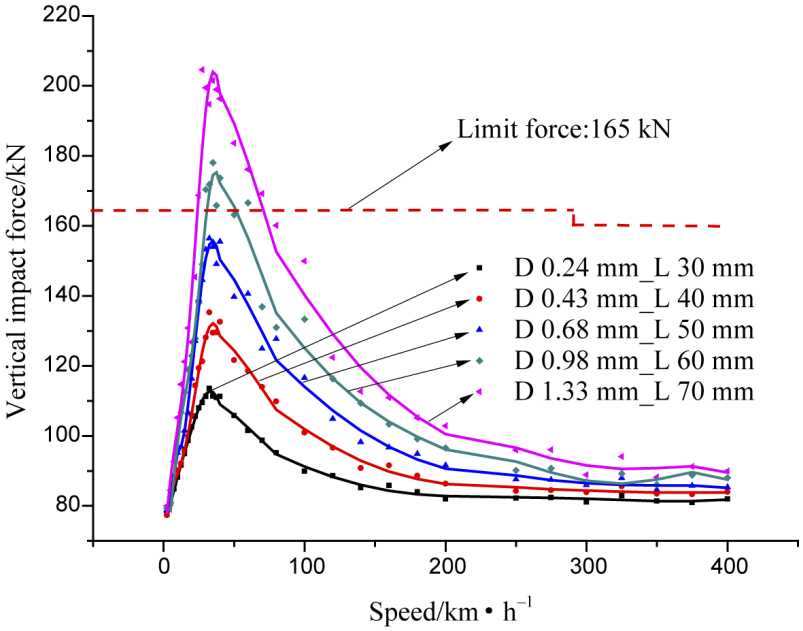

Figure 4.37: Relations between vehicle speed and maximum wheel-rail dynamic impact forces induced by wheel flats of different sizes [73].

In general, the force values represented in Figure 4.37 are considerably higher than those determined in the case study. This may be due to the track type of the test site being much stiffer, although the characteristics are not specified in the article. In any case, the results appear to be in order magnitude, pending more precise validation.

Finally, Figure 4.38 [74] illustrates the spectrogram for two types of wheel-rail excitations with different spectral characteristics. The track characteristics are similar to those in the case study, as well as the numerical track model. However, a rail with discrete elastic supports is used, not applicable to the case of the Embedded Rail System considered in this work.

The main frequencies are primarily in the range of 0 to 100 Hz, with magnitudes similar to those obtained in Figure 4.27. Although the typology of the excitations is unknown and the track typology is different, these results could indicate that the outputs of the Fourier analysis in Subsection 4.2.2 are coherent with the studied problem. Coherent both for the peak frequencies found and for their quantification.

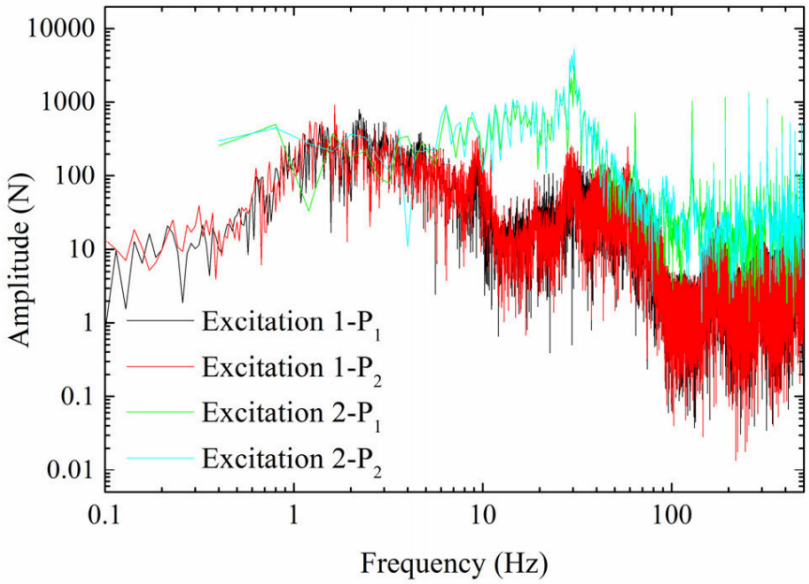

Figure 4.38: Spectrogram of different wheel-rail excitations [74].

Chapter 5

Conclusion

5.1 Summary

The work has been focused on meeting the objectives specified in Section 3.3. The first one was the development of a methodology capable of predicting the vibration characteristics induced by urban rail traffic on Embedded Rail System tracks. The second objective came from applying the first one and evaluating the role of damping mats as an anti-vibration measure.

In order to carry out the above, it was necessary to perform a thorough literature review structured in different sections dealing broadly with the field of ground vibrations due to urban rail traffic. A case study based on the Ring 3 light rail project was subsequently carried out to put into practice the previously introduced methods and to draw conclusions based on the results.

The detailed thesis structure can be found in Section 1.2.

5.2 Findings and discussion

In addition to the specific conclusions of Subsections 4.1.3 and 4.2.3, other more general insights gained from the literature review and the work conducted are discussed in this section.

For an elastically supported rail, quantifying and characterizing the impulsive load from a wheel-rail impact is practically independent of the vehicle characteristics. The track, the defect at the wheel-rail interface, and the vehicle speed are the factors to be considered. The reason is the higher resistance of the wheel with respect to the elastic rail to resist movement during an impact for the frequencies under study. Consequently, the vehicle's weight does not influence the momentum produced, however counter-intuitive this may seem.

Another notable finding has been to explore the possibilities of the solution presented by Yu and Yuan to calculate the response of an Euler-Bernoulli beam subjected to an impulsive load (Equation 3.17). This solution constitutes a powerful tool for studying dynamic excitations due to wheel-rail impacts, but it is also applicable to non-destructive tests on pavements or blasting. Since the equation is a function of space and time, various application possibilities exist. For example, the rail response after an impact has been studied as a function of space for different instants. Said evolution with time allows to indirectly obtain the propagation speed of the wave in the rail.

Generally speaking, the problem of vibrations induced by urban rail traffic is complex. For this reason, the usual working approach is based on numerical models with data input from field measurements. In contrast, the methodology developed in this work allows for analyzing in a simple and fast way the problem of vibrations induced by urban rail traffic from the coupling of different analytical solutions. For this purpose, assumptions are necessary to simplify the problem along the vibration transmission path.

One advantage of this more analytical approach is that it enables a physical understanding of what happens at each process step, from the source to the receiver. It is also a flexible preliminary prediction tool, as it can be adapted or optimized on a case-by-case basis. Another interesting possibility is to reversely apply the methodology to identify and characterize defects at the wheel-rail interface from vibration data.

5.3 Recommendations for future work

The priority for the near future is to obtain real results from vibration measurements in some of the Ring 3 line sections under construction in order to validate the theoretical results for the presented case study, based on the methodology proposed in this work.

In order to facilitate this next phase of the project, some ideas about the possible field work to be carried out are proposed below. These suggestions are based on the different phases of the analytical methodology employed, and on the results obtained during the case study analyses.

To study the generation and transmission of vibrations and compare the results with those obtained theoretically, it is only necessary to have an impulse hammer and several accelerometers. The hammer measures the impulse after an impact on the rail, which simulates the impact of the wheel on the rail due to a point defect. The accelerometers quantify and characterize the response to the impulse at different levels of the track system.

Field work on the track can only be performed during the construction phase of the infrastructure, because once the track is completed, it is embedded and only the top of the rail is visible.

Figure 5.1 shows a simple diagram showing the signal acquisition process. Piezometric accelerometers are arranged at different track levels to measure the response of rail, slab and soil after an impact from the impulse hammer. Both the sensors and the impact hammer are connected to the data acquisition unit, where the analog signal collected by the sensors is previously filtered and then converted to the digital system. Finally, the numerical values of the digital signal are sent to a computer, where these data can be manipulated.

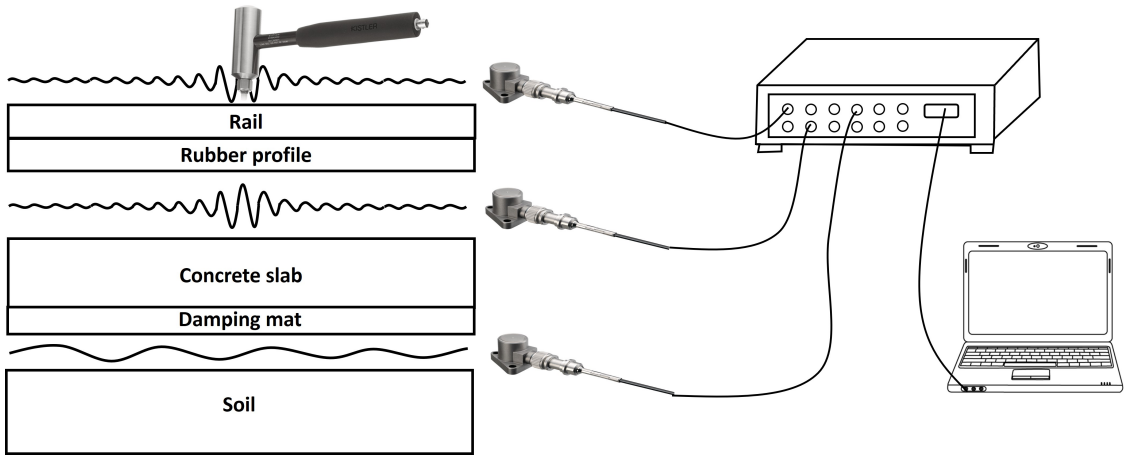

Figure 5.1: Proposed signal acquisition process to analyze the response of the track system to an impulse.

To measure the ground response, several sensors are required along the distance from the vibration source to the receiver. Figure 5.2a represents this distance, r, as well as the location of the n sensors, s_n, and the location of the receiver building, at point N.

There are different approaches to the choice of sensor distribution to correctly characterize the evolution of the soil response as a function of distance from the source. Ideally, a large number of sensors should be placed very close to each other. However, this is unnecessary, impractical and unfeasible.

When ground surface accelerations are expected to evolve linearly or the shape of this evolution is completely unknown, placing the sensors evenly spaced is a reasonable option. However, in order to optimize the use of sensors, a different approach is proposed.

Figure 5.2b shows an approximately exponential evolution of accelerations with distance.

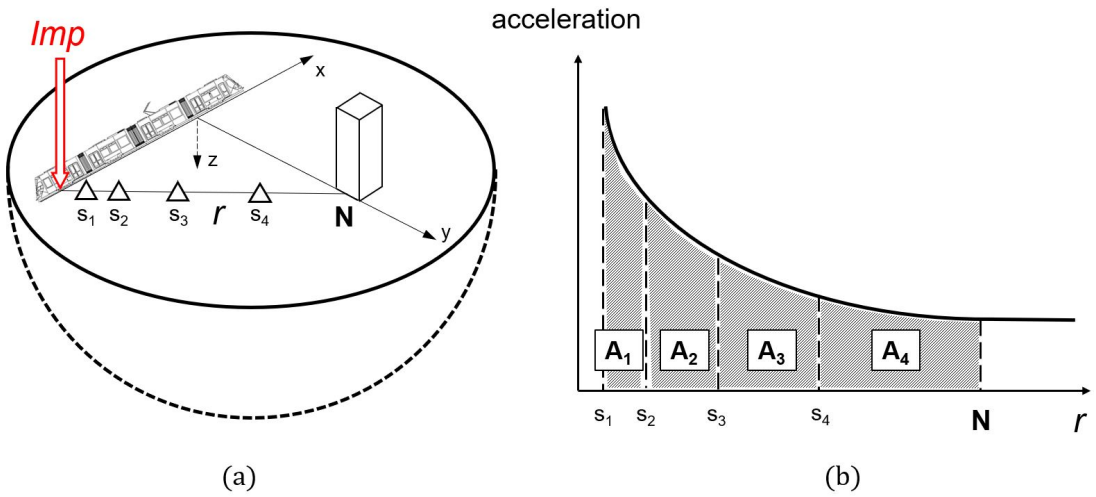

Figure 5.2: (a) Distribution of sensors, s_n, over the vibration path distance, r. (b) Evolution of acceleration with distance from the vibration source, s_n, from the data measured by the accelerometers.

In this case the sensors are placed so that they all cover the same areas under the curve. Therefore, in the area of greatest signal change more sensors are concentrated, while when the curve flattens the sensors are far apart. If the sensors had been placed equidistantly, many of them would have measured practically the same signal while in another section the density of sensors would have been insufficient to capture changes occurring over short distances.

Piezoelectric accelerometers are the first choice for most vibration measurements since they have a wide frequency response, good sensitivity and resolution, and are easy to install [75]. Because accelerometers are so versatile, a large variety of designs, sizes, and ranges exist to choose from. The choice of different electrical and physical specifications for accelerometers mainly depends on the expected signal characteristics to measure and any environmental constraints.

An accelerometer sensitivity describes the conversion between vibration and voltage at a reference frequency. For a typical accelerometer sensitivity of 100 mV/g, the output for a 10 g measured signal is 1000 mV. Note that g represents g-force, which is a unit of measurement of acceleration. Generally, a low-sensitivity accelerometer is used to measure high amplitude signals, while a high sensitivity accelerometer is employed to measure low amplitude signals.

Regarding mounting, stud mounting is the best technique, but it requires drilling into the target material and is generally reserved for permanent sensor installation. Other methods, such as magnetic or adhesive mounting, are meant for temporary attachment. The various

attachment methods all affect the measurable frequency of the accelerometer. Generally, the looser the connection, the lower the measurable frequency limit.

The most common accelerometer measures acceleration along only a single axis. This type is often used to measure mechanical vibration levels. Since the methodology presented in this work and the case study developed mainly focus on vertical accelerations, this type of sensor seems the most suitable.

NI offers two types of uniaxial accelerometers, the PCB 352C03 and the PCB 352C33, with frequency ranges from 0.5 to 10000 Hz and can be mounted with a stud or adhesive mount [76]. The PCB 352C03 model has a measurement range of $\pm$500 g and a sensitivity of 10 mV/g. In contrast, the sensitivity of the PCB 352C33 PCB model is much higher (100 mV/g) but at the cost of a smaller measuring range of $\pm$50 g. The measuring range represents the level of acceleration supported by the sensor's output signal specifications.

A good option would be to find an accelerometer with a good balance between measuring range and sensitivity. That is, a sensor with intermediate characteristics between the PCB 352C03 and the PCB 352C33 could be adapted to the features of the case study of the Ring 3 line.

Another option to consider is that of variable capacitance (VC) accelerometers. This type of sensor measures low-frequency dynamic events, prioritizing high sensitivity versus wideband frequency response [77]. Given the appearance of low frequencies in some of the case study results, VC accelerometers would help to capture the low-frequency response that may resonate with building or track elements.

Finally, a proposed field instrumentation plan that applies all the considerations developed in this subsection is shown. The plan shows the distribution of accelerometers on the track, the ground, and the study building. The sensors in the building are placed in the center of the slab, and stud mounting can be used or, alternatively, adhesive mount if drilling is not possible.

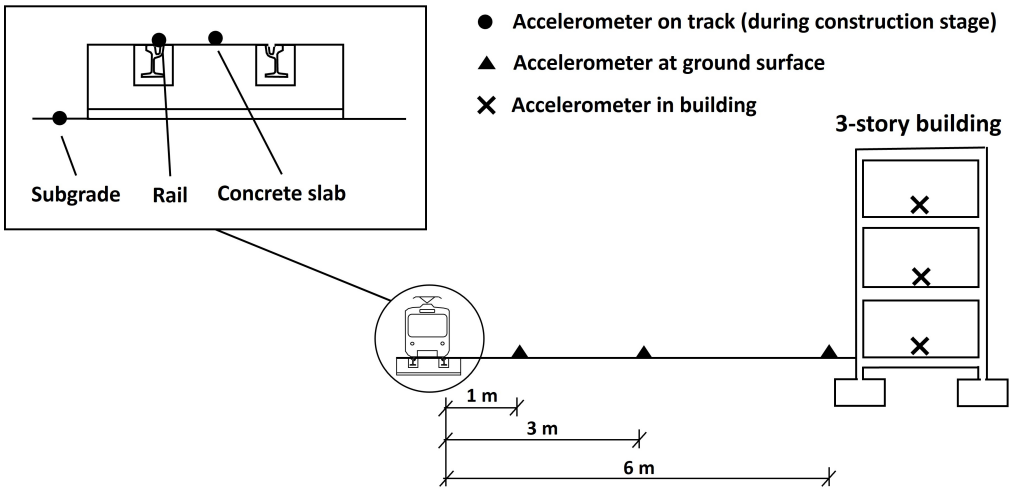

Figure 5.3: Field instrumentation plan showing accelerometers setups on track, ground and building.

Bibliography

[1] United Nations Development Programme.
Sustainable development goals.
`https://www.undp.org/sustainable-development-goals`.
Accessed: 2022-03-07.

[2] J. Schofer.
The benefits of urban mass transit.
`https://www.britannica.com/topic/mass-transit/Mass-transit-finance`, .
Accessed: 2022-02-24.

[3] G. Kouroussis, L. Van Parys, C. Conti, and O. Verlinden.
Prediction of ground vibrations induced by urban railway traffic: An analysis of the coupling assumptions between vehicle, track, soil, and buildings.
International Journal of Acoustic and Vibration, 18(4):163–172, 2013.

[4] A. Smart.
Sydney transport: trams halted, buses hacked.
City Hub Sydney, 2020.

[5] M. Montesinos.
No más ruido pide medidas por las vibraciones del tranvía.
La Verdad, 2015.

[6] A. Maluenda.
Nuevas denuncias por el ruido y las vibraciones del tranvía.
Heraldo, 2012.

[7] R. Fausset.
Durham dreamed of a transit line. duke university all but killed it.
The New York Times, 2019.

[8] J. Schofer.
Bæredygtige transportformer.

https://transforming.dtu.dk/mobilitet, .
Accessed: 2022-03-09.

[9] M. Anderson.
Vibration.
https://www.britannica.com/science/vibration.
Accessed: 2022-03-13.

[10] H. Lamb.
On the propagation of tremors over the surface of an elastic solid.
Philosophical Transactions of the Royal Society A, 203:1–42, 1904.

[11] L. Rayleigh.
On waves propagated along the plane surface of an elastic solid.
Proceedings of The London Mathematical Society, 17:4–11, 1885.

[12] F.E. Richart, Jr. J. L. Hall, and R. D. Woods.
Vibrations of Soils and Foundations.
Prentice Hall, Inc, 1970.

[13] D.P. Connolly, G. Kouroussis, O. Laghrouche, C.L. Ho, and M.C. Forde.
Benchmarking railway vibrations: Track, vehicle, ground and building effects.
Construction and Building Materials, (92):64–81, 2015.

[14] B. Hyun Nam, J. Kim, J. An, and B. Kim.
A review on the effects of earthborne vibrations and the mitigation measures.
International Journal of Railway, 6(3):95–106, 2013.

[15] L. Hall.
Simulations and analyses of train-induced ground vibrations in finite element models.
Soil Dynamics and Earthquake Engineering, 23(5):403–413, 2003.

[16] D. Kim and J. Lee.
Propagation and attenuation characteristics of various ground vibrations.
Soil Dynamics and Earthquake Engineering, 19:115–126, 2000.

[17] G. Paneiro, F.O. Durão, M. Costa e Silva, and P. Falcão.
Prediction of ground vibration amplitudes due to urban railway traffic using quantitative and qualitative field data.
Transportation Research Part D, 40:1–13, 2015.

[18] M. Bédard.
The effects of vibrations on buildings.

https://cep-experts.ca/the-effects-of-vibrations-on-buildings/.
Accessed: 2022-03-17.

[19] MasterHD at English Wikipedia. Public domain.
Resonance.
https://commons.wikimedia.org/wiki/File:Resonance.PNG.
Accessed: 2022-02-24.

[20] L. Ling, J. Han, X. Xiao, and X. Jin.
Dynamic behavior of an embedded rail track coupled with a tram vehicle.
Journal of Vibration and Control, 23(14):2355–2372, 2017.

[21] A. Yavari.
Quasi-static loading.
https://imechanica.org/node/8437.
Accessed: 2022-03-18.

[22] R.Verachtert, H.E.M.Hunt, M.F.M.Hussein, and G.Degrande.
Changes of perceived unevenness caused by in-track vibration countermeasures in slab track.
European Journal of Mechanics - A/Solids, 65:40–58, 2017.

[23] E. Ntotsios, D. Thompson, and M. F. M. Hussein.
The effect of track unevenness correlation on railway induced ground vibration.
6th ECCOMAS Thematic Conference on Computational Methods in Structural Dynamics and Earthquake Engineering, 2017.

[24] H. Peng, Y. Yao, X. Cai, Y. Zhong, and T. Sun.
Field measurement analysis and control measures evaluation of metro vehicle noise caused by rail corrugation.
Applied Sciences, 11(23), 2021.

[25] W. Jeong.
Spectral characteristics of rail surface by measuring the growth of rail corrugation.
Applied Sciences, 11(20), 2021.

[26] G. Kouroussis, S. Zhu, and K. Vogiatzis.
Noise and vibration from transportation.
Journal of Zhejiang University-SCIENCE A, 22(1):1–5, 2021.

[27] G. Kouroussis, G. Alexandrou, and O. Verlinden.
A comprehensive prediction model for vehicle/track/soil dynamic response due to wheel flats.

Proceedings of the Institution of Mechanical Engineers, Part F: Journal of Rail and Rapid Transit, 230(4):1088–1104, 2015.

[28] C. Hanson, D. Towers, and L. Meister.
Transit noise and vibration impact assessment.
U.S. Department of Transportation, Federal Transit Administration, Office of Planning and Environment, 2006.

[29] T. Maeda, P. Gautier, B. Hemsworth C.E. Hanson, J.T. Nelson, B. Schulte-Werning, D. Thompson, and P. de Vos.
Noise and vibration mitigation for rail transportation systems.
Notes on Numerical Fluid Mechanics and Multidisciplinary Design, 118:259–266, 2012.

[30] G. Kouroussis, O. Verlinden, and C. Conti.
On the interest of integrating vehicle dynamics for the ground propagation of vibrations: the case of urban railway traffic.
Noise and Vibration Mitigation for Rail Transportation Systems, 48(12):1553–1571, 2010.

[31] P.J. Mistry, M.S. Johnson, S. Li, S. Bruni, and A. Bernasconi.
Parametric sizing study for the design of a lightweight composite railway axle.
Composite Structures, 1, 2021.

[32] Pandrol.
Pandrol qtrack®.
`https://www.pandrol.com/product/q-track/`.
Accessed: 2022-04-12.

[33] M. Ahac and S. Lakušic.
Rail traffic noise and vibration mitigation measures in urban areas.
Tehnicki Vjesnik, 19(2):427–435, 2012.

[34] Isolgomma.
Railway anti-vibration mats.
`https://www.isolgomma.com/railway-antivibration-solution/railway-anti-vibration-mats/`.
Accessed: 2022-04-12.

[35] G. Lombaert, G. Degrande, S. François, and D.J. Thompson.
Ground-borne vibration due to railway traffic: A review of excitation mechanisms, prediction methods and mitigation measures.
Notes on Numerical Fluid Mechanics and Multidisciplinary Design, 126:253–287, 2013.

[36] D. Adam, A. Vogel, and A. Zimmermann.
Ground improvement techniques beneath existing rail tracks.
Ground Improvement, 11(4):229–235, 2007.

[37] F. Richart, J. Hall, and R. Woods.
Vibrations of soils and foundations.
Prentice-Hall, Englewood Cliffs, 1970.

[38] John A. Volpe National Transportation Systems Center.
Transit Noise and Vibration Impact Assessment Manual.
Federal Transit Administration, 2018.

[39] P. Coulier, S. François, G. Degrande, and G. Lombaert.
Subgrade stiffening next to the track as a wave impeding barrier for railway induced vibrations.
Soil Dynamics and Earthquake Engineering, 48:119–131, 2013.

[40] D. Thompson.
Railway noise and vibration: mechanisms, modelling, and means of control.
Elsevier, Oxford, 2009.

[41] H. Verbraken, G. Degrande, and G. Lombaert.
Experimental and numerical determination of transfer functions along railway tracks.
Proceedings of the 9th National Congress on Theoretical and Applied Mechanics, pages 1–9, 2012.

[42] G. Kouroussis, D. P. Connolly, and O. Verlinden.
Railway-induced ground vibrations – a review of vehicle effects.
International Journal of Rail Transportation, 2(2):69–110, 2014.

[43] E. Winkler.
Die Lehre von der Elastizität und Festigkeit.
H. Domenicus. Prague, 1867.

[44] M. Mohanta, G. Setu, P.K. Sarkar J.P. Srivastava, and V. Ranjan.
Static analysis of railway track.
Proceedings of India International Science Festival. Young Scientists' Meet, 2015.

[45] A. J. C. B. Saint-Venant.
Memoire sur la torsion des prismes.
Mem. Divers Savants, 14:233–560, 1855.

[46] J. Boussinesq.

Applications des potentiels à l'étude de l'équilibre et mouvement des solides elastiques. Gauthier–Villard. Paris, 1885.

[47] K. Symon.
Mechanics.
Addison Wesley, Boston, 1971.

[48] S. E. A. Raheem, M. M. Ahmed, and T. M. A. Alazrak.
Soil-raft foundation-structure interaction effects on seismic performance of multi-story mrf buildings.
Engineering Structures and Technologies, 6(2):43–61, 2014.

[49] S.S. Rao and F.F. Yap.
Mechanical Vibrations.
Addison Wesley, Boston, 1995.

[50] M. Varanis, A. L. Silva, and A. G. Mereles.
On mechanical vibration analysis of a multi degree of freedom system based on arduino and mems accelerometers.
Revista Brasileira de Ensino de Física, 40(1), 2018.

[51] R. N. D. Anjuman.
Vibration eigen value and eigen vector problem in free vibration 1 d-bar element.
`https://slidetodoc.com/vibration-eigen-value-and-eigen-vector-problem-in/`.
Accessed: 2022-06-04.

[52] M. Belgasmia.
Structural Dynamics and Static Nonlinear Analysis From Theory to Application.
IGI Global, 2021.

[53] LearnEMC.
Time/frequency domain representation of signals.
`https://slidetodoc.com/vibration-eigen-value-and-eigen-vector-problem-in/`.
Accessed: 2022-06-21.

[54] D. Nishiura, H. Sakai, A. Aikawa, S. Tsuzuki, and H. Sakaguchi.
Novel discrete element modeling coupled with finite element method for investigating ballasted railway track dynamics.
Computers and Geotechnics, 96:40–54, 2018.

[55] H. Yu and Y. Yuan.
Analytical solution for an infinite euler-beam on a viscoelastic foundation subjected to arbitrary dynamic loads.

Journal of Engineering Mechanics, 140(3), 2014.

[56] I. L. Vér, C. S. Ventres, and M. M. Myles.
Wheel/rail noise - part iii: Impact noise generation by wheel and rail discontinuities.
Journal of Sound and Vibration, 46(3):395–417, 1976.

[57] E. Woodward.
Geometry - Plane, Solid Analytic Problem Solver.
Research Education, 1978.

[58] Farnell.
Damping coefficient.
`https://uk.farnell.com/damping-coefficient-definition`.
Accessed: 2022-07-03.

[59] J. M. Mussat, R. D. Bertero, and P. M. Barbieri.
Propagation and attenuation of statistically stationary ground vibrations due to human activities.
Journal of Geotechnical and Geoenvironmental Engineering, 145(9), 2019.

[60] M. E. M. Hunt.
Stochastic modelling of traffic-induced ground vibration.
Journal of Sound and Vibration, 144(1):53–70, 1991.

[61] M. Rahman and T. Michelitsch.
A note on the formula for the rayleigh wave speed.
Wave Motion, 43(3):272–276, 2006.

[62] Siemens.
Avenio – fits your city.
`https://www.mobility.siemens.com/global/en/portfolio/rail/rolling-stock/trams-and-light-rail/avenio.html`.
Accessed: 2022-04-18.

[63] Hovedstadens Letbane.
Fakta om hovedstadens letbane.
`https://www.dinletbane.dk/da/se-visionerne/fakta/`.
Accessed: 2022-04-21.

[64] De Nationale Geologiske Undersøgelser for Danmark og Grønland.
The geus jupiter database.
`https://data.geus.dk/geusmap`.
Accessed: 2022-04-18.

[65] Geotechdata.info.
Soil young's modulus.
http://www.geotechdata.info/parameter/soil-young-s-modulus.
Accessed: 2022-04-18.

[66] edilon)(sedra.
System information sheet - corkelast ers (embedded rail system) type ers lr 60r2-ms.
2020.

[67] H. Lin, T. Bengisu, and Z. Mourelatos.
Modeling the stiffness and damping properties ofstyrene-butadiene rubber.
SAE International, 2011.

[68] H. Lin, T. Bengisu, and Z. Mourelatos.
Dynamic properties of styrene-butadiene rubber for automotive applications.
SAE Technical Papers, 2009.

[69] S. E. A. Raheem, M. M. Ahmed, and T. M. A. Alazrak.
Landing and perching on vertical surfaces with microspines for small unmanned air vehicles.
Engineering Structures and Technologies, 57(1-4):313–327, 2010.

[70] H. Cho and J. Park.
Study of rail squat characteristics through analysis of train axle box acceleration frequency.
Applied Sciences, 11(15), 2021.

[71] J. Vanwalleghem, I. De Baere, M. Loccufier, and W. Van Paepegem.
Practical aspects in measuring vibration damping of materials.
Inegi-Inst Engenharia Mecanica E Gestao Industrial, 2012.

[72] M. Maglio, A. Pieringer, J. C. O.Nielsen, and T. Vernersson.
Wheel–rail impact loads and axle bending stress simulated for generic distributions and shapes of discrete wheel tread damage.
Journal of Sound and Vibration, 502, 2021.

[73] C. Chang, Y. Cai, B. Chen, Q. Li, and P. Lin.
Experimental study of the wheel/rail impact caused by wheel flat within 400 km/h using full-scale roller rig.
Railway Sciences, 1(1):76–89, 2022.

[74] B. An, L. Gao, T., G. Xiang, and J. Wang.
A novel approach of identifying railway track rail's modal frequency from wheel-rail excitation and its application in high-speed railway monitoring.
IEEE Access, 7(1), 2020.

[75] B. Lent.
Simple steps to selecting the right accelerometer.
https://www.fierceelectronics.com/sensors/chips-act-gets-praise-and-ding.
Accessed: 2022-07-24.

[76] NI.
Measuring vibration with accelerometers.
https://www.ni.com/da-dk/innovations/white-papers/06/measuring-vibration-with-accelerometers.html.
Accessed: 2022-07-24.

[77] Inc. Dytran Instruments.
Variable capacitance mems accelerometers.
https://www.dytran.com/DC-MEMS/.
Accessed: 2022-07-24.

{2.7182818284}ϑφερτυθιοπσδφγηξκλ